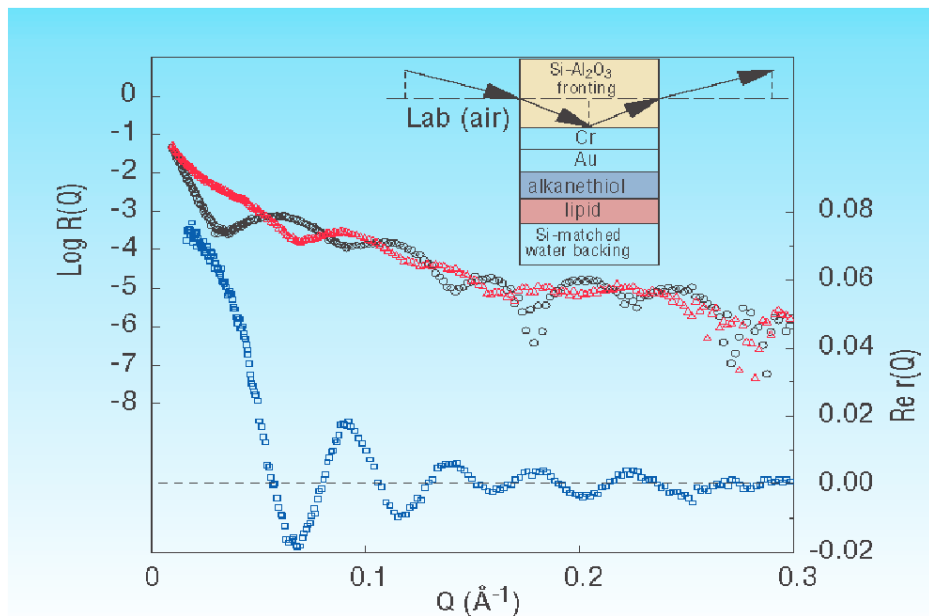


# What can the reflection of neutrons reveal about the structure of hard and soft condensed matter?



C.F. Majkrzak  
Center for Neutron Research  
National Institute of Standards and Technology

NCNR Neutron Scattering School, February 2021



**FIGURE 2.** Reflectivity curves for the thin film system depicted schematically in the inset, one for a Si fronting (red triangles), the other for  $\text{Al}_2\text{O}_3$  (black circles). The curve in the lower part of the figure (blue squares) is the real part of the complex reflection amplitude for the films obtained from the reflectivity curves by the method described in the text.

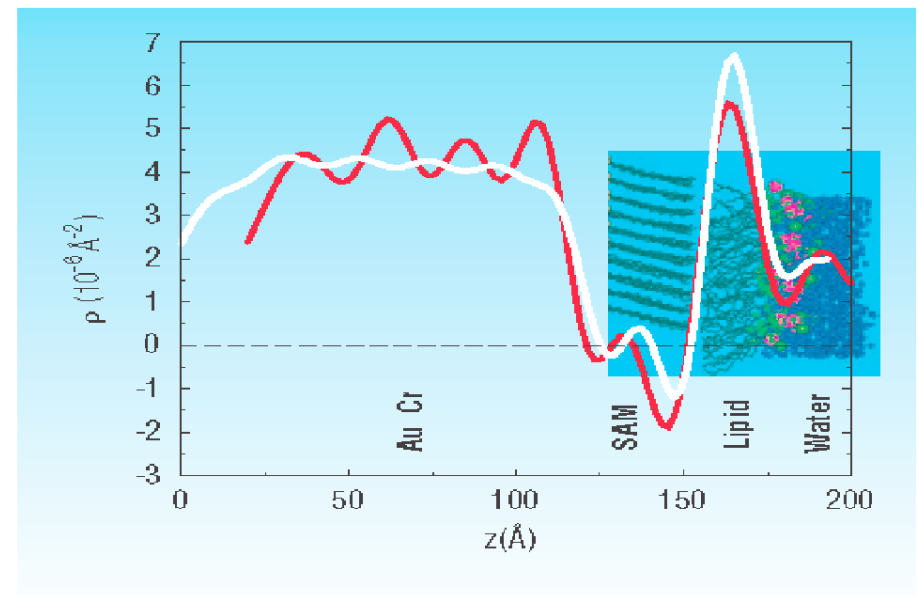
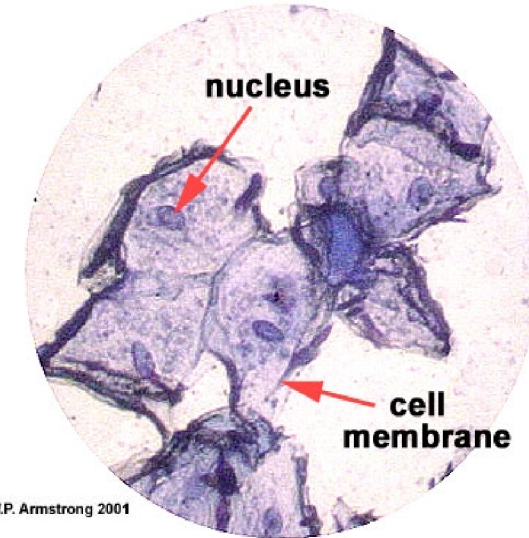
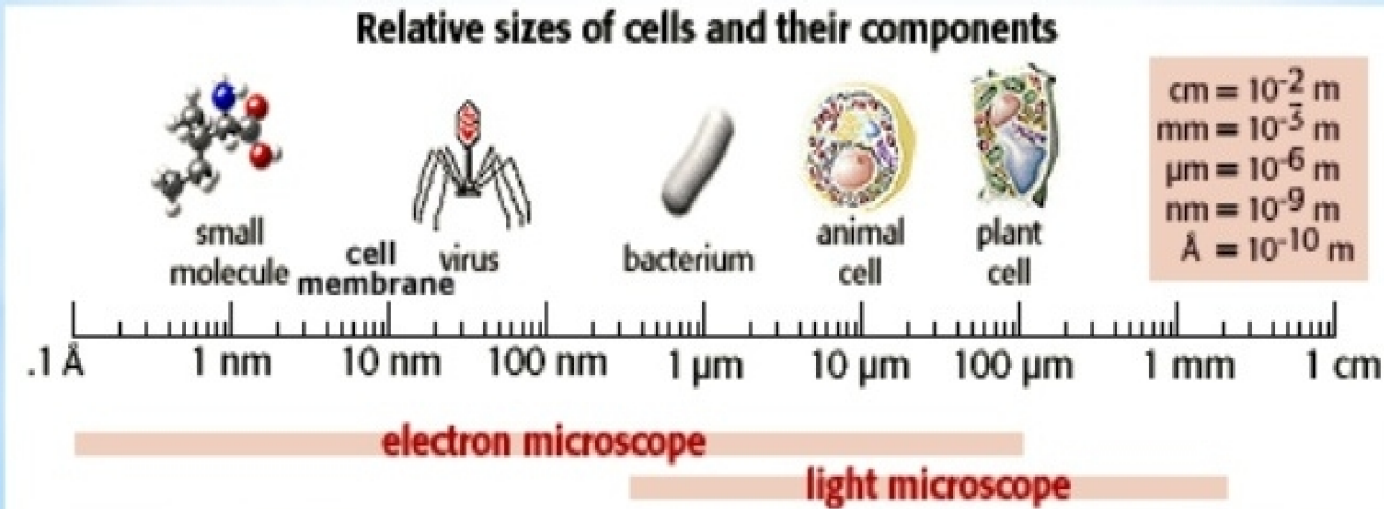


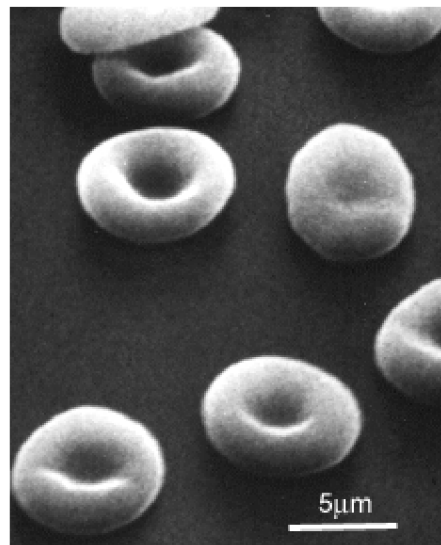
**FIGURE 3.** SLD profile (red line) resulting from a direct inversion of the  $\text{Re } r$  of Fig. 2 compared with that predicted by a molecular dynamics simulation (white line) as discussed in the text. The headgroup for the Self-Assembled-Monolayer (SAM) at the Au surface in the actual experiment was ethylene oxide and was not included in the simulation but, rather, modelled separately as part of the Au. Also, the Cr-Au layer used in the model happened to be 20 Å thicker than that actually measured in the experiment.



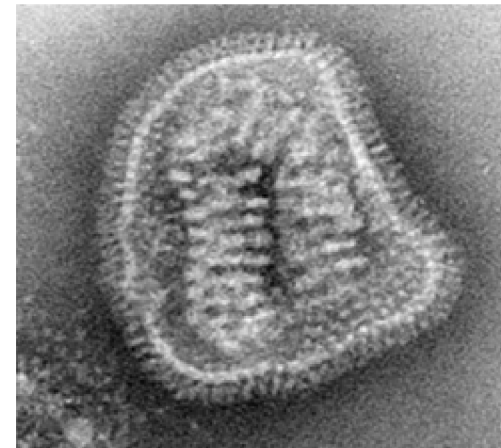
# A common theme – trying to see structure in objects at very small length scales --



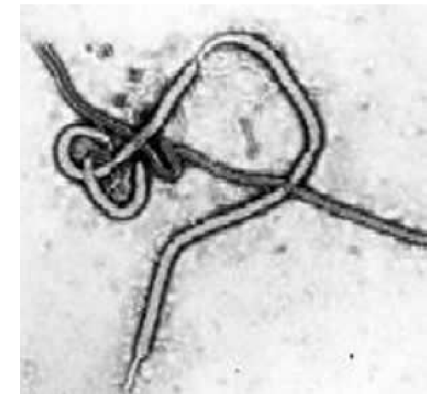
(Wikipedia EM)



(red blood cells Leeds)

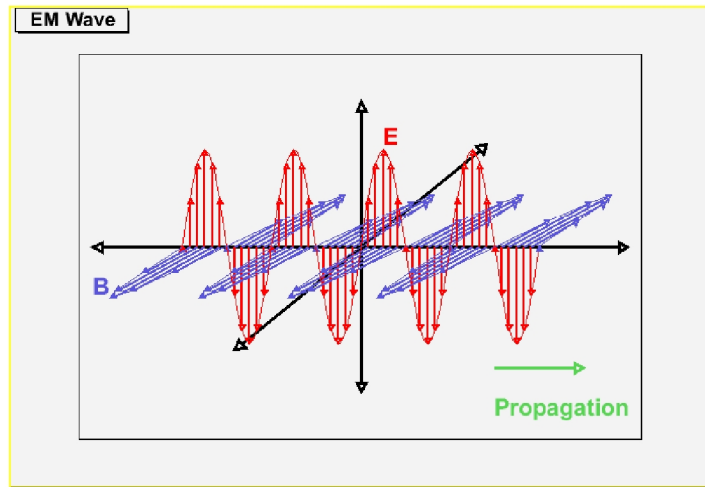


(virus ASU)

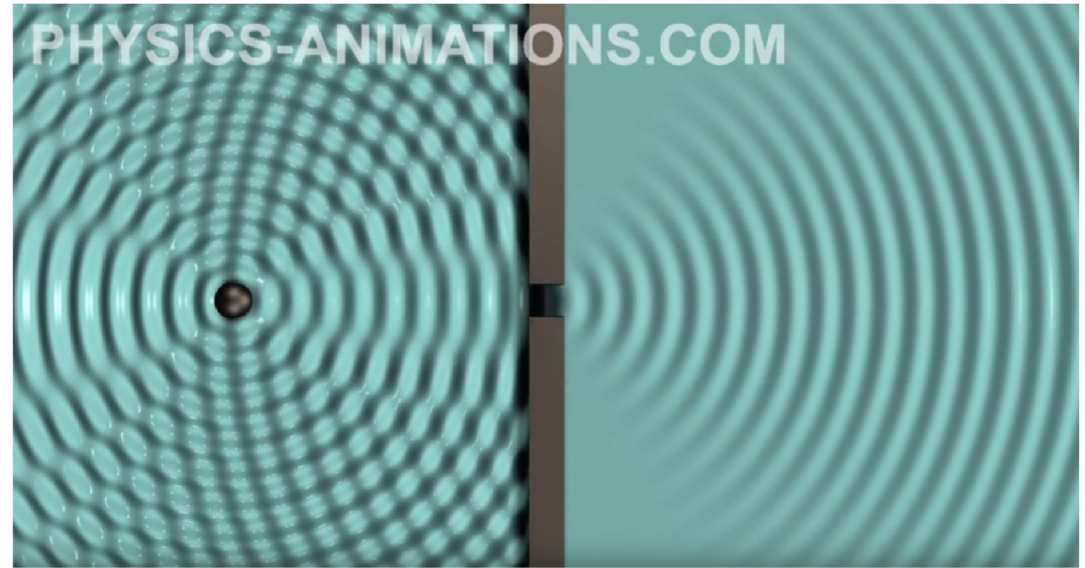


(Ebola UTMB)

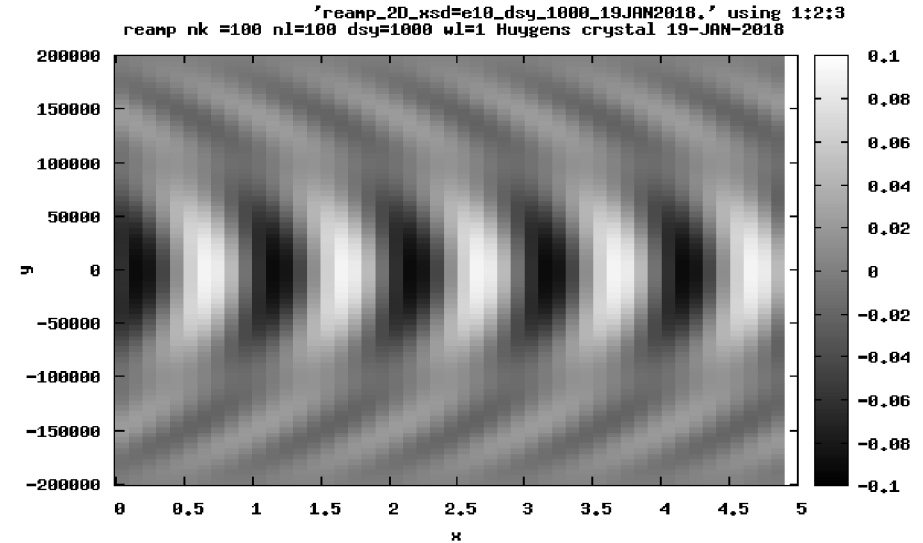
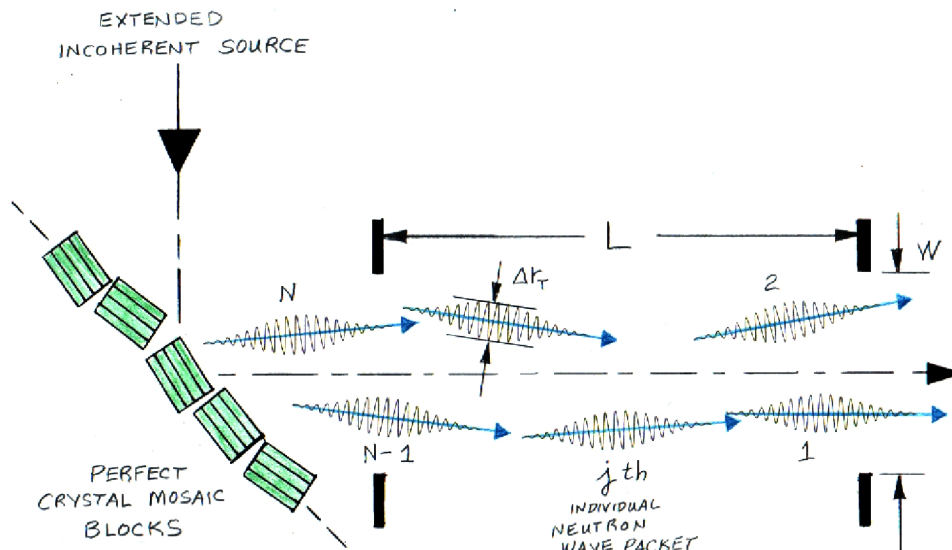
# From real space images and geometrical optics to wave behavior and diffraction patterns:



(physics.indiana.edu)



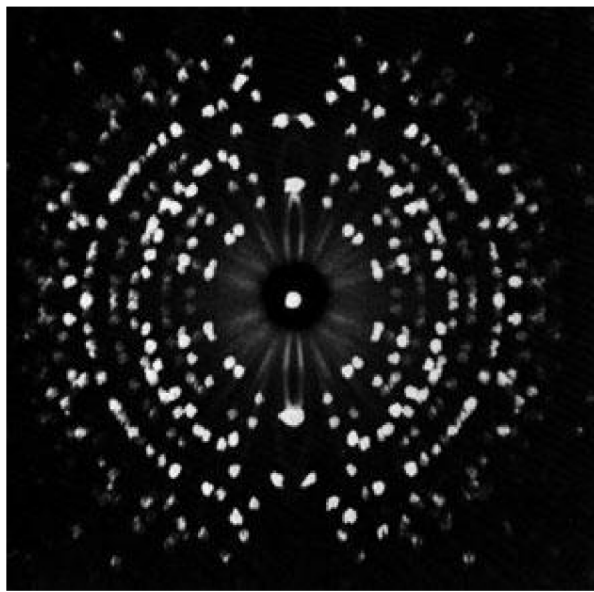
$$r(k) = [4\pi/(i2k_z S)] \int \Psi(k) \rho(r) e^{ik \cdot r} d^3r$$



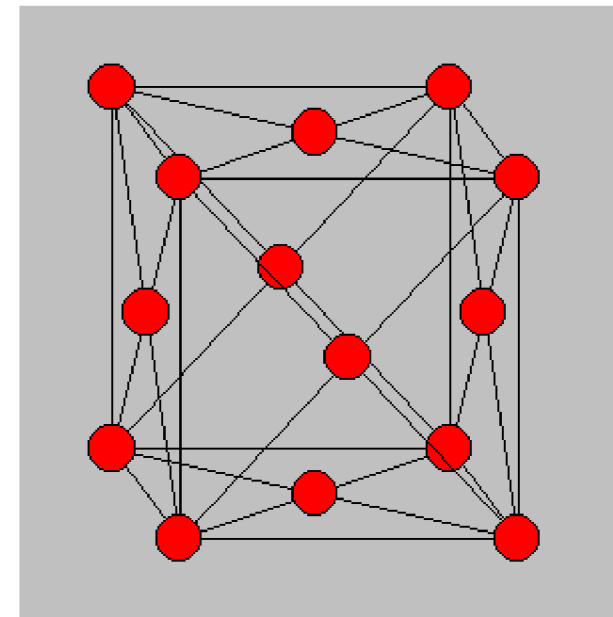
the neutron wave packet – a particle probe with a built-in ruler



## Diffraction examples --



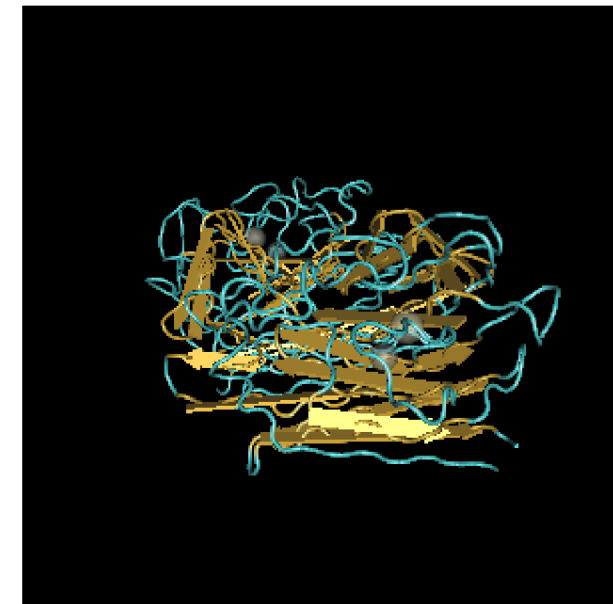
(H.J. Milledge)



(colorado.edu)



(Pea.Lectin.einstein.cclrc.ac.uk)



(prasthofer pea lectin)

# Neutron Reflectometry and Diffraction from Layered Media

Advances in the preparation of thin films helped create a specialized configuration for elastic neutron diffraction at low momentum transfers from layered matter at glancing angles of incidence – neutron reflectometry. Early work in this area was pioneered by a number of people at different institutions, including Gian Felcher (ANL), Bob Thomas, Jeff Penfold, Adrian Rennie (Oxford), John Hayter, Giovanna Fragneto (ILL), John White, Bernard Farnoux (Saclay), Jarek Majewski (LANL), Greg Smith, Bill Hamilton and others. For a review of the early history, see, for example, *The application of the specular reflection of neutrons to the study of surfaces and interfaces*, J Penfold and R K Thomas 1990 J. Phys.: Condens. Matter 2 1369, *The Origins of Neutron Reflectometry*, C.F. Majkrzak and J. Penfold, Neutron News Volume 21, Issue 1, 2010, and *Neutron Scattering Studies of Surfaces and Interfaces*, C.F. Majkrzak and G.P. Felcher, MRS Bulletin Volume: 15 Issue: 11 Pages: 65-72 NOV 1990.

## <> Fundamentals of the Theory

## <> Basic Experimental Methods

## <> Practical Applications

- Soft Condensed Matter
- Hard Condensed Matter

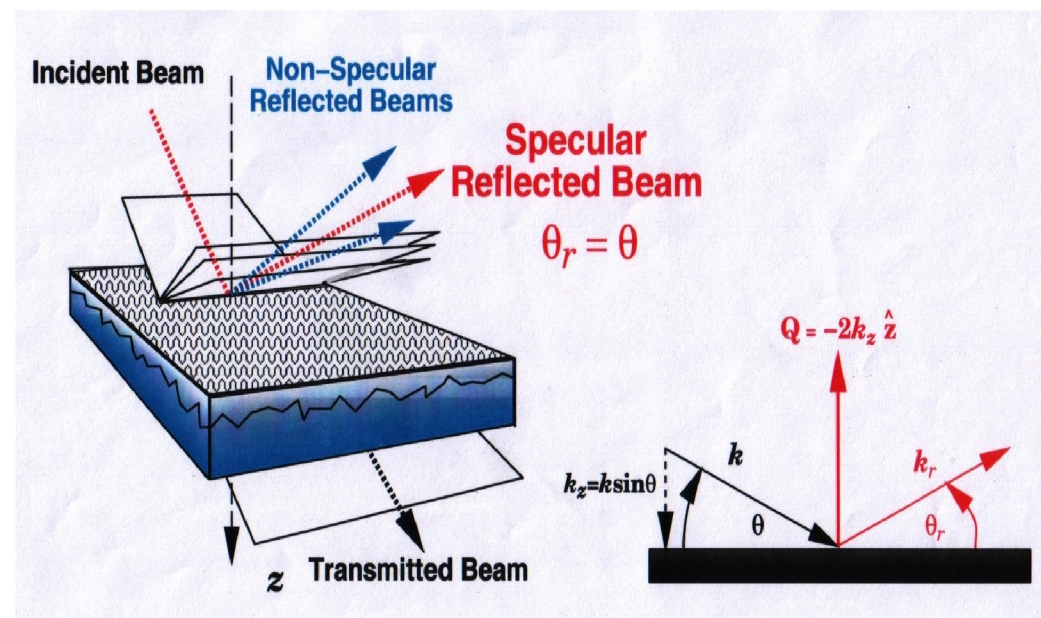
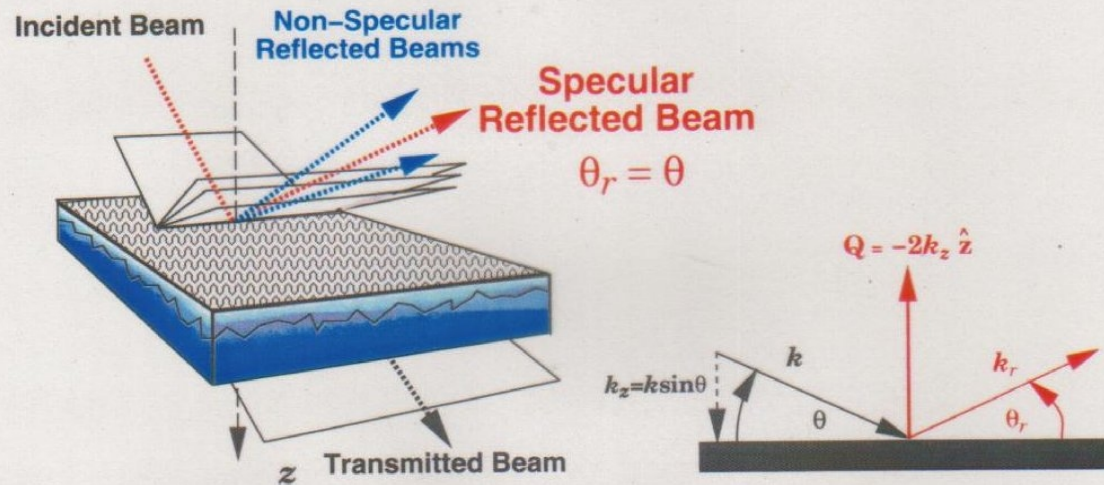


(figure thanks to Norm Berk)



$$\text{Reflectivity} = \frac{\text{Number of reflected neutrons}}{\text{Number of incident neutrons}} = |r|^2$$



**Specular reflection:**  $\bar{\rho}(z) = \langle \rho(x, y, z) \rangle_{xy}$

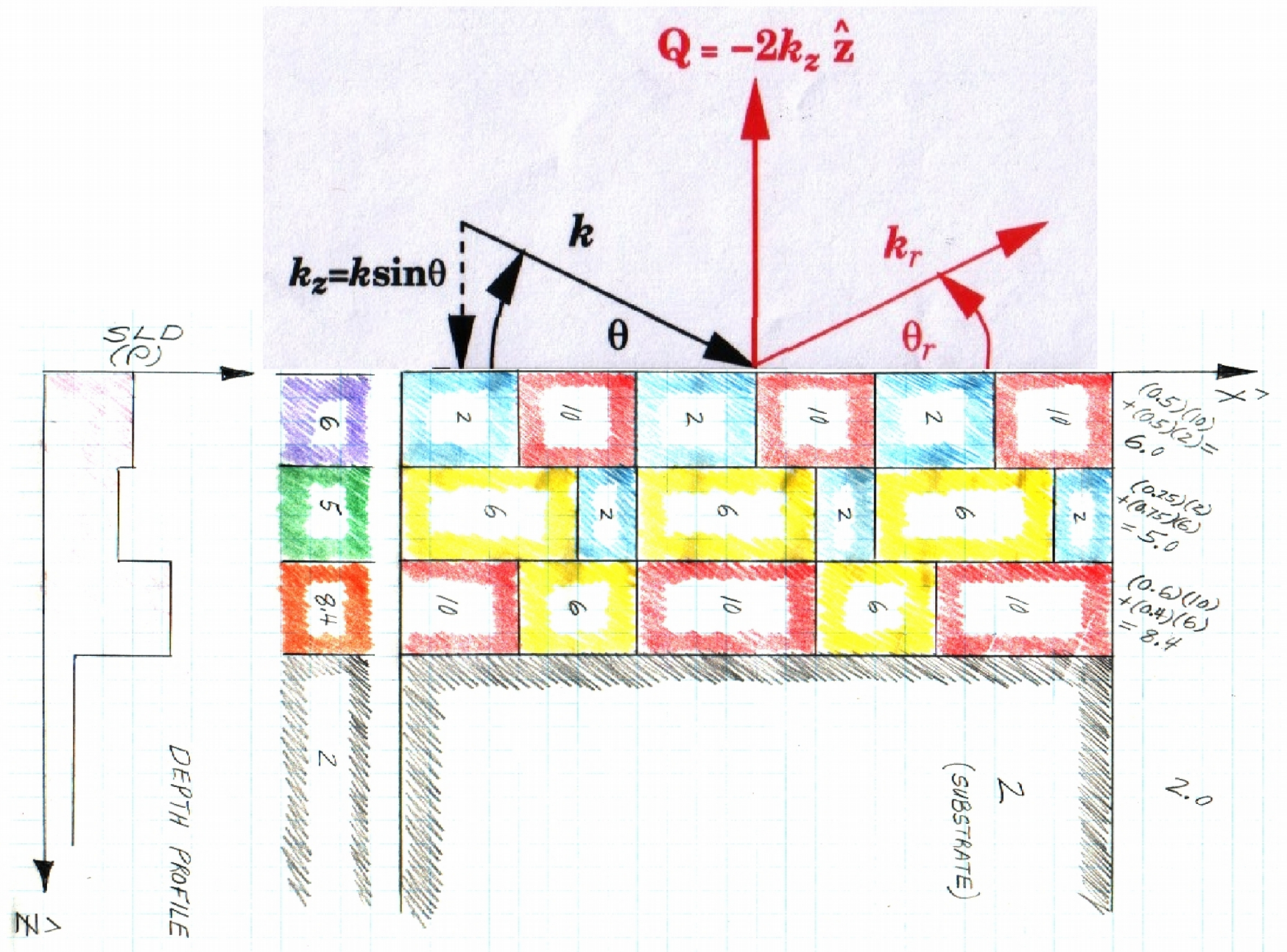
**Non-Specular reflection:**  $\Delta \rho(x, y, z) = \rho(x, y, z) - \bar{\rho}(z)$

(AFTER N.F. BERK ET AL.)

# Principal Uses and Advantages of Neutron Reflectometry (NR):

- \* For the specular condition, provides the chemical (isotopic) scattering length density (SLD) depth profile along the surface normal with a spatial resolution approaching half a nanometer.
- \* With polarized neutrons, provides the *vector* magnetization depth profile of a ferromagnetic material.
- \* Isotopic contrast, particularly applicable to hydrogen and deuterium.
- \* A non-destructive probe which can penetrate macroscopic distances through single crystalline substrates, making possible reflection studies of films in contact with liquids within a closed cell.
- \* As a consequence of the relatively weak interaction between the neutron and material, a remarkably accurate theoretical description of the reflection process and quantitative analysis of the data is possible, although the Born approximation is often not valid and an “exact” or “dynamical” formulation is required.
- \* NR is an established probe of the nanometer scale structure of both hard and soft condensed matter lamellar systems of interest in physics, chemistry, biology, and polymer and materials science

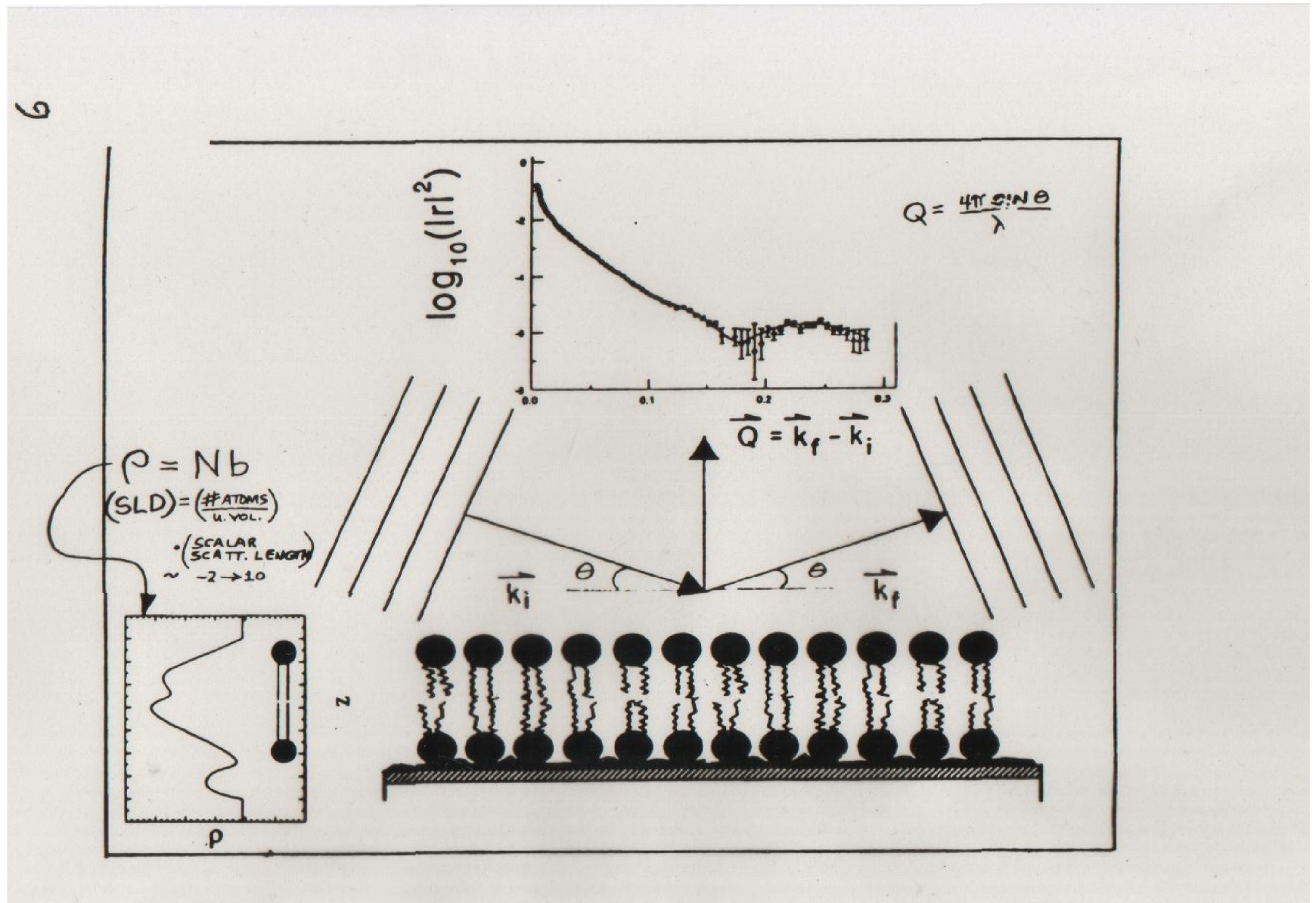




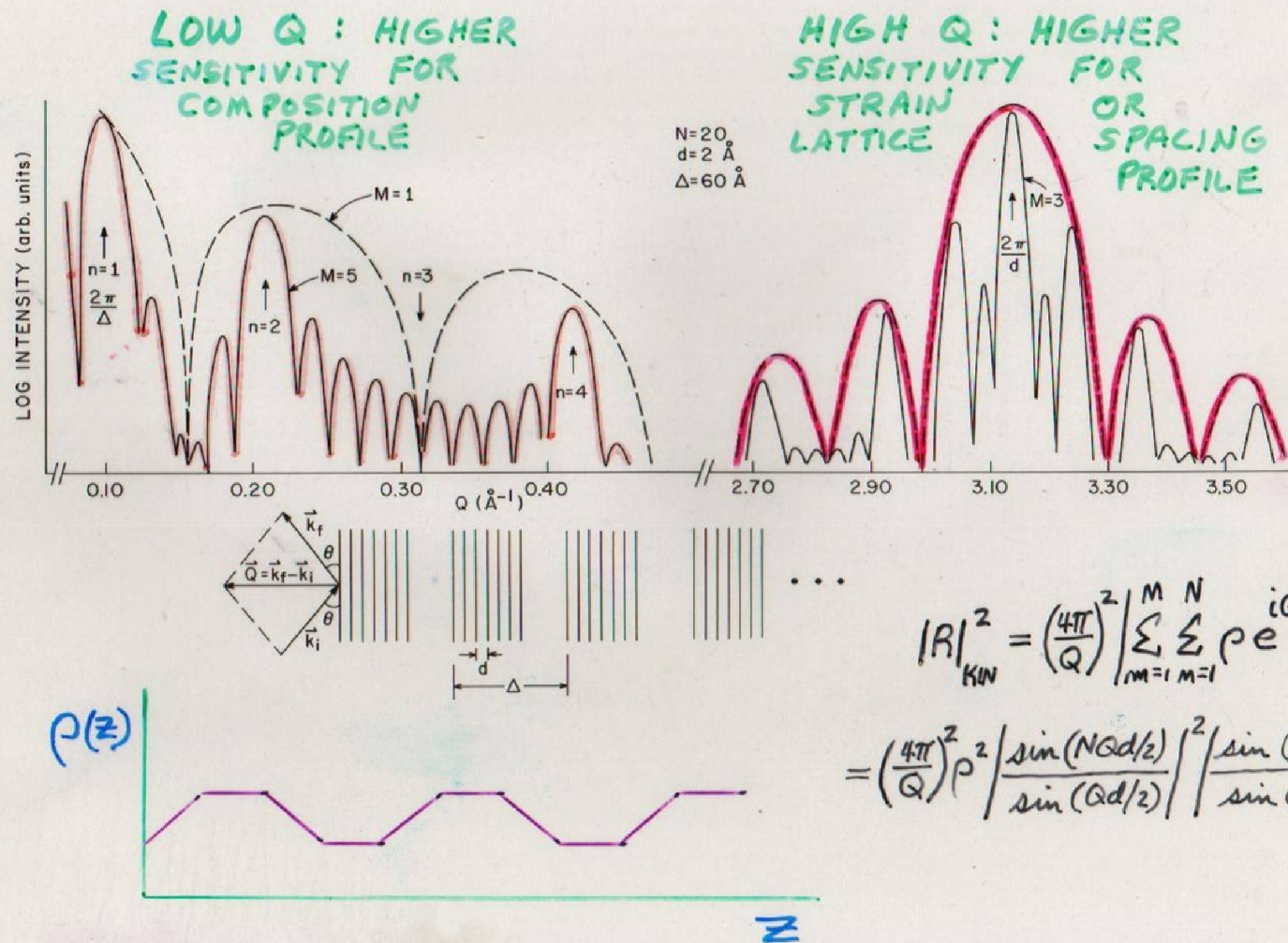
Averaging of the scattering length density (SLD) in the plane of a layer perpendicular to the wavevector transfer ( $Q$ ) occurs for the specular reflection condition  $\theta = \theta_r$ .



## What a neutron reflectometer (in the specular mode) probes



The specular reflection paradigm -- deducing the (in-plane average) scattering length density (SLD) depth profile along the surface normal from reflected intensity measured as a function of  $Q$ .



Specular reflectivity measurements are conventionally taken to mean elastic diffraction over a region of sufficiently low values of  $Q$  that sensitivity to structure at inter-atomic length scales is insignificant. Continuing a specular scan to high enough  $Q$  eventually allows the interatomic structure of, say, a superlattice to be revealed.

IN THE CONTINUUM LIMIT

$$V(\vec{r}) = \frac{2\pi\hbar^2}{m} \sum_{j=1} N_j b_j = \frac{2\pi\hbar^2}{m} \rho$$

NUMBER OF ATOMS  
OF TYPE  $j$  PER UNIT  
VOLUME

SCATTERING LENGTH  
DENSITY (SLD)

COHERENT  
SCATTERING LENGTH  
OF ATOM  $j$  —

$$b = \underbrace{\text{Re}b}_{\text{SCATTERING}} + i \underbrace{\text{Im}b}_{\text{ABSORPTION}}$$

IN VACUUM

$$E_0 = \frac{\hbar^2 k_0^2}{2m} + 0$$

IN A MATERIAL MEDIUM

$$E = \frac{\hbar^2 k^2}{2m} + \frac{2\pi\hbar^2}{m} \rho$$

CONSERVATION OF ENERGY REQUIRES  $E_0 = E$   
SO THAT

$$k^2 = k_0^2 - 4\pi\rho$$

& THEREFORE

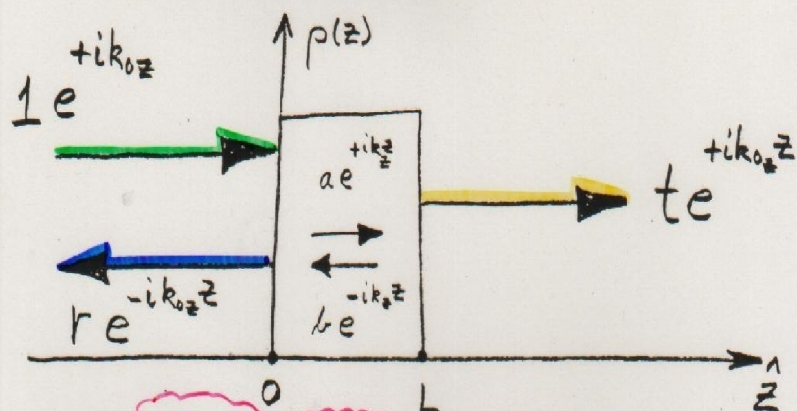
$$[\nabla^2 + k^2] \Psi = 0$$

CAN THEN DEFINE A REFRACTIVE INDEX  $n \equiv \frac{k}{k_0}$

OR

$$n^2 = 1 - \frac{4\pi\rho}{k_0^2}$$



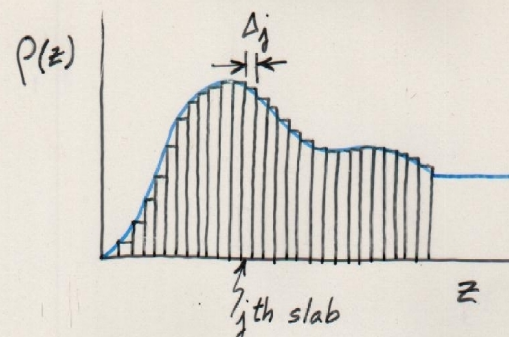


$$\frac{\partial^2 \psi(z)}{\partial z^2} + k_z^2 \psi(z) = 0$$

CONSERVATION OF MOMENTUM  
AND PARTICLE NUMBER  
REQUIRE THAT  $\frac{\partial \psi(z)}{\partial z}$  AND  $\psi(z)$

BE CONTINUOUS AT THE  
BOUNDARIES  $z=0$  &  $z=L$

$$\begin{pmatrix} t \\ it \end{pmatrix} e^{ik_0 L} = \begin{pmatrix} A & B \\ C & D \end{pmatrix} \begin{pmatrix} 1+r \\ i(1-r) \end{pmatrix}$$



$$\begin{pmatrix} A & B \\ C & D \end{pmatrix} = \begin{pmatrix} a_N & b_N \\ c_N & d_N \end{pmatrix} \begin{pmatrix} a_{N-1} & b_{N-1} \\ c_{N-1} & d_{N-1} \end{pmatrix} \dots \begin{pmatrix} a_2 & b_2 \\ c_2 & d_2 \end{pmatrix} \begin{pmatrix} a_1 & b_1 \\ c_1 & d_1 \end{pmatrix}$$

$$\begin{pmatrix} a_j & b_j \\ c_j & d_j \end{pmatrix} = \begin{pmatrix} \cos S_j & \frac{1}{m_{zj}} \sin S_j \\ -m_{zj} \sin S_j & \cos S_j \end{pmatrix}$$

$$S_j = k_{0z} m_{zj} \Delta_j \\ = k_{zj} \Delta_j$$

The elements A, B, C, and D of the so-called "transfer" matrix which relates the reflection, transmission, and incident wave amplitudes -- r, t, and 1, respectively -- contain all of the information about the SLD composition of the film. The transfer matrix can be constructed of a product of matrices, each of which corresponds to one successive "slice" of the film over which the SLD is taken to be a constant value. Thus, any arbitrary profile can be rendered -- and to whatever spatial resolution is needed by making the thicknesses of the slices small enough.

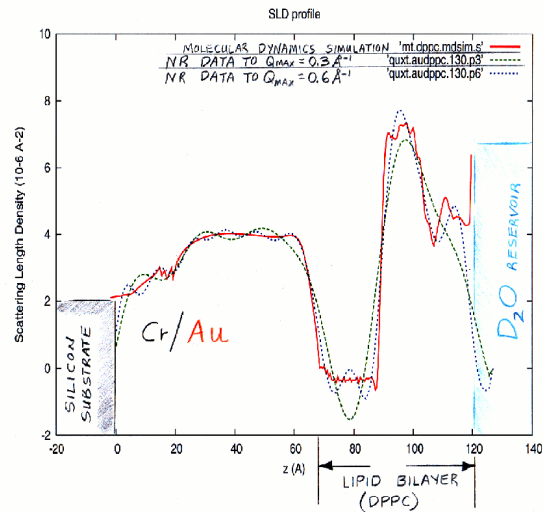
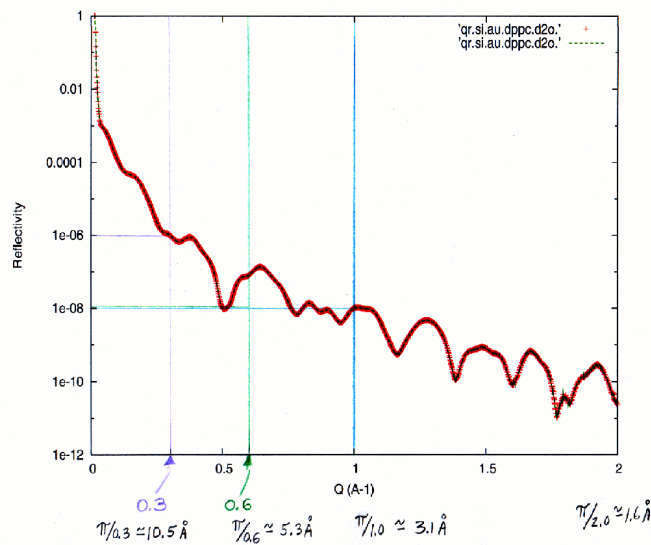
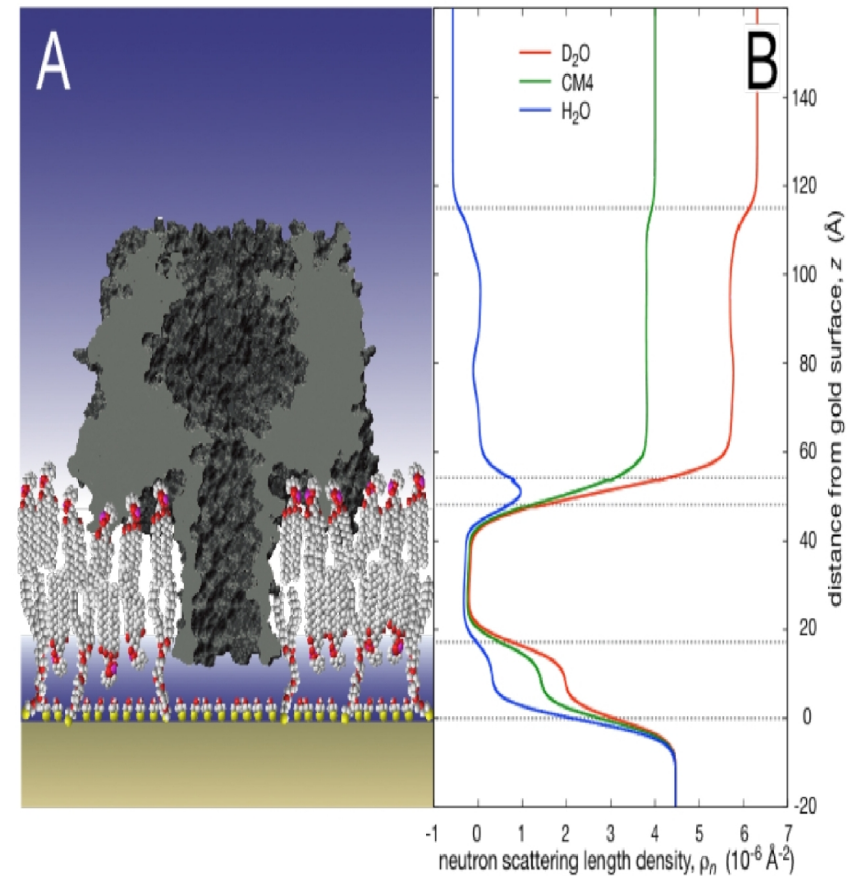


Illustration of the inverse relationship between the maximum value of  $Q$  up to which the reflectivity is measured and the spatial resolution in the corresponding SLD depth profile. Resolving smaller features in the profile in real space requires collecting reflectivity data up to larger values of  $Q$  in reciprocal space. The statistical accuracy in the measured reflectivity also affects the level of uncertainty in the associated SLD profile model to which the reflectivity data are fit.



Molecular sketch of alpha-hemolysin channel in a tethered bilayer lipid membrane as deduced from NR measurements (the left) with corresponding scattering length density profile (right) [10].

[10] D.J. McGillivray, G. Valincius, F. Heinrich, J.W.F. Robertson, D.J. Vanderah, W. Febo-Ayala, et al., Structure of functional *Staphylococcus aureus* alpha-hemolysin channels in tethered bilayer lipid membranes, *Biophys J.* **96** (2009) 1547–1553.



# Polarized Neutrons

<> a magnetic moment arises from the motion of electrical charges -- though neutral, a neutron is composed of charged quarks which give rise to a net magnetic dipole moment which is quantized with corresponding spin  $1/2$  -- a neutron is a Fermion

<> if it exists at all, any neutron electric dipole moment is of negligible magnitude for all practical purposes of concern to us here

<> a neutron can be represented by a spinor wave function having two components corresponding to two spin eigen-states (spin “+” or “up” and “-” or “down”)

<> for a nucleus with spin, the neutron-nucleus (i.e., the *nuclear*) interaction is spin-dependent

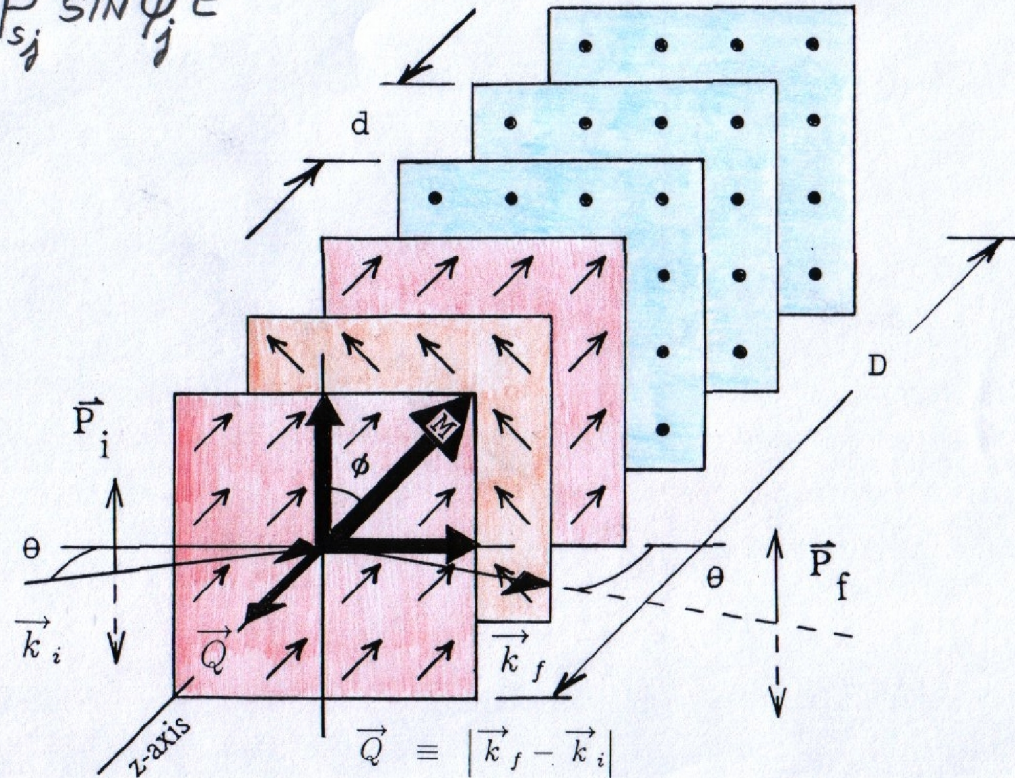
<> the *magnetic* interaction between the neutron magnetic moment and that of a *nuclear* magnetic moment is relatively weak (and nuclear magnetic moments are normally not ordered -- a notable exception occurring in a  $^3\text{He}$  gas cell used as a neutron polarizer)

<> the *magnetic* interaction between the neutron magnetic moment and that of an atomic magnetic moment, on the other hand, can be comparable to the nuclear interaction

(a good description of the phenomenon of a quantized spin one-half system is given in the quantum mechanics text by Merzbacher)

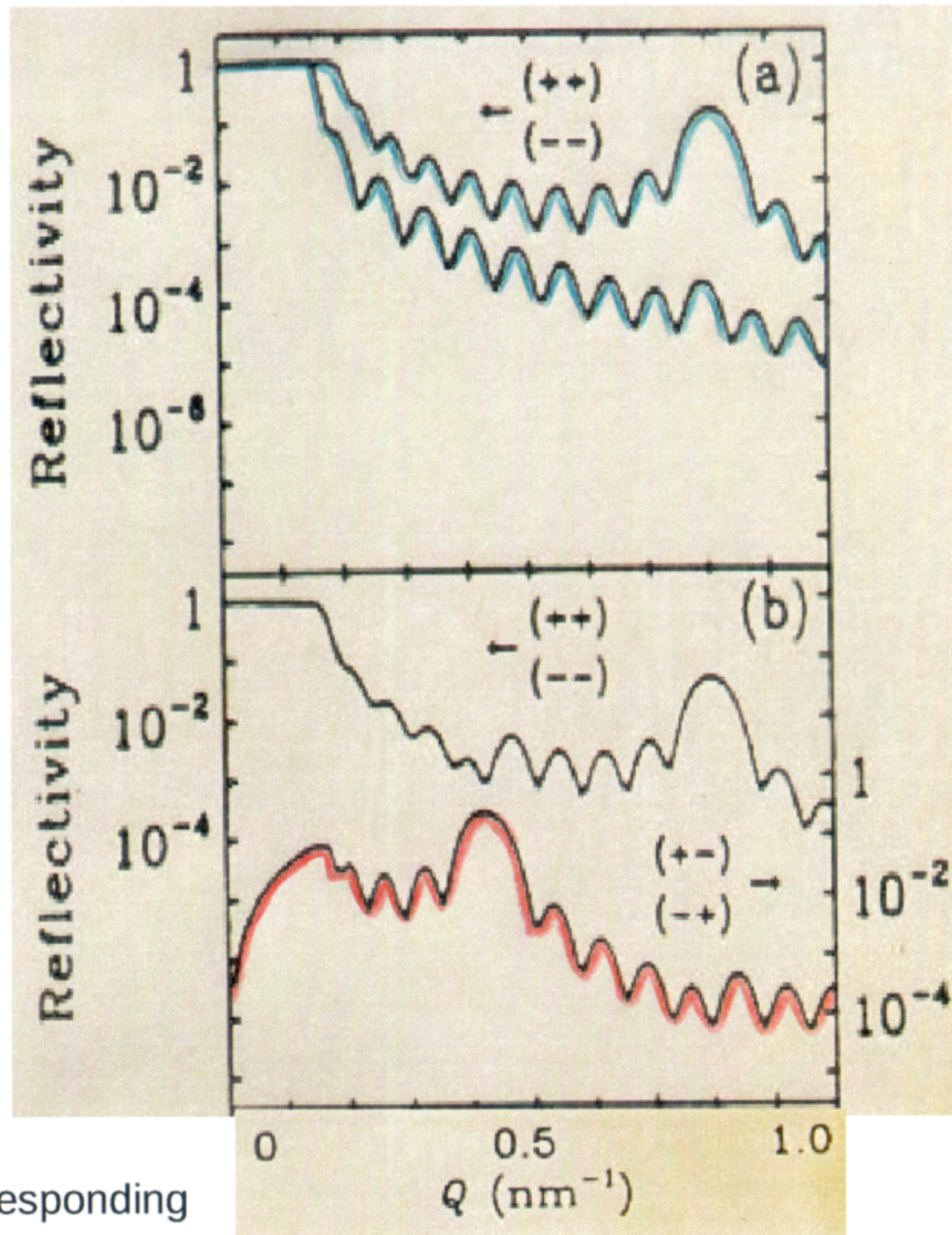
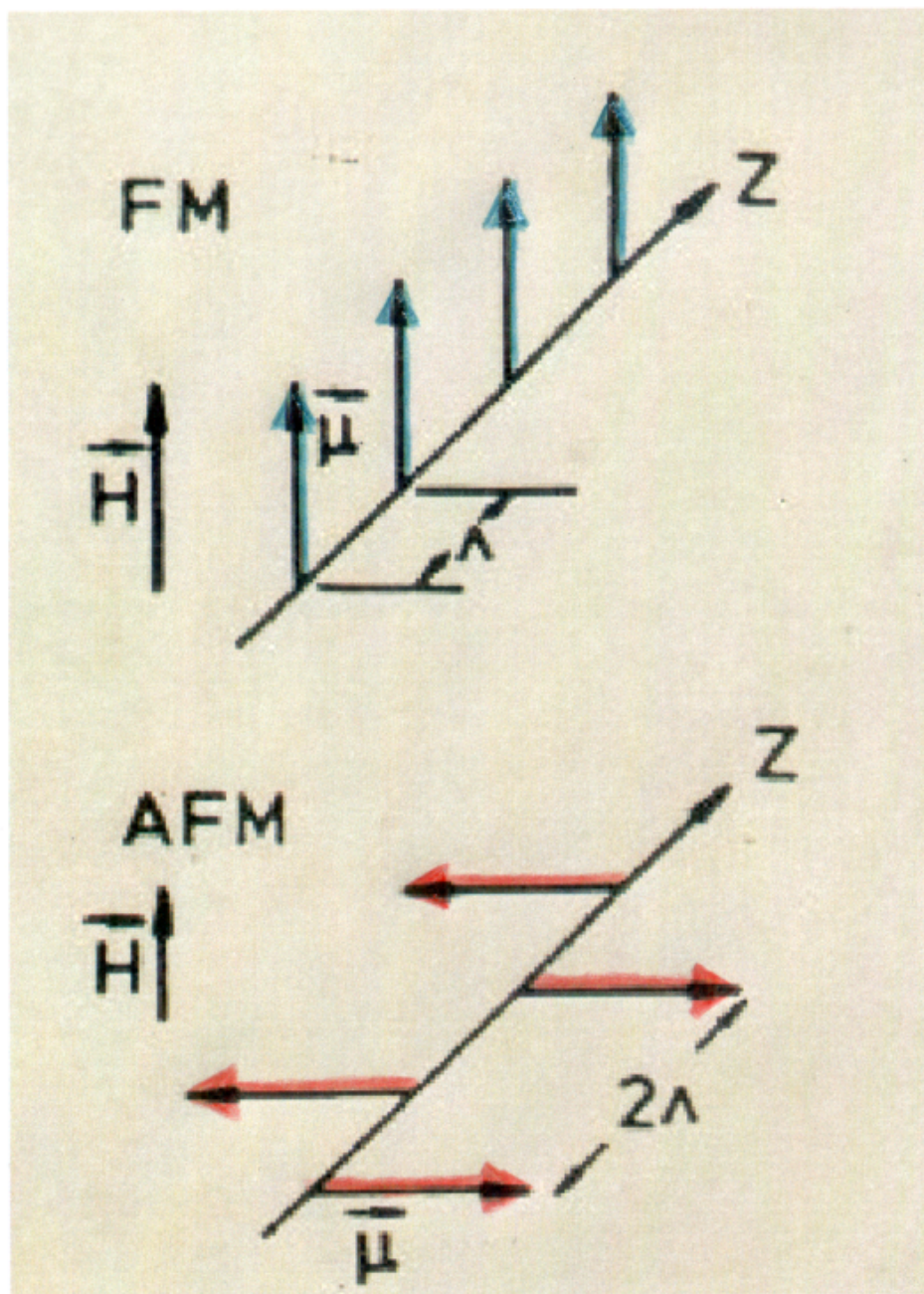
$$F^{\pm\pm} \propto \sum_{j=1}^N [b_{sj} \pm p_{sj} \cos \phi_j] e^{iQ u_j}$$

$$F^{\pm-} \propto \sum_{j=1}^N p_{sj} \sin \phi_j e^{iQ u_j}$$



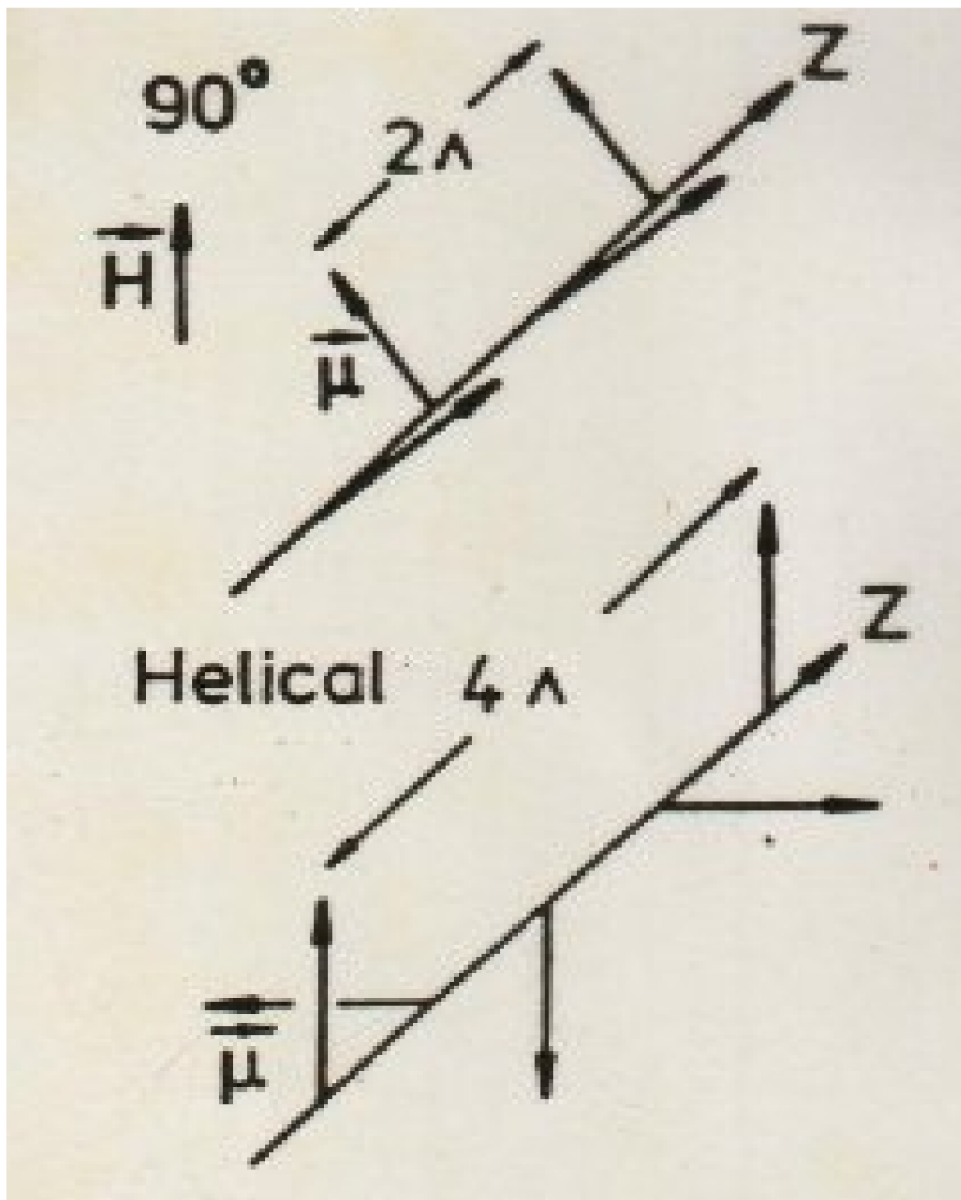
The above diagram illustrates a particularly useful configuration resulting in the ability to determine not only the magnitude of the net magnetization in each of the successive planes in a layered material, but also the direction of that magnetic moment.



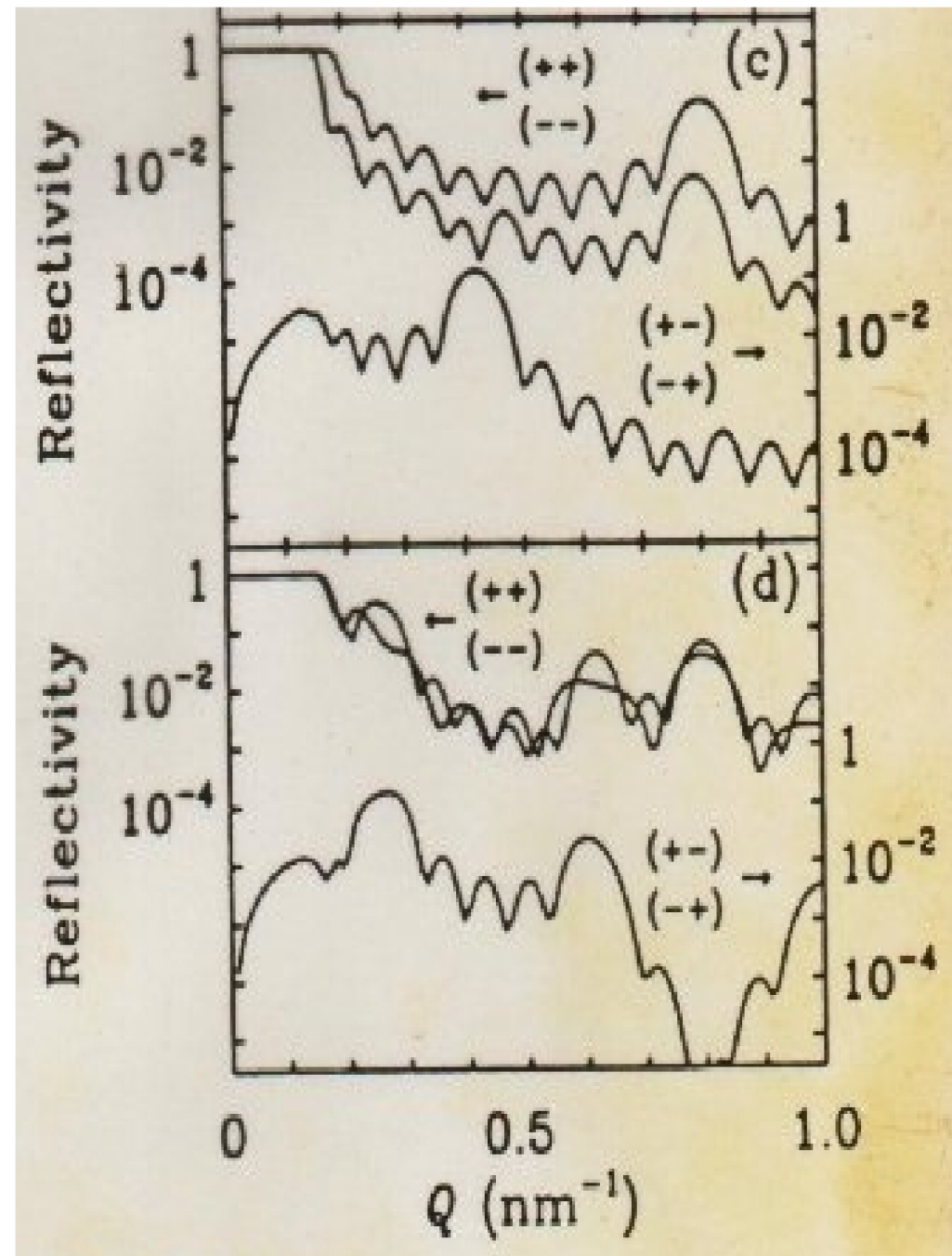


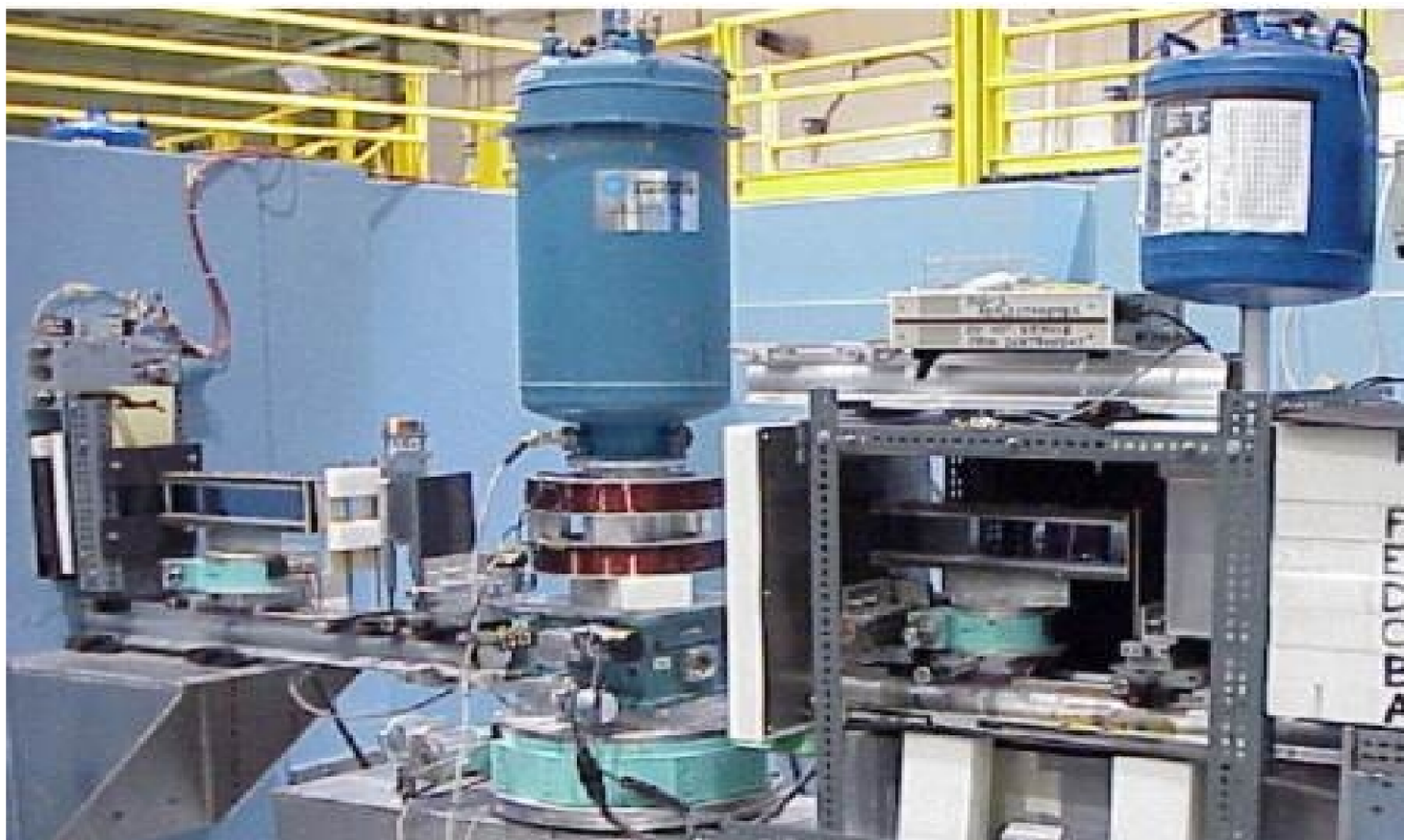
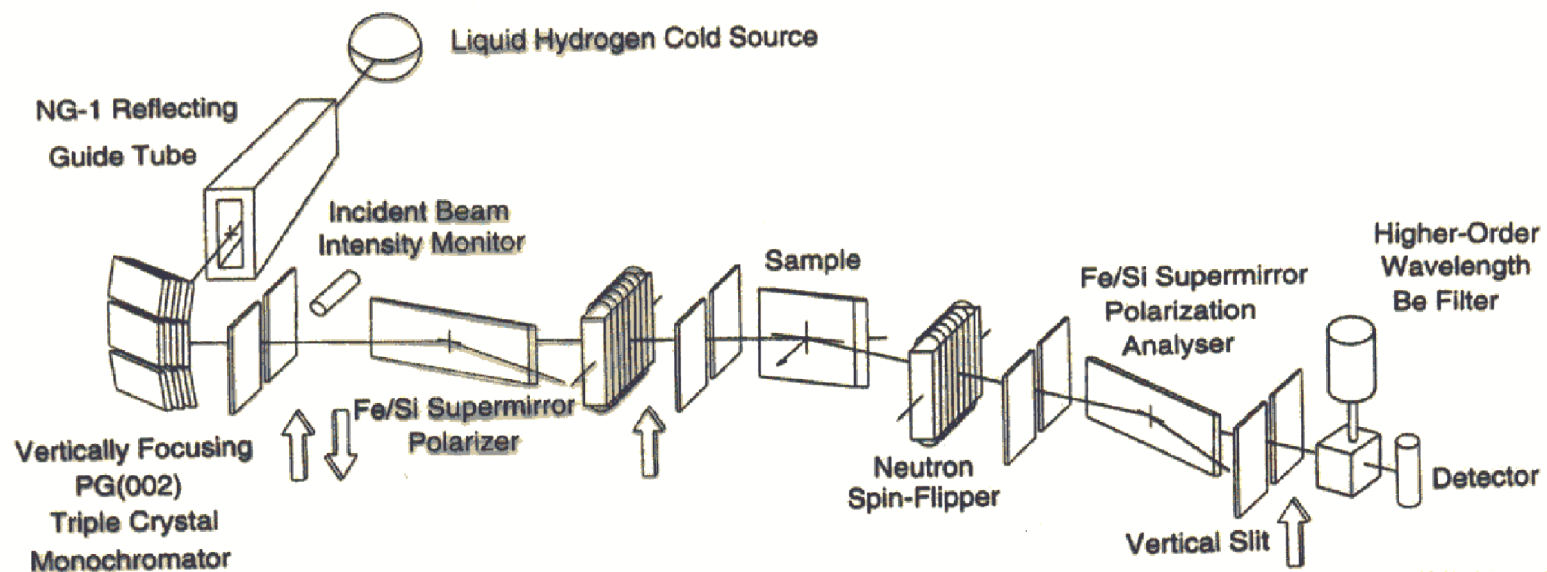
Two basic magnetic structures and their corresponding spin-dependent polarized neutron reflectivity curves (after Ankner, Schreyer, Majkrzak, and Zabel).





Two more magnetic structures and their corresponding spin-dependent polarized neutron reflectivity curves (after Ankner, Schreyer, Majkrzak, and Zabel).





# **Scientific areas in which neutron reflectometry has been applied at the NCNR**

(not necessarily a comprehensive account!)

<> Polymer Science

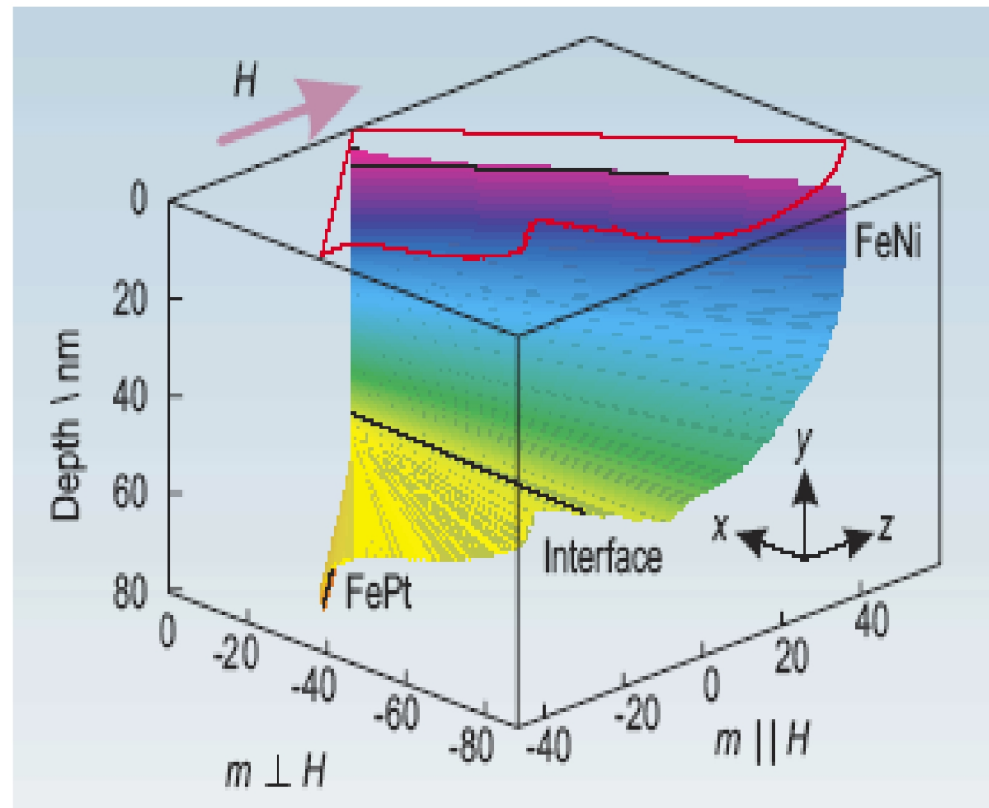
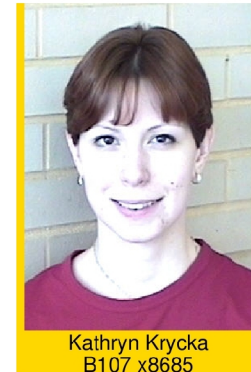
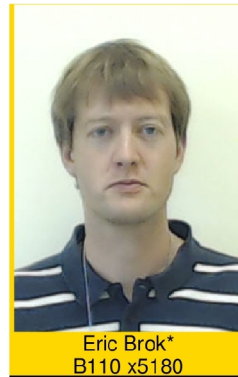
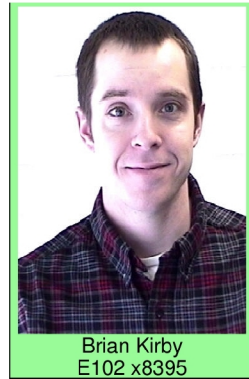
<> Magnetism

<> Biology

<> Electrochemistry and Photovoltaics



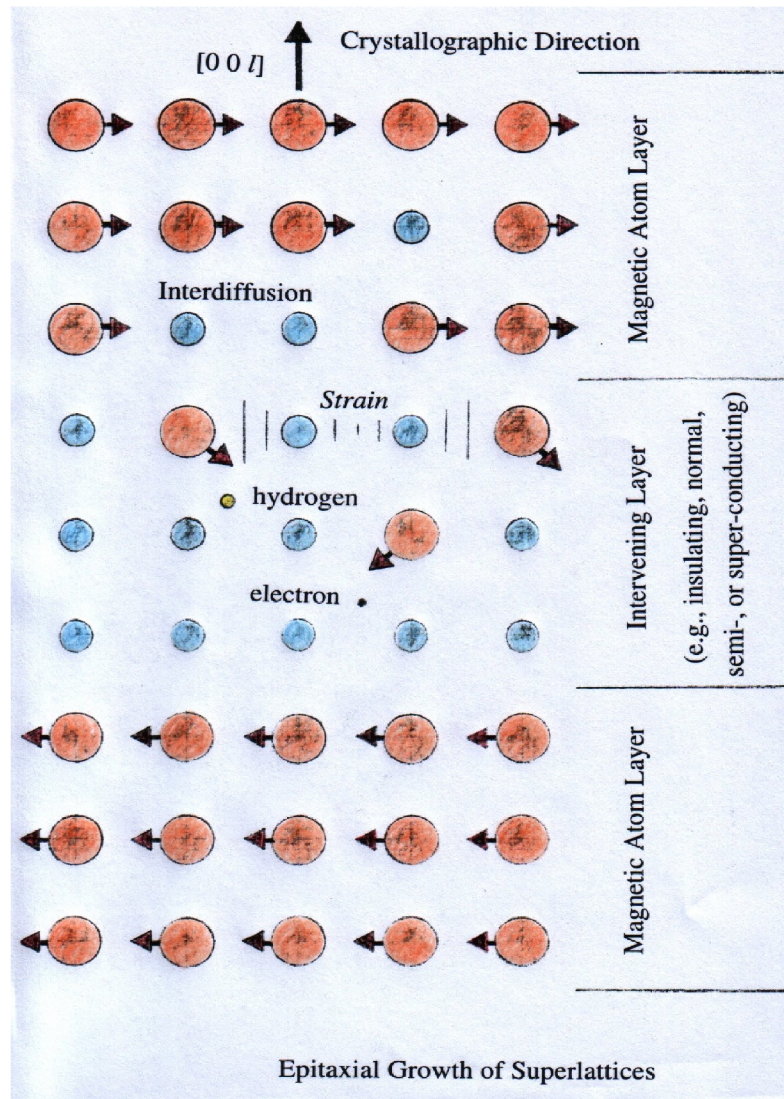
# Magnetism



(after O'Donovan et al.)

# New directions in science – synthetic superlattices

The same developments in physical vapor deposition methods were also being applied to the fabrication of composite layered systems (in some cases with atomic layer accuracy by molecular beam epitaxy) that do not occur in nature but which could be tailored to study fundamental physical phenomena in a controlled, systematic way.

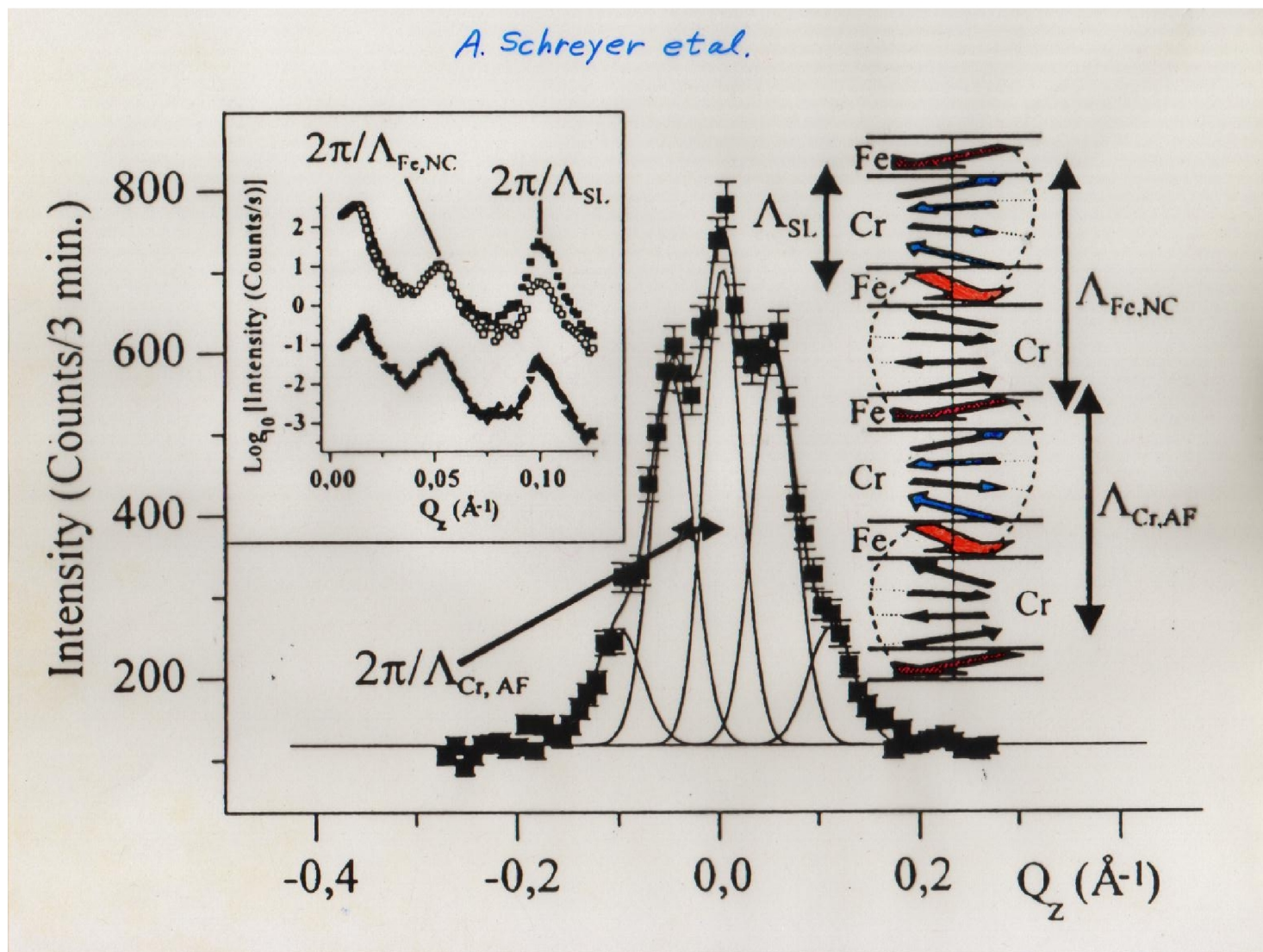


By means of molecular beam epitaxial growth in ultrahigh vacuum and other thin film deposition techniques, it is possible to construct synthetically layered systems tailored to study specific types of interactions of interest in hard condensed matter. For instance, how two separated regions made up of ferromagnetic atomic planes interact with one another across an intervening region of atomic planes of a material that is superconducting or semi-conducting can be studied by analysis of the polarized neutron reflectivity -- as a function of temperature, applied magnetic field magnitude and direction, or other parameter such as the thickness of the intervening layer.

There exists a considerable body of work on systems prepared in this manner.

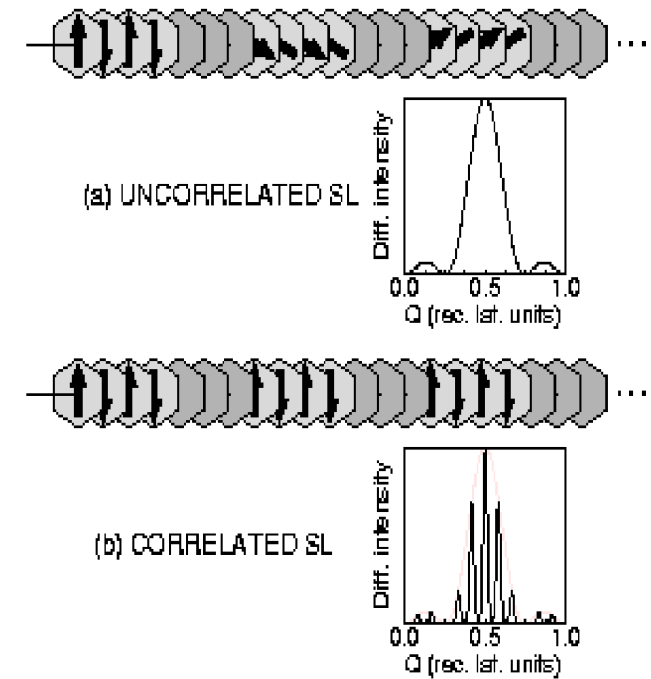
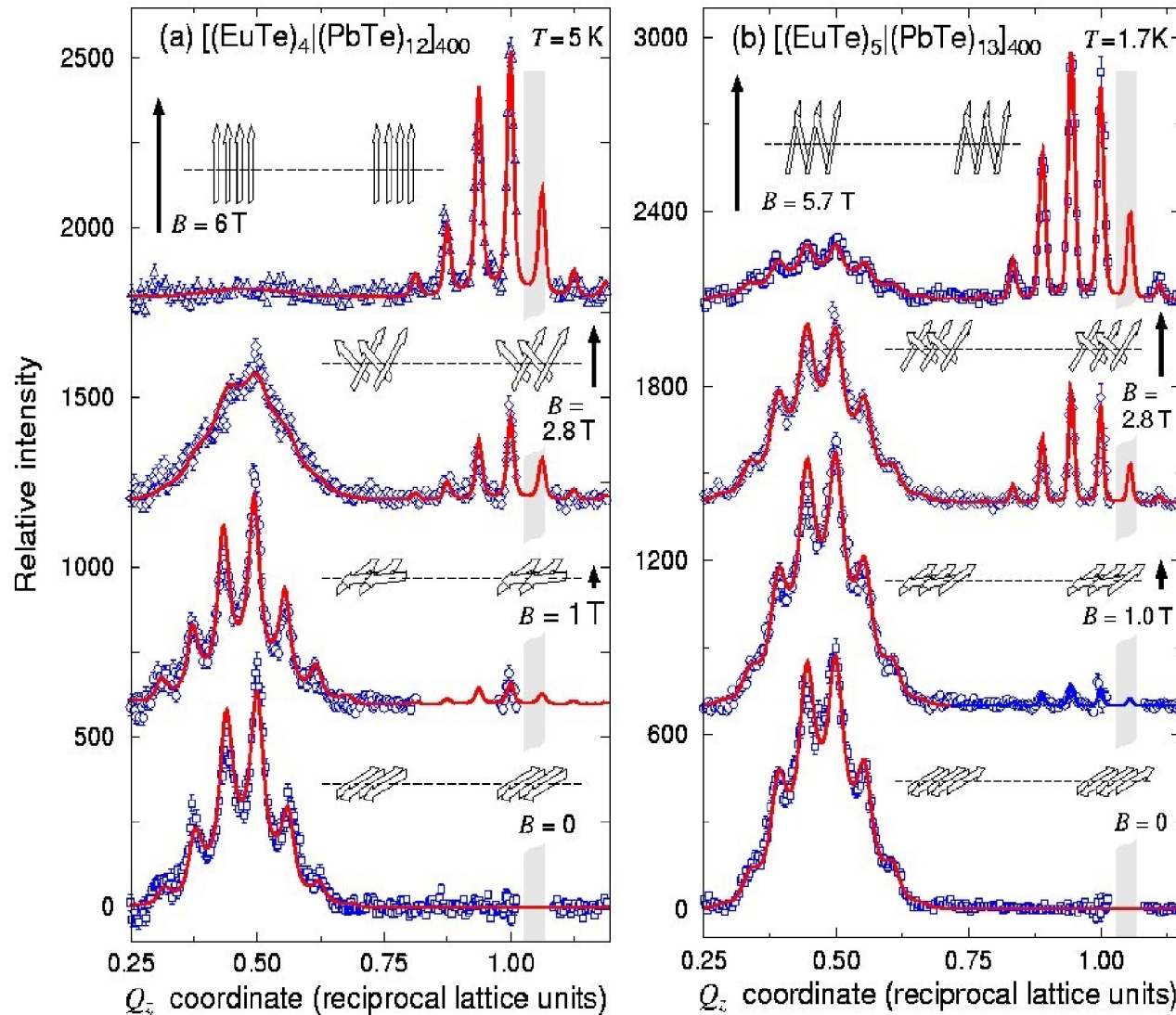


# Magnetic structure of unit bilayer



In this particular example, each ferromagnetic Fe layer consists of several atomic planes -- the relative orientations of these layers to one another within the overall layered system is deduced principally from the relatively low- $Q$  polarized neutron reflectivity data (inset). The intricate modulated antiferromagnetic structure of the Cr atomic planes within the intervening layers is revealed primarily in the higher- $Q$  polarized neutron diffraction pattern.

# Magnetic multilayers -- interlayer correlation



Remarkably detailed information about magnetic structure on an inter-atomic length scale can be obtained from polarized neutron reflection and diffraction studies. (Polarized neutron reflection data on magnetic semiconductor superlattices by Henryk Kepa et al..)



# Realization of ground-state artificial skyrmion lattices at room temperature

D. A. Gilbert,<sup>1,2</sup> B. B. Maranville,<sup>2</sup> A. L. Balk,<sup>3,4</sup> B. J. Kirby,<sup>2</sup> P. Fischer,<sup>5,6</sup>  
D. T. Pierce,<sup>3</sup> J. Unguris,<sup>3</sup> J. A. Borchers,<sup>2</sup> and K. Liu<sup>1</sup>

Moore's Law has been the icon of the computer revolution for nearly 50 years, but recent challenges with heat management and miniaturization have signaled its impending end. Spintronics – data and logic technologies that use the electron spin, in addition to the electron charge – offer a new approach to ultra-low power information technologies that may reinvigorate Moore's Law. One promising spintronic technology is the magnetic skyrmion. Skyrmions are specialized configurations of magnetic moments into topologically-protected structures; a typical skyrmion structure, shown in Fig. 1, possesses a core and perimeter with opposite out-of-plane spin orientations, and a closed, continuous in-plane winding of magnetic moments between. These structures can be realized on the atomic scale, moved with very low electrical current densities, and are robust against moderate perturbations including stray fields and system defects. These make skyrmions very attractive for ultra-low power, high-density data storage and logic technologies. A key challenge to the development of skyrmion-based memory and logic devices is achieving skyrmion structures stable at ambient conditions (room temperature and no magnetic field).

Recently, we have realized ground-state magnetic skyrmions stable at ambient conditions by nanopatterning [1]. Specifically, cobalt nanodots with diameters of 560 nm and heights of 30 nm are patterned. The magnetic 'vortex' configuration within these dots, shown in Fig. 1 (red), form a closed winding structure, with an out-of-plane core, which is stable over a wide range of temperatures. However, a vortex lacks an out-of-plane perimeter, distinguishing it from a skyrmion. By placing a vortex-state nanodot on top of a magnetic film, the loop structure and core can be imprinted into the film. Thus, by designing a film with an out-of-plane orientation, the imprinted structure at the interface has a closed loop structure with an out-of-plane core and perimeter, e.g. a skyrmion. To prove this claim and demonstrate its viability for application, three pieces of evidence must be shown: (1) the direction of circulation of the loop structure, called the circularity, must be controllable, (2) the orientation of the core, called the polarity, relative to the perimeter must be controllable, and (3) the loop structure must, in-fact, be imprinted into the film underlayer.

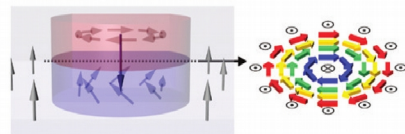


**FIGURE 1:** Diagram of an artificial skyrmion. Vortex dot is shown in red. The imprinted region (blue) that forms a skyrmion with the underlayer is shown in grey.

Samples were prepared by a three-step process. In step one, multilayer films of  $[\text{Co}(0.5 \text{ nm})/\text{Pd}(1 \text{ nm})]_{10}$  were grown on naturally oxidized Si substrates; the multilayer structure gives the film a preferred out-of-plane orientation – called the perpendicular magnetic anisotropy (PMA). In the second step, hexagonal arrays of nano-holes with a diameter of 560 nm and center-to-center spacing of 1000 nm were patterned into a  $\approx 400 \text{ nm}$  thick polymer layer that was spin-coated onto the Co/Pd film. The holes are shaped like a circle, with one side made flat; the asymmetric structure has been previously used to realize circularity control. Next, the sample was irradiated by 1 keV  $\text{Ar}^+$  plasma, which suppresses the PMA in the regions exposed by the holes, while the regions still protected by polymer retain their PMA. During the third step, 32 nm of Co was deposited into the holes and the polymer mask removed, realizing asymmetric Co dots grown over the irradiated regions. Once the sample was fabricated, the skyrmion state was configured by a designed field sequence. First, the Co/Pd underlayer was saturated in the positive out-of-plane direction using a large out-of-plane magnetic field. Then, the out-of-plane field was removed and a small in-plane magnetic field was applied to saturate the dots parallel to the flat edge. At this point a small out-of-plane magnetic field was applied anti-parallel to the underlayer. The in-plane magnetic field was removed, nucleating a vortex, with the core biased to be anti-parallel to the underlayer. Lastly, the out-of-plane magnetic field was removed, leaving the system at remanence (no magnetic field) in a vortex state dot, with a core anti-parallel to the underlayer, and the region under the dot having no PMA.

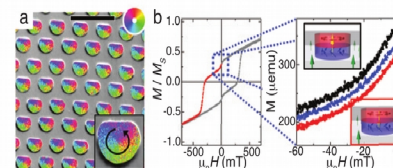


**FIGURE 2:** (a) SEMPA image of the asymmetric dot array. Color wheel indicates magnetization direction. (b) Remnant magnetization curve, with the core parallel, anti-parallel, and random relative to the underlayer, shown in black, red and blue, respectively ( $1 \text{ emu} = 10^{-3} \text{ A m}^2$ ).

As stated above, circularity control was achieved by using the asymmetric dot structure. Applying an in-plane magnetic field parallel to the flat edge of the dot defines the nucleation site for the vortex and thus the circularity. Micrographs taken using scanning electron microscopy with polarization analysis (SEMPA) are shown in Fig. 2(a). The colors indicate the direction of the magnetization; the common color wheel for each of the dots indicates a common circularity of the magnetization. Other magnetic imaging technique and magnetometry measurements confirm the circularity control seen in SEMPA.

Recalling the magnetic field sequence to set the skyrmion state, polarity control is determined during the vortex nucleation by the small magnetic field applied anti-parallel to the underlayer. To demonstrate polarity control, the remanent magnetization was measured with the core parallel and anti-parallel to the underlayer. Specifically, the sample was prepared as discussed above, with the core anti-parallel to the underlayer and the out-of-plane magnetization measured as the magnetic field was decreased from remanence to negative saturation. In this case the magnetization of the core and perimeter are opposite, and thus subtract when measured together. Then, the sample was prepared again, but with the biasing field applied parallel to the underlayer. In contrast to the former case, the magnetization from the core and underlayer are expected to be parallel and add together. In a third measurement no biasing field was applied and the polarity was random. Indeed, as shown in Fig. 2(b), the skyrmion state, with the core and underlayer anti-parallel, has the smallest magnetization; the vortex state with the core and the underlayer oriented parallel has the largest magnetization; the random polarity falls in-between the parallel and anti-parallel configurations. This confirms the biasing field indeed defines the polarity.

Lastly, and arguably most crucially, the imprinting of the skyrmion was demonstrated using polarized neutron reflectometry (PNR), performed on the MAGIK reflectometer. PNR is a technique that uses scattering to extract depth-profiles from layered systems and possesses sensitivity to nuclear and magnetic features. The measured data are shown as dots in Fig. 3(a). A model was made to simulate the nominal structure and the reflectivity pattern calculated. By iteratively changing the model and comparing the calculated reflectivity to the data, the model converges on an accurate representation of the physical system. The

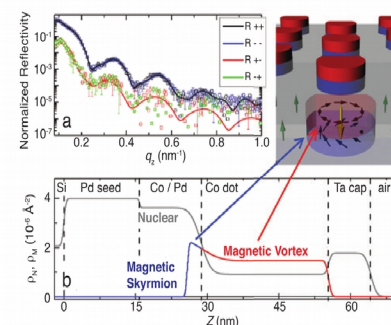


**FIGURE 3:** (a) Measured (dots) and simulated (lines) reflectometry, and (b) converged depth profile.

converged model is shown in Fig. 3(b), and the corresponding reflectometry is shown as the solid lines in Fig. 3(a), which agree well with the experimental data ( $\chi^2 < 1.2$ ). The converged model correctly identifies the designed structure, giving confidence in its accuracy. More importantly, the model identifies the magnetization of the Co dot – as expected – but also shows that the magnetization extends  $\approx 3 \text{ nm}$  below the  $[\text{Co}/\text{Pd}]/\text{Co}$ -dot interface. This imprinted magnetic feature is the first direct evidence of the imprinted magnetic skyrmion. Further, the imprinted skyrmion is expected to be stable while the dots and underlayer are stable (ambient conditions up-to approximately  $300^\circ\text{C}$ , and  $300 \text{ mT}$ ). Theoretical modeling using NIST's object oriented micromagnetic framework (OOMMF) confirms that the imprinted structure extends 2 nm into the underlayer.

In summary, we have successfully achieved room temperature artificial skyrmion lattices in the ground state over extended areas, defining a platform for exploring skyrmion properties and behaviors as well as the use of skyrmion lattices in novel technological concepts. The system is constructed by fabricating circularity controlled Co nanodots on a selectively irradiated Co/Pd underlayer with PMA. Circularity control is imposed by the fabrication of asymmetric dots and confirmed by microscopy. Polarity control is realized by the application of a small out-of-plane magnetic field during the vortex nucleation, and demonstrated in the magnetization curves. The imprinted skyrmion lattice in the Co/Pd is directly confirmed by PNR, and is quantitatively consistent with micromagnetic simulations. These artificially constructed skyrmion lattices are stable over a wide range of magnetic fields and temperatures, including room temperature and zero magnetic field. These foundational results present a new path in skyrmion research on the meso-scale, at and above room temperature.

## Reference

- [1] D. A. Gilbert, B. B. Maranville, A. L. Balk, B. J. Kirby, P. Fischer, D. T. Pierce, J. Unguris, J. A. Borchers, K. Liu, *Nature Communications* **6**, 8462 (2015).

<sup>1</sup> University of California, Davis, CA 95616

<sup>2</sup> NIST Center for Neutron Research, National Institute of Standards and Technology, Gaithersburg, MD 20899

<sup>3</sup> Center for Nanoscale Science and Technology, National Institute of Standards and Technology, Gaithersburg, MD 20899

<sup>4</sup> University of Maryland, College Park, MD 20742

<sup>5</sup> Lawrence Berkeley National Laboratory, Berkeley, CA 94720

<sup>6</sup> University of California, Santa Cruz, CA 94056



# Beyond the interface limit: structural and magnetic depth profiles of voltage-controlled magneto-ionic heterostructures

D. A. Gilbert,<sup>1</sup> A. J. Grutter,<sup>1</sup> E. Arenholz,<sup>2</sup> K. Liu,<sup>3</sup> B. J. Kirby,<sup>1</sup> J. A. Borchers,<sup>1</sup> and B. B. Maranville<sup>1</sup>

Oxidation is a common process that changes virtually every quality of a material, including optical, mechanical, electrical, thermal, and magnetic properties. For example, metals are typically shiny, ductile, conductive, and can be magnetic, while metal oxides can be matte or transparent, brittle, insulating, and are frequently non-magnetic. Controlling oxidation by electric fields offers an opportunity for manipulating the material properties with the flip of a switch. This is the premise behind both memristors, which use a voltage to control oxygen distributions and tune electrical conductivity, and magneto-ionic devices [1-5], which similarly use a voltage to tune magnetic properties. These technologies work by recognizing that metal oxides are ionic solids with oxygen atoms that have a net charge and thus are sensitive to electric fields. Applying a strong electric field can thus alter the oxygen ion distribution, changing the material properties. Recent investigations [1, 2] have demonstrated magneto-ionic control in ultra-thin Hall bar structures (thicknesses < 1 nm). In these studies, the films prefer to have the magnetization oriented out of the plane of the film; using an electric field to drive oxygen into the interface with a neighboring oxide material causes the magnetization to rotate into the plane of the film. Devices built on this control have been proposed for ultra-high density, low-power data storage technologies. However, for broader applications, ion-based control must be demonstrated in thicker films with bulk-like properties, and it is unclear how the magneto-ionic control mechanism works in this regime.

In this work, we demonstrated magneto-ionic effects in comparably thick (15 nm) cobalt films [5]. Using an applied voltage, oxygen was driven from a GdO<sub>x</sub>/AlO<sub>x</sub> film into the neighboring Co film, which then becomes non-ferromagnetic CoO<sub>x</sub>. Magnetometry revealed that, while some of the magnetic properties are recovered, others are not. Using polarized neutron reflectometry (PNR), the depth-resolved oxygen distribution and magnetization were directly mapped, providing a physical picture to explain the observed behavior.

Thin-films with a structure Si/Pd(50 nm)/AlO<sub>x</sub>(1000 nm)/GdO<sub>x</sub>(2 nm)/Co(15 nm)/Pd(20 nm) were grown by sputtering and e-beam evaporation at the Center for Nanoscale Science and Technology. Electro-thermal (E+T) conditioning was performed by heating the sample to 230 °C and applying 40 V across the Pd layers for 15 min. The measured PNR reflection and

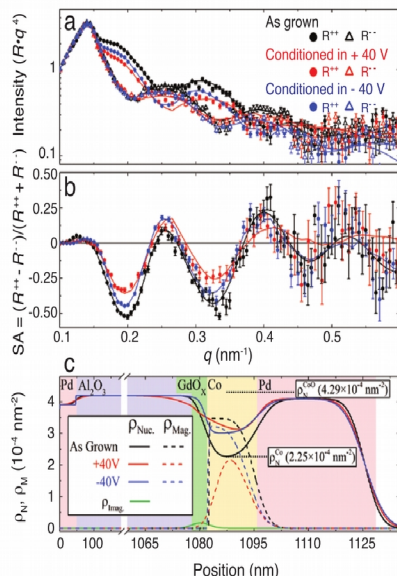


**FIGURE 1:** (a) Fitted PNR data scaled by  $q^2$  and (b) spin asymmetry for the sample as-grown and after electro-thermal conditioning. (c) Depth-dependent real and imaginary nuclear SLD ( $\rho_N$  and  $\rho_{imag}$ ), and magnetic SLD ( $\rho_M$ ) extracted from the PNR. In (a) and (b) the experimental data are shown as symbols, and the lines are fits corresponding to the depth profile shown in (c).

spin-asymmetry (SA) for the as-grown sample, the sample after applying +40 V (anode on the top surface), and sequential -40 V are shown in Figs. 1(a) and (b), respectively. The SA, which is proportional to the product of the magnetization and nuclear scattering length density (SLD), is shown to decrease after the +40 V treatment and partly recover after subsequently applying -40 V. Using the Refl1d software package, models for the three treatments (as-grown, after +40 V, and after sequential +/- 40 V) were fitted in parallel, Fig. 1(c). The fitted model for the as-grown sample closely matches the designed structure and the bulk nuclear SLD for these materials, lending confidence to its accuracy. After the initial +40 V treatment the nuclear SLD increases in the Co layer, the GdO<sub>x</sub>/Co interface becomes much broader, and the

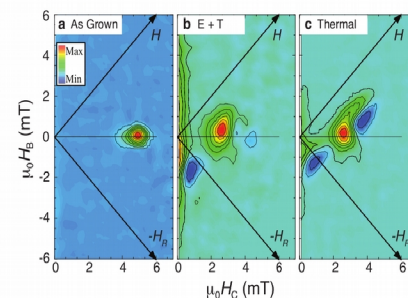


**FIGURE 2:** FORC distributions for the sample (a) as-grown, (b) after +/- 40 V conditioning, and (c) after thermal-only conditioning.

magnetic SLD decreases (38 %), most prominently at the interface (80 %). This is consistent with oxygen being moved by the electric field from the GdO<sub>x</sub> layer into the Co layer, forming non-magnetic CoO<sub>x</sub>. Subsequently applying -40 V restored the sharp nuclear interface and most of the magnetism (92 %). However, oxygen migration was irreversible for thicknesses greater than 10 nm. Measurements performed using a thermal-only treatment showed a much smaller effect, demonstrating that the electric field moves oxygen into and out of the Co layer depending on its polarity.

Magnetic first order reversal curve (FORC) measurements of the as-grown sample, the +/- 40 V sample, and a thermally treated sample (230 °C for 30 minutes) are shown in Fig. 2. The FORC plots, in a general sense, are a map of all hysteretic events that exist within a system and provide detailed information regarding the magnetic reversal process. The FORC distribution for the as-grown sample shows only a single feature, indicating a single magnetic phase. By comparison the electro-thermal and thermal-only samples show two features, with a new feature located at  $H_C = 0$  that specifically identifies reversible features. In general, reversible features indicate the absence of hysteresis and are often manifest when the magnetism is measured along a hard axis. We suggest that the new reversible phase is the result of a decoupling between grains within the Co film plane. Specifically, the film is comprised of many nano-scale magnetic grains, each with their own randomly oriented magnetocrystalline anisotropy. Typically, magnetic exchange coupling between neighboring grains can cause the film to behave as a single coherent structure. The small amount of residual oxygen may be interrupting the exchange interaction, allowing the magnetocrystalline anisotropy of each grain to dictate its orientation.

We suggest the reduced exchange interaction and irreversibility for thicknesses of > 10 nm is due to a screening effect of the electric field, as shown in Fig. 3. Specifically, the +40 V electro-thermal treatment moved oxygen deep into the film, diffusing quickly at grain surfaces and more slowly in the bulk. During the -40 V treatment the oxygen migrated quickly off of the grain surface,

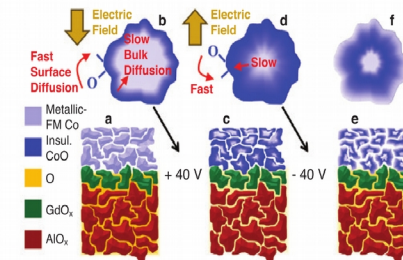


**FIGURE 3:** Cross-section view of (a) the as grown film, (b) a single grain during +40 V treatment, (c) the film after +40 V treatment, (d) a single grain during subsequent -40 V treatment, and (e, f) cross section and grain after -40 V treatment. Colors identify AlO<sub>x</sub> (red), GdO<sub>x</sub> (green), metallic FM Co (light blue), insulating non-FM CoO<sub>x</sub> (blue), and interstitial oxygen (orange); large gold arrow indicates the electric field. Illustration (e) emphasizes fast surface migration, identified by the red arrows, and slow bulk diffusion, indicated by the grey arrows.

leaving a metallic Co shell. This shell screens the electric field via the Faraday effect, thus halting any further migration and trapping oxygen within each grain and deeper in the film. This mechanism suggests an unexplored role of the microstructure, and a potential limit to these technologies.

In summary, we have realized a thin film magneto-ionic device built on a thick (15 nm) Co film. Semi-reversible control of the magnetism resulting from oxygen migration was demonstrated and directly mapped using polarized neutron reflectometry. First order reversal curve measurements showed that the nominally similar sample possessed two phases, while the as-grown sample had only one. Based on a fundamental understanding of the nature of electric fields and oxygen migration, a physical picture was presented which supports the results. This work thus demonstrates that ionic devices with 'active' layers thicker than a few atom layers are still viable, thus opening new opportunities for future ion-based technologies.

## References

- [1] U. Bauer, L. Yao, A. J. Tan, P. Agrawal, S. Emori, H. L. Tuller, S. v. Dijken, G. S. D. Beach, *Nature Mater.* **14**, 174 (2015).
- [2] C. Bi, Y. Liu, T. Newhouse-Illige, M. Xu, M. Rosales, J. W. Freeland, O. Myasov, S. Zhang, S. G. E. t. Velthuis, W. G. Wang, *Phys. Rev. Lett.* **113**, 267202 (2014).
- [3] D. A. Gilbert, J. Olamit, R. K. Dumas, B. J. Kirby, A. J. Grutter, B. B. Maranville, E. Arenholz, J. A. Borchers, K. Liu, *Nature Commun.* **7**, 11050 (2016).
- [4] A. J. Grutter, D. A. Gilbert, U. S. Allan, E. Arenholz, B. B. Maranville, J. A. Borchers, Y. Suzuki, K. Liu, B. J. Kirby, *Appl. Phys. Lett.* **108**, 082405 (2016).
- [5] D. A. Gilbert, A. J. Grutter, E. Arenholz, K. Liu, B. J. Kirby, J. A. Borchers, B. B. Maranville, *Nature Commun.* **7**, 12264 (2016).

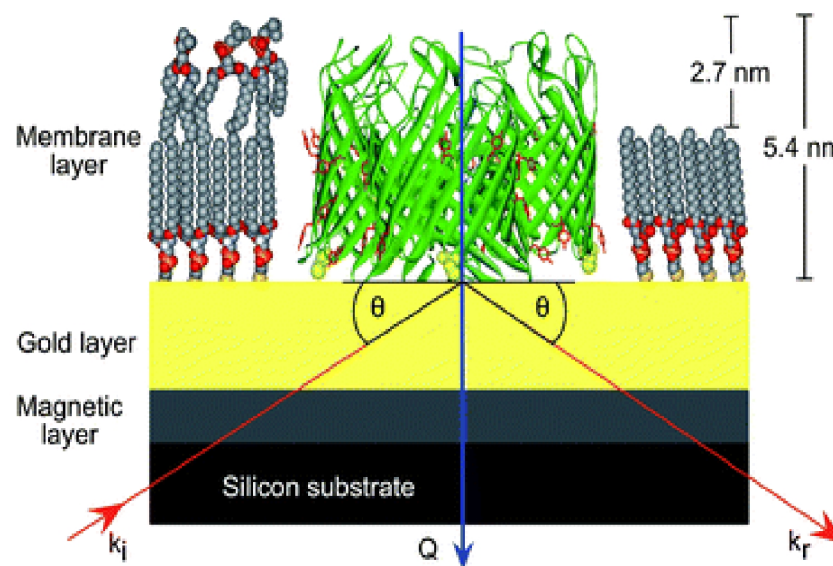
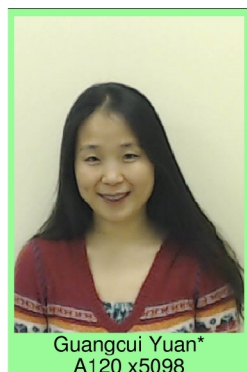
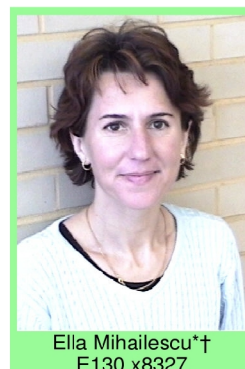
<sup>1</sup> NIST Center for Neutron Research, National Institute of Standards and Technology, Gaithersburg, MD 20899

<sup>2</sup> Advanced Light Source, Lawrence Berkeley National Laboratory, Berkeley, CA 94720

<sup>3</sup> University of California, Davis, CA 95616



# Mostly Soft Matter



(after Holt et al.)





# Polymer Science

Early on, colleagues from various institutions, including Tom Russell, Frank Bates, Anne Mayes, Spiros Anastasiadis, Mark Foster, and at NIST, Sushil Satija, Alamgir Karim, Wen Li Wu, and others made pioneering studies of polymer thin film systems using neutron reflectometry as a probe. Greg Smith and Bill Hamilton were also involved in some of this research. Polymer science has continued to be a mainstay of NR activities at the NCNR with regular contributors such as Bulent Akgun.

## Structure of symmetric polyolefin block copolymer thin films

Mark D. Foster,<sup>a)</sup> Mohan Sikka, Navjot Singh, and Frank S. Bates  
*Department of Chemical Engineering and Materials Science, University of Minnesota, Minneapolis, Minnesota 55455*

Sushil K. Satija and Charles F. Majkrzak  
*National Institute of Standards and Technology, Reactor Radiation Division, Gaithersburg, Maryland 20899*

(Received 5 February 1992; accepted 27 February 1992)

The microstructure of thin films of nearly symmetric poly(ethylene-propylene)-poly(ethylene) (PEP-PEE) diblock copolymers ( $f = 0.55$ , where  $f$  is the volume fraction of PEP) was characterized by neutron reflectometry (NR). A symmetric film structure in which the PEE block segregates preferentially to both interfaces is observed above and below the bulk order-disorder transition (ODT). Measurements at room temperature for several chain lengths,  $N$ , provide a real-space picture of the change in interdomain interfacial profiles associated with the crossover between the strong and weak segregation limits. The polymer/air and substrate/polymer interfaces are observed to induce an ordered microstructure even when the center of the film is disordered. The characteristic dimension of this near surface microstructure is larger than the corresponding bulk value for values of  $\chi N$  lying between those of the bulk Gaussian-to-stretched-coil and order-disorder transitions, where  $\chi$  is the segment-segment interaction parameter. This behavior is attributed to the correlation of large amplitude composition fluctuations in the film with the interfaces. A mean-field behavior prevails for  $\chi N < (\chi N)_{\text{GST,bulk}}$ , where some preferential segregation occurs at the interfaces, but the characteristic dimension once again matches that in the bulk.



Tom Russell, Frank Bates, and Mark Foster, CW from top left.



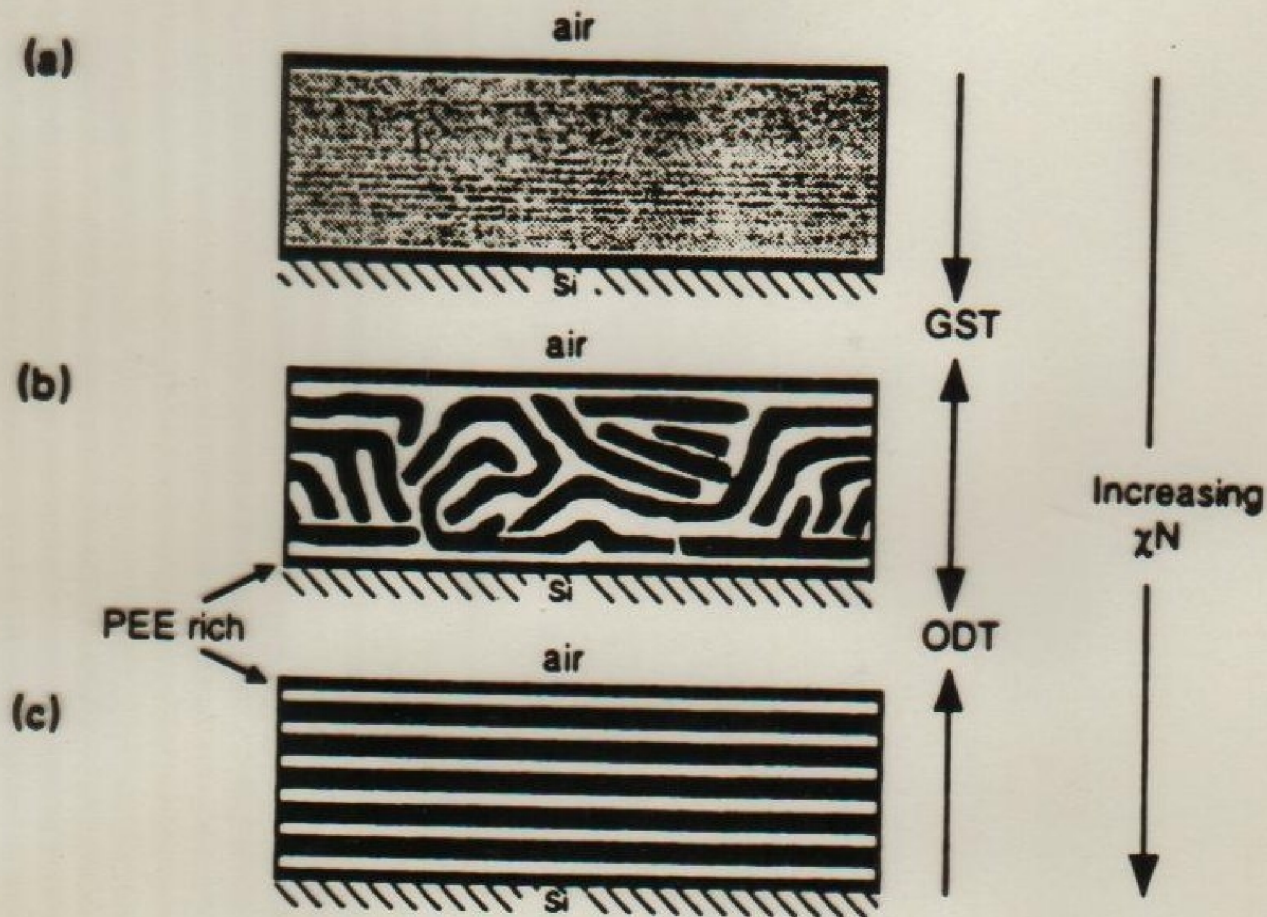


FIG. 5. Thin film morphologies for symmetric PEP-PEE diblock copolymers. (a) Interfacial segregation of PEE occurs for  $\chi N < (\chi N)_{\text{GST}}$ . The center of the film is spatially homogeneous. (b) For  $(\chi N)_{\text{GST}} < (\chi N) < (\chi N)_{\text{ODT}}$  the film contains a microstructured morphology that is oriented at the film interfaces. The range of the orientational correlation increases with increasing  $(\chi N)$ . (c) A lamellar microstructure that is highly oriented with the film interfaces exists when  $(\chi N) > (\chi N)_{\text{ODT}}$ .



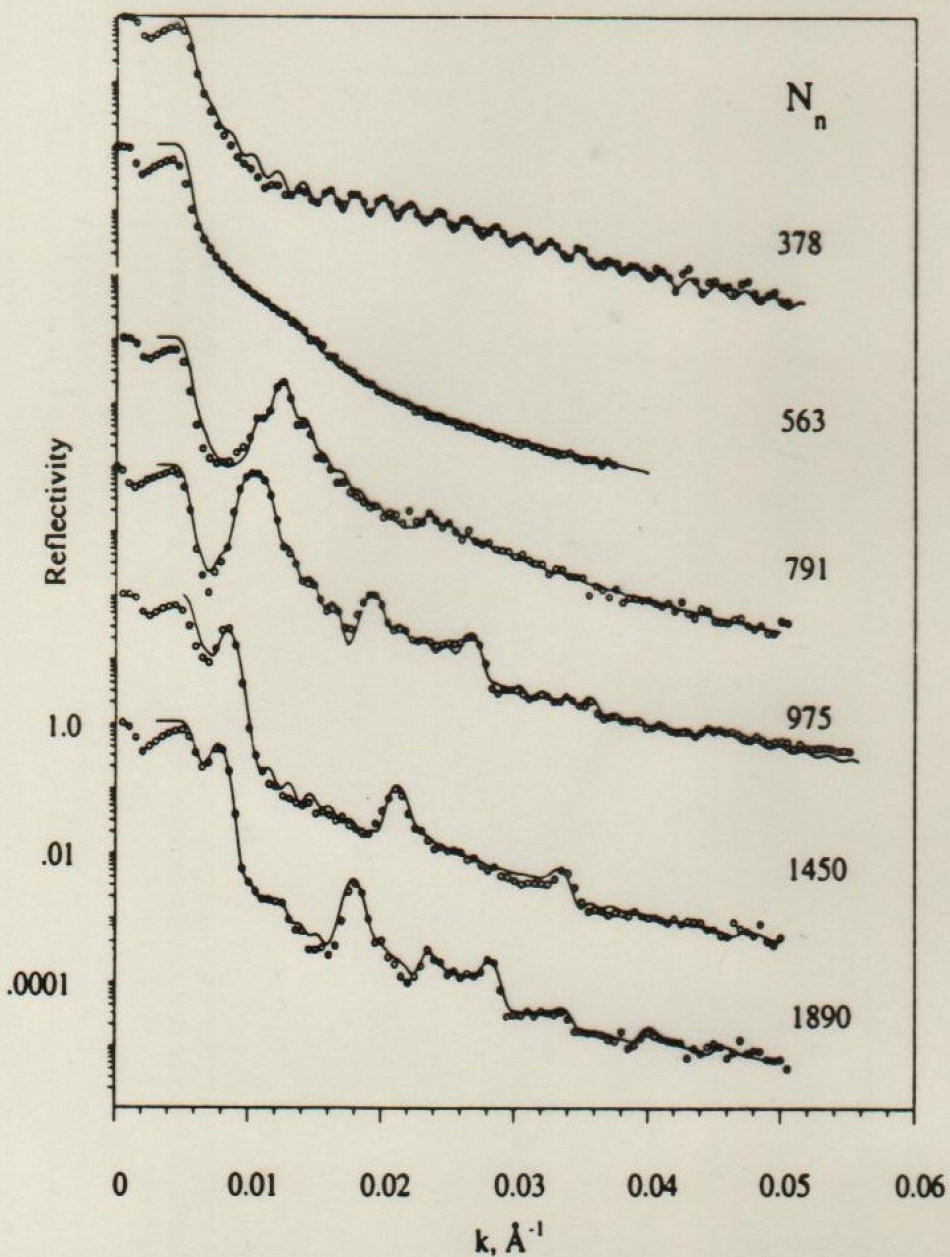


FIG. 8. Reflectivity data for six PEP-PEE chain lengths and the corresponding model curves used to infer concentration profiles illustrated in Fig. 9. The results for  $N < 1890$  have been shifted vertically. Poor agreement between the model curves and data in the vicinity of the critical wave vector stems from an experimental artifact that also produces the apparent lack of total reflectivity for  $k \lesssim k_c$  (Ref. 32).

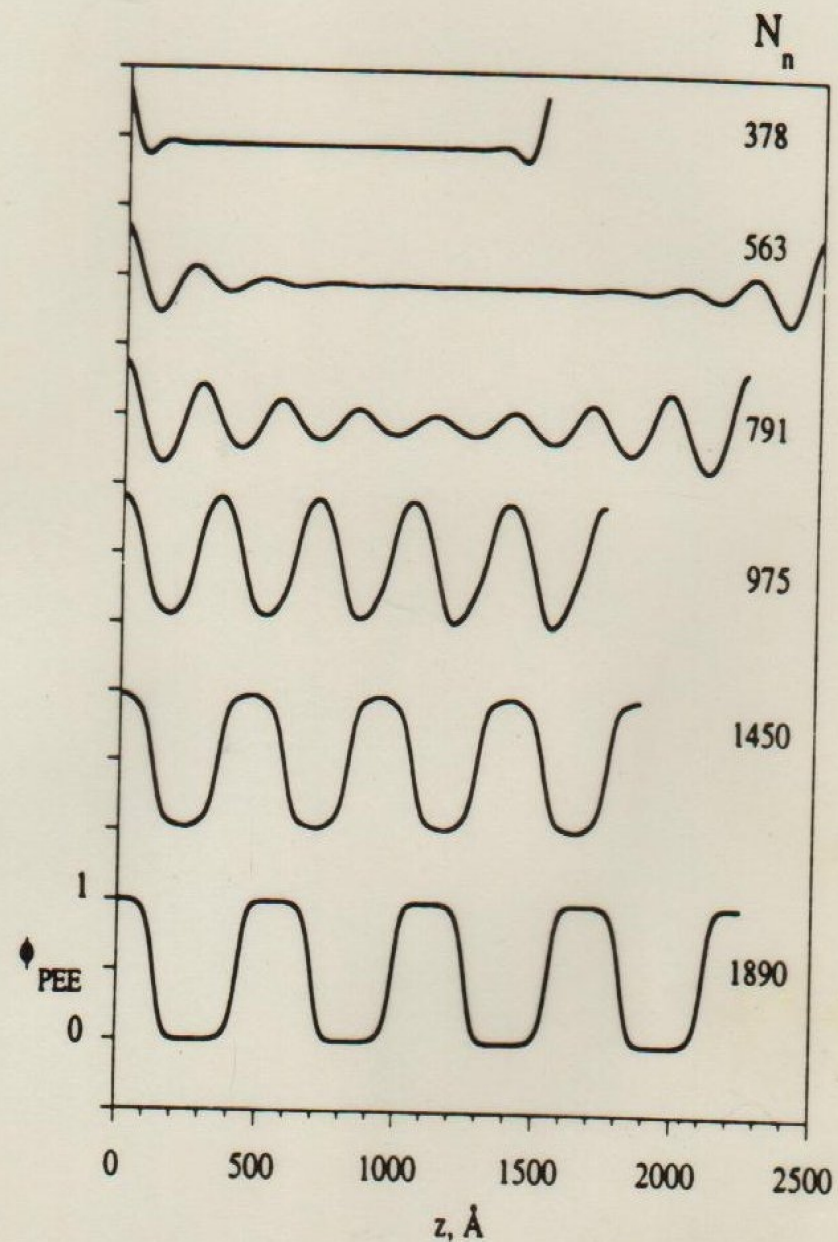


FIG. 9. Real space concentration profiles corresponding to the model curves shown in Fig. 8.



# Connecting polymer-solvent interactions to structural transformations during solvent vapor annealing of block polymer thin films

C. K. Shelton,<sup>1</sup> R. L. Jones,<sup>2</sup> J. A. Dura,<sup>3</sup> and T. H. Epps, III<sup>1,4</sup>

nSoft

Solvent vapor annealing (SVA) is a powerful technique for directing nanostructure ordering, orientation, and morphology in block polymer (BP) thin films for applications in emerging nanotechnologies such as nanolithographic masks, nanoporous membranes, nanotemplating, and organic optoelectronics. Swelling BP thin films with solvent vapor plasticizes polymer chains and reduces polymer glass transition temperatures ( $T_g$ ), thereby increasing chain mobility and allowing nanostructures to reorganize into well-ordered morphologies. With judicious control over factors including the solvent vapor composition, solvent vapor partial pressure, and swelling/deswelling pathways to influence the thermodynamics and kinetics of the polymer-solvent interactions, one can access a myriad of potential nanostructure conformations not obtainable by traditional thermal annealing alone. Additionally, SVA is ideal for BP systems that are susceptible to thermal transitions and degradation or require infeasible thermal annealing time scales. Therefore, we recently employed a combination of *in situ* small-angle neutron scattering (SANS) and neutron reflectivity (NR) to elucidate the importance of polymer-solvent interactions on morphology development during SVA of BP thin films [1]. Our results allowed us to glean key insights into the mechanisms of SVA and develop a more predictive approach to target desired nanostructure self-assembly.

Although the effects of SVA on BP self-assembly have been well researched, studies probing how solvent segregation into individual domains governs reorganization kinetics and thermodynamics have not been prevalent. Therefore, we used *in situ* neutron scattering to quantify the segregation of deuterated benzene (*d*-benzene) into the polystyrene (PS) and polyisoprene (PI) domains of PS-cylinder-forming poly(styrene-*b*-isoprene-*b*-styrene) (SIS) BP thin films as a function of atmospheric solvent concentration (solvent partial pressure divided by solvent vapor pressure [ $p/p_{\text{sat}}$ ]) [1]. Neutron scattering with solvent deuteration provided enhanced polymer-solvent contrast, in comparison to traditional X-ray experiments. From our neutron scattering analysis, we elucidated the full mechanism that describes how the number of stacked domains ( $n$ ) and the out-of-plane domain spacing ( $L_z$ ) changed as a function of film thickness and  $p/p_{\text{sat}}$  (Figure 1). The key factor in this mechanism was the amount of solvent in the PS block, a commonly ignored parameter that caused a transition between

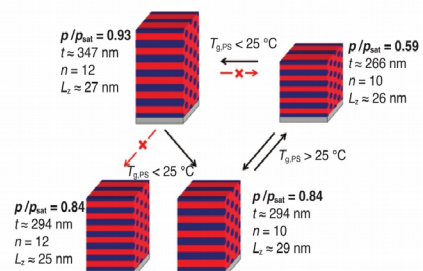


**FIGURE 1:** Schematic detailing the process by which SIS nanostructures restructured during SVA. SVA promoted layering of parallel PS cylinders by swelling the film to impart chain mobility via reduction of the  $T_g$  of the glassy PS domains below the annealing temperature (25 °C). To account for the film thickness ( $t$ ) reduction during solvent removal from  $p/p_{\text{sat}} = 0.93$  to  $p/p_{\text{sat}} = 0.84$ ,  $n$  decreased, rather than  $L_z$ , to prevent unfavorable compression of the SIS polymer chains. However, commensurability conditions from mismatches in  $t$  and  $n$  and an increased polymer-polymer interaction parameter ( $\chi_{\text{PS-PI}}$ ) led to slightly stretched layers ( $L_z = 27$  to  $L_z = 29$ ). When there was not enough solvent in the film to lower the PS  $T_g$  below 25 °C ( $p/p_{\text{sat}} \leq 0.59$ ),  $n$  could no longer adjust to account for thickness changes; instead, the average  $L_z$  decreased with the value of  $p/p_{\text{sat}}$  to account for the change in  $t$ .

a glassy PS state (kinetically trapped layers) and a non-glassy PS state (mobile layers); the PI domain is always non-glassy at room temperature. Primarily, we found that higher solvent concentrations in the PS domain lowered the  $T_g$  below room temperature, which increased the chain mobility and allowed the domains to rearrange and form the low energy domain spacing (modified slightly by commensurability). As the solvent concentration was decreased,  $T_g$  increased above room temperature,  $n$  was fixed, and  $L_z$  decreased as the film de-swelled. Interestingly, although the minority PS domain (cylinders) was the only glassy component at low solvent concentration, the non-glassy PI matrix was kinetically trapped as well and forced to conform to the same compressed  $L_z$ . This competition between polymer-solvent thermodynamics and kinetics resulted in an unexpected increase in  $L_z$  (27 nm to 29 nm) upon deswelling the film from a  $p/p_{\text{sat}}$  value of 0.93 to a  $p/p_{\text{sat}}$  value of 0.84, as there was sufficient *d*-benzene in the PS

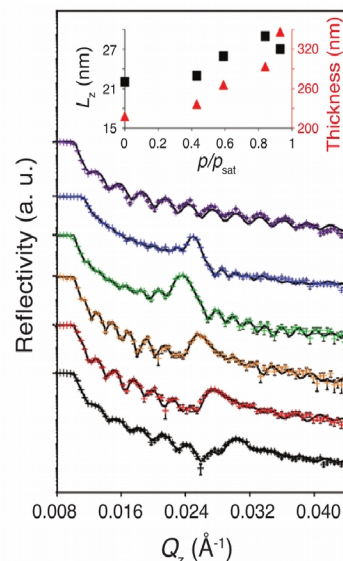


**FIGURE 2:** NR profiles (data points) and model fits (black lines) for *d*-benzene swollen SIS films at different  $p/p_{\text{sat}}$  in the order that they were run from top to bottom. Upon exposure to solvent vapor, the film increased in thickness ( $t$ ) due to solvent swelling and developed repeating parallel cylinder layers as evidenced by the narrowing of Kiessig fringes and the formation of a Bragg peak, respectively. In general,  $L_z$  decreased with the value of  $p/p_{\text{sat}}$ . However,  $L_z$  increased slightly from  $p/p_{\text{sat}} = 0.93$  to  $p/p_{\text{sat}} = 0.84$ . This effect was attributed to the reduction of  $n$  and subsequent incommensurability promoting slightly thicker layers. The inset plot shows how the film thickness and  $L_z$  change as a function of  $p/p_{\text{sat}}$ . The NR profiles have been vertically offset for clarity.

domain (51 % by mole and 40 % by mole, respectively) to lower the  $T_g$  of PS below 25 °C and impart chain mobility [2]. Therefore, the polymer chains were able to decrease  $n$  from 12 to 10 and maintain a favorable  $L_z$  at a reduced film thickness [3]. At the new  $n = 10$ , the layers were stretched slightly from 27 nm to 29 nm to achieve commensurability between the film thickness and  $L_z$  and to account for the slight increase in  $\chi_{\text{PS-PI}}$  when the solvent concentration in the film was reduced.

This unexpected transition from increasing to decreasing  $L_z$  during deswelling was determined from NR results obtained at the multi-angle grazing-incidence *k*-vector (MAGIK) reflectometer (Figure 2). The Bragg peak, which indicated the development of a periodic out-of-plane domain structure (parallel cylinders), shifted to a lower  $Q_z$  value going from the first ( $p/p_{\text{sat}} = 0.93$ ) to second ( $p/p_{\text{sat}} = 0.84$ ) solvent concentration and increased thereafter. This distinct shift signified an initial increase in  $L_z$ . Because the film thickness only decreased during deswelling,  $n$  had to decrease to maintain the low energy domain spacing. However  $L_z$  increased above this value to maintain commensurability with the film thickness,  $t$ . Following the initial increase in  $L_z$  the number of domains was fixed by the immobility of the PS domain, and  $L_z$  was forced to decrease with film thickness as solvent was removed.

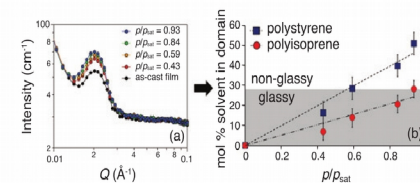


**FIGURE 3:** (a) SANS intensity profiles as a function of  $p/p_{\text{sat}}$ . (b) Solvent content in PS and PI domains calculated from broad peak model fits to SANS intensity profiles indicated that at a  $p/p_{\text{sat}}$  value of 0.59 the normalized *d*-benzene mol % in the PS domain (moles *d*-benzene in PS divided by moles *d*-benzene plus PS) was not high enough to reduce the  $T_g$  below 25 °C, which resulted in a glassy PS domain (gray shaded region) with limited mobility; the PI is always non-glassy at 25 °C.

To understand the cause of the structural transition, azimuthally averaged 1-D intensity profiles from *in situ* SANS, taken at the NGB 10 m SANS, (Figure 3a) were analyzed to quantify the solvent uptake in each domain as a function of  $p/p_{\text{sat}}$  (Figure 3b). Figure 3b revealed that at a  $p/p_{\text{sat}}$  value of 0.59, there was not a sufficient concentration of solvent to reduce the PS  $T_g$  below 25 °C (25–30) % by mole [2], and the PS domain transitioned to a glassy state. The  $p/p_{\text{sat}}$  value at which the glassy/non-glassy transition occurred matched with the  $p/p_{\text{sat}}$  value at which the restructuring mechanism, (measured with NR) changed, providing the final piece to the SVA mechanism.

In summary, we related measurable differences in  $L_z$ ,  $n$ , and film thickness to in-plane and out-of-plane solvent profiles determined with SANS and NR, respectively. The ability to add polymer-solvent contrast (via *d*-benzene) allowed us to relate both polymer-polymer and polymer-solvent interactions to the reorganization of nanostructures during SVA. Thus, we determined how solvent preferentially diffuses into individual domains, tracked solvent diffusion and nanostructure reorganization as a function of  $p/p_{\text{sat}}$ , and monitored the kinetic trapping of nanostructure reorganization with solvent removal. Finally, we demonstrated that  $L_z$  can be controlled by manipulating the solvent content in the film and the swelling/drying pathway. These outcomes help define several of the underlying mechanisms that govern self-assembly in BP thin films subjected to SVA, such as the mobility required to restructure the domain lattice, the impact of surface and interfacial roughness on commensurability constraints, the trapping of solvent in the film as a function of polymer mobility, and the selectivity of polymer and solvent at the free and substrate surfaces, which can facilitate the prediction of ideal solvent annealing conditions depending on the objectives.

## References

- [1] C. K. Shelton, R. L. Jones, J. A. Dura, T. H. Epps, III, (2016) in review.
- [2] J. E. Mark, Physical Properties of Polymers Handbook, (Springer Science & Business Media, LLC, New York, 2007) p. 191.
- [3] M. Luo, J. E. Seppala, J. N. L. Albert, R. L. Lewis, N. Mahadevarupam, G. E. Stein, T. H. Epps, III, Macromolecules **46**, 1803 (2013).

<sup>1</sup> Department of Chemical and Biomolecular Engineering, University of Delaware, Newark, DE 19716

<sup>2</sup> Materials Science and Engineering Division, National Institute of Standards and Technology, Gaithersburg, MD 20899

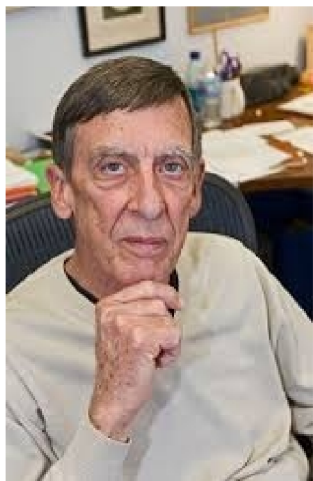
<sup>3</sup> NIST Center for Neutron Research, National Institute of Standards and Technology, Gaithersburg, MD 20899

<sup>4</sup> Department of Materials Science and Engineering, University of Delaware, Newark, DE 19716



# Biology

Biology is another significant area of science where neutron reflectometry and diffraction studies have been applied at the NCNR. Many people have been involved in this endeavor as well, both staff and external colleagues including Steve White, Doug Tobias, Mike Kent, Kent Blasie, Larry Kneller, Klaus Gawrisch, Ursula Perez-Salas, Duncan McGillivray, Jarek Majewski, Stephen Holt, Jeremy Lakey, and Anton Le Brun. Collaborations with Anne Plant, Curt Meuse, John Elliott and others in various divisions at NIST also proved very fruitful.



**Part 3: Application of polarized neutrons and ferromagnetic reference layers to phase-sensitive neutron reflectometry studies of the structure of soft condensed matter systems**

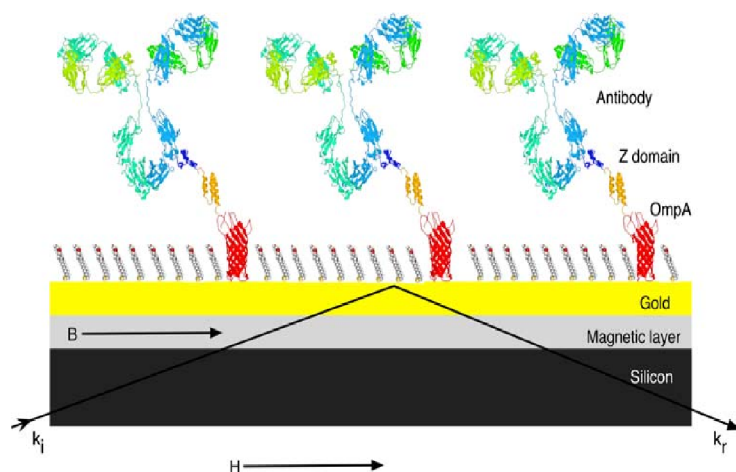


(Figure from the work of Anton Le Brun et al.)



Steve White, Ursula Perez-Salas, Mike Kent, and Kent Blasie, CW from top left.



## Phase Sensitive Neutron Reflectometry on a Water-Cushioned Biomembrane-Mimic

**B**iomimetic membranes have been developed as models of living cell membranes, and this has applications in the quest for biocompatibility of inorganic materials in biologically active mediums, such as coatings for artificial organs. A membrane consists of a lipid bilayer (two lipid layers) where hydrophobic carbon chains form the inside of the membrane and their polar head groups the interface with the aqueous surrounding medium. A supported membrane-mimic consists of a lipid-like bilayer, typically attached to a single-crystal substrate, with access to water only at the top surface [1, 2]. Here we use neutron reflectometry to study a system in which water has access to both sides of a membrane-mimic attached to such a substrate, thus making the system a closer mimic to a real cell membrane.

The system devised by Liu *et al.* [3] consists of a water-swallowable polyelectrolyte that electrostatically binds to the substrate and acts as a “cushion” for the membrane, not unlike the cytoskeletal support found in actual mammalian cell membranes. The lower half of the membrane-mimic is a terpolymer that attaches to the polyelectrolyte. A phospholipid layer forms on top of the terpolymer and the bilayer is finally chemically crosslinked for added stability. The system is shown schematically in Fig. 1.

Neutron reflectivity measurements were performed at the NG-1 vertical stage reflectometer to obtain the compositional profile at every step of the assembling process of the membrane-mimic which consisted of three stages: a) polyelectrolyte multilayer (PE), b) polyelectrolyte multilayer

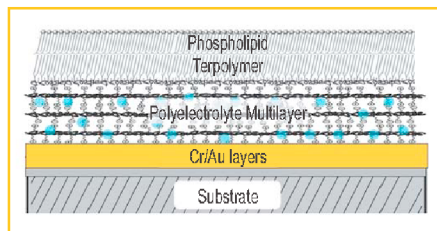


Fig. 1. Schematic diagram of a biomimetic membrane. The phospholipid layer at the top combines with the terpolymer layer to form a membrane-mimic that in turn resides on the water (blue dots) permeable “cushion” polyelectrolyte multilayer. The latter attaches electrostatically to the Au-capped substrate.

plus terpolymer (PE+TER), and c) polyelectrolyte multilayer plus terpolymer plus phospholipid layer (PE+TER+PC) [4]. The spatial resolution attained was approximately 10 Å, about half the thickness of a membrane bilayer, making it possible to distinguish the two layers of a membrane but not the structure of a single layer.

A unique compositional profile of the biomimetic film with no a priori knowledge of the sample's composition is obtained by measuring the reflectivity of equivalent samples made onto two substrates [5]. The substrates used were single crystal silicon (Si) and sapphire ( $\text{Al}_2\text{O}_3$ ) coated with chromium (Cr) and then a gold (Au) layer to allow the polyelectrolytes to bind to a similar surface on both wafers.

Figure 2 shows the compositional profiles for the PE, PE+TER and PE+TER+PC assemblies in a  $\text{D}_2\text{O}$  atmosphere at 92 % relative humidity. The figure shows that the hydration of the PE layer is almost unaffected by the addition of the terpolymer and the phospholipid layer. Also, upon the addition of the phospholipid layer to the PE+TER assembly, the composite PE+TER+PC assembly shows an increase in thickness of approximately 30 Å, consistent with the formation of a single phospholipid layer at the surface. It is also clear that the addition of a phospholipid layer onto the terpolymer layer rearranges this region

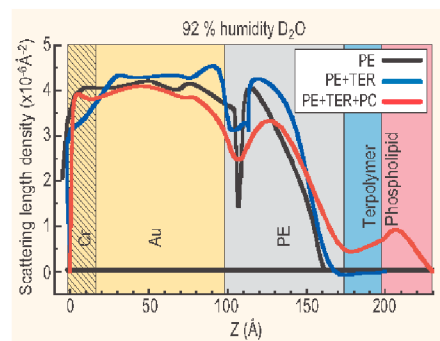


Fig. 2. Compositional profile of biomimetic membrane in a  $\text{D}_2\text{O}$  atmosphere at 92 % relative humidity at various stages of assembly on Au-capped substrate: only polyelectrolyte (PE), polyelectrolyte and terpolymer (PE+TER), polyelectrolyte, terpolymer and phospholipid (PE+TER+PC). The compositional profile is given by the scattering length density, SLD, profile when using neutrons.

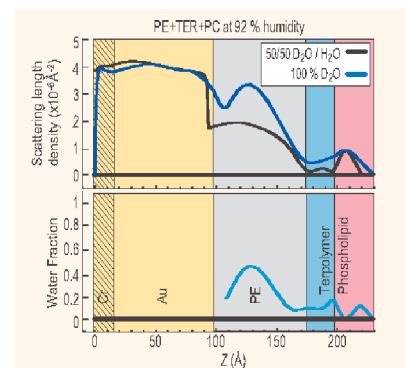


Fig. 3. Scattering length density profiles (top) and water fraction (bottom) for PE+TER+PC under indicated conditions.

significantly, since the terpolymer layer only becomes apparent after the phospholipid layer is added. It is possible to verify with an independent technique (contact angle) that the terpolymer was in fact deposited because it forms a hydrophobic outer layer. The outer surface becomes hydrophilic once the phospholipid layer is deposited onto the terpolymer layer.

Figure 3 (top) shows the profile for the PE+TER+PC assembly under 92 % relative humidity in 100 %  $\text{D}_2\text{O}$  and in 50/50  $\text{D}_2\text{O}/\text{H}_2\text{O}$ . The overall thickness change due to the intake of water, in going from dry (not shown) to 92 % relative humidity, was found to be 20 Å. Figure 3 (bottom) shows the water fraction in the assembly under 92 % relative humidity. This is obtained by assuming that the distribution of each component in the layers is unaffected by having either  $\text{D}_2\text{O}$  or 50/50  $\text{D}_2\text{O}/\text{H}_2\text{O}$ . From the figure it can be seen that the polyelectrolyte multilayer has a 40 % water uptake. This is a significant amount of water, which suggests that the polyelectrolyte multilayer can work as a “cushion” for membrane-mimetic systems. The terpolymer and the phospholipid layers contain an average of 10 % water, which is also significant, suggesting that these layers are not tightly packed.

The method of making equivalent samples on two substrates to obtain a unique compositional profile has a built-in congruency test, particularly useful in checking the reproducibility of the samples as well as the quality of the films. The test is to compare the calculated imaginary part of the complex reflectivity from the obtained profile with the corresponding data, as is shown in Fig. 4 for the PE+TER and PE+TER+PC assemblies. From Fig. 4 it is concluded that the PE+TER samples are homogenous and essentially identical while for the PE+TER+PC assembly, the

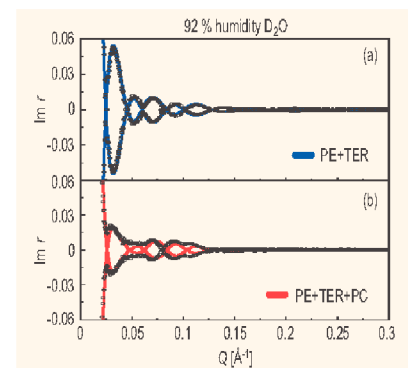


Fig. 4. Imaginary part of the complex reflectivity,  $\text{Im } r(Q)$ , data (symbols) and calculated curves (lines) obtained from the SLD profiles for the PE+TER and the PE+TER+PC assemblies shown in Fig. 2.

absence of true zeros, as indicated by the calculated curve, is suggestive of a small degree of sample inhomogeneity.

The system from Liu *et al.* has many characteristics desirable in a biomimetic membrane. It is a single membrane-mimic attached to a significantly hydrated soft “cushion” support that allows some membrane proteins to function. Thrombomodulin, a membrane protein relevant to blood-clotting, is being studied in this membrane-mimic environment to further develop biocompatible coatings for artificial organs [6].

## References

- [1] E. Sackmann, *Science* **271**, 43 (1996).
- [2] A. L. Plant, *Langmuir* **15**, 5128 (1999).
- [3] H. Liu, K. M. Faucher, X. L. Sun, J. Feng, T. L. Johnson, J. M. Orban, R. P. Apkarian, R. A. Dluhy, E. L. Chaikof, *Langmuir* **18**, 1332 (2002).
- [4] U. A. Perez-Salas, K. M. Faucher, C. F. Majkrzak, N. F. Berk, S. Krueger, E. L. Chaikof, *Langmuir* **19**, 7688 (2003).
- [5] C. F. Majkrzak, N. F. Berk, U. A. Perez-Salas *Langmuir* **19**, 1506 (2003).
- [6] J. Feng, P. Y. Tseng, K. M. Faucher, J. M. Orban, X. L. Sun, E. L. Chaikof, *Langmuir* **18**, 9907 (2002).

U. A. Perez-Salas  
NIST Center for Neutron Research  
National Institute of Standards and Technology, Gaithersburg, MD 20899-6562

K. M. Faucher  
Emory University School of Medicine, Atlanta, GA 30322

C. F. Majkrzak, N. F. Berk, S. Krueger  
NIST Center for Neutron Research  
National Institute of Standards and Technology  
Gaithersburg, MD 20899-6562

E. L. Chaikof  
Emory University School of Medicine  
Atlanta, GA 30322

The next series of slides shows a NR study of the location of water within a particular biomimetic membrane of interest to a vascular surgeon (who is attempting to develop synthetic replacements for arteries and veins in medical applications). Such synthetic vessels must have bio-compatible coatings which won't foster an immune system response.

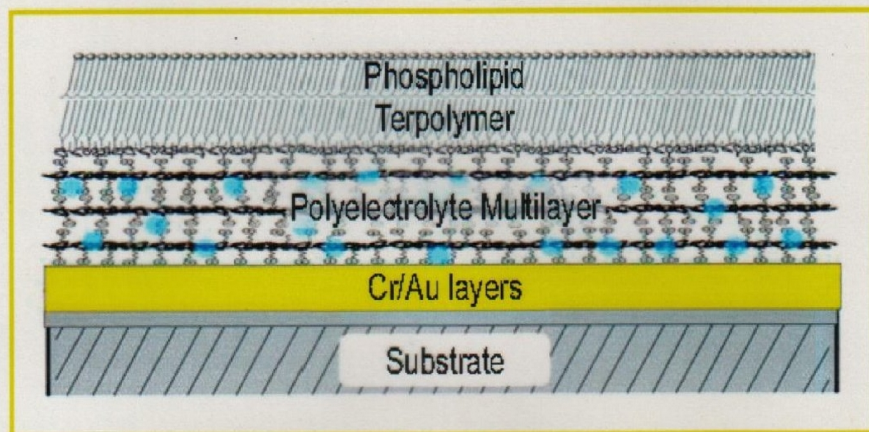


Fig. 1. Schematic diagram of a biomimetic membrane. The phospholipid layer at the top combines with the terpolymer layer to form a membrane-mimic that in turn resides on the water (blue dots) permeable "cushion" polyelectrolyte multilayer. The latter attaches electrostatically to the Au-capped substrate.

(Work of Ursula Perez-Salas, K. Faucher, E. Chaikof, et al.)

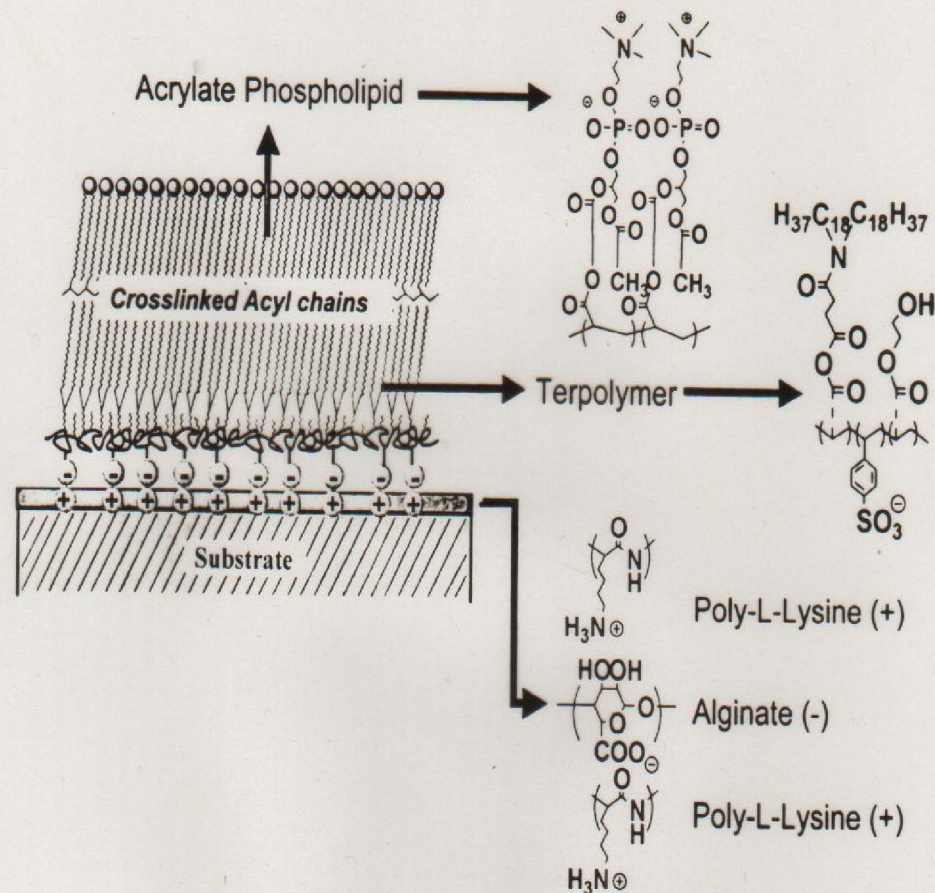
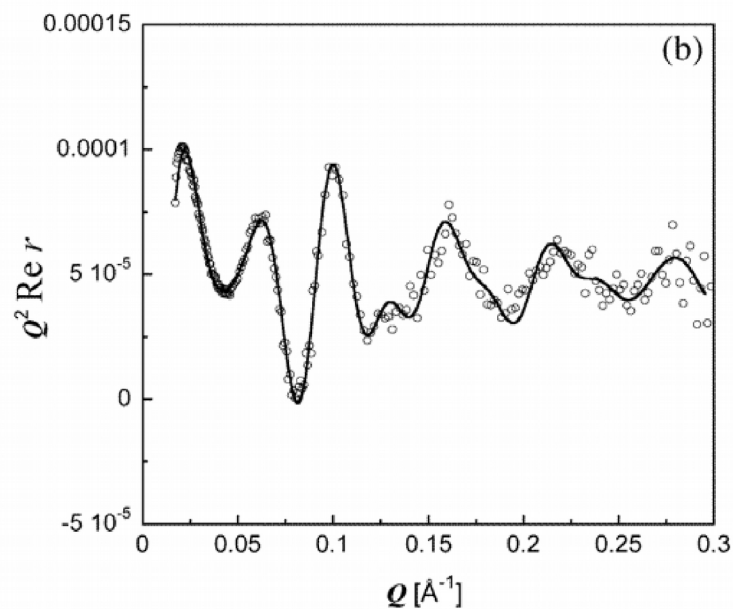
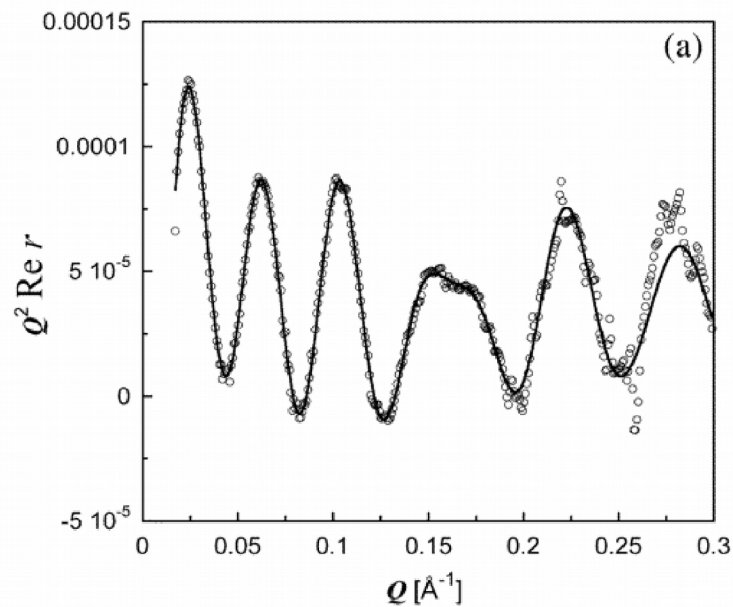


Figure 1:

- 1 Schematic representation the terpolymer (TER)-acrylate phospholipid (PC) membrane mimic supported on a polyelectrolyte multilayer(PE) "cushion". . . . .





Typical real parts of reflection amplitudes obtained via phase-sensitive neutron reflectometry methods for the biomimetic film structure presented in the previous slides.

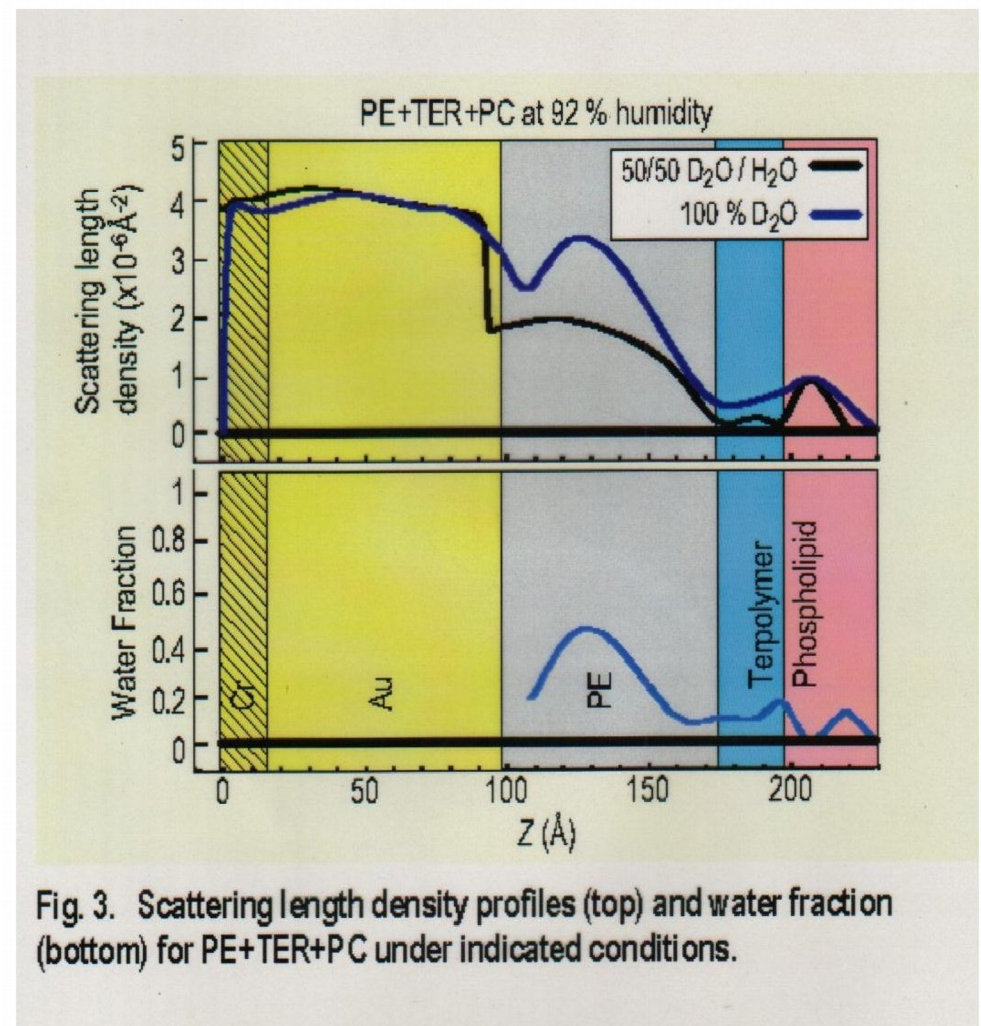
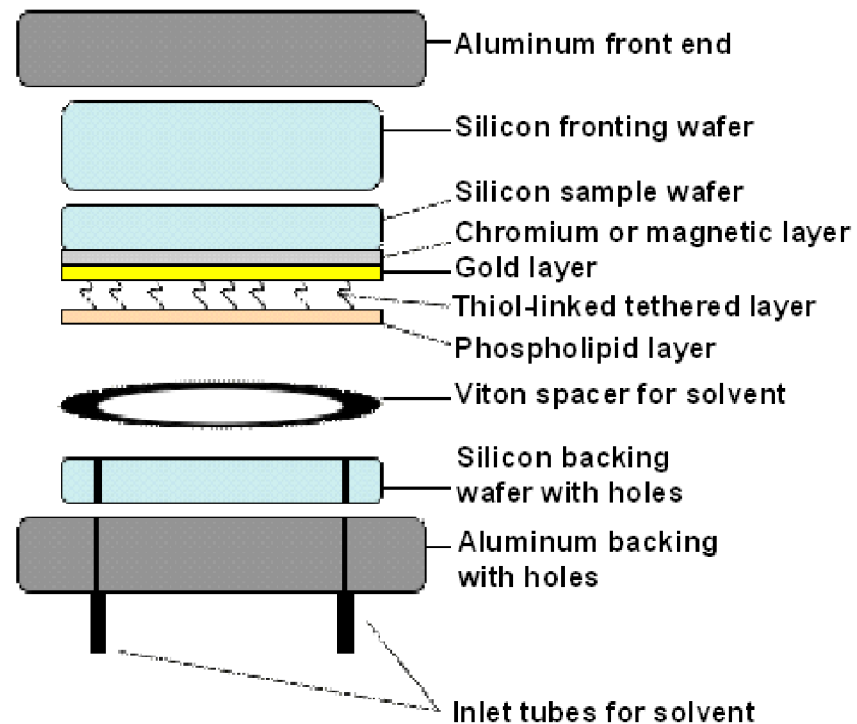
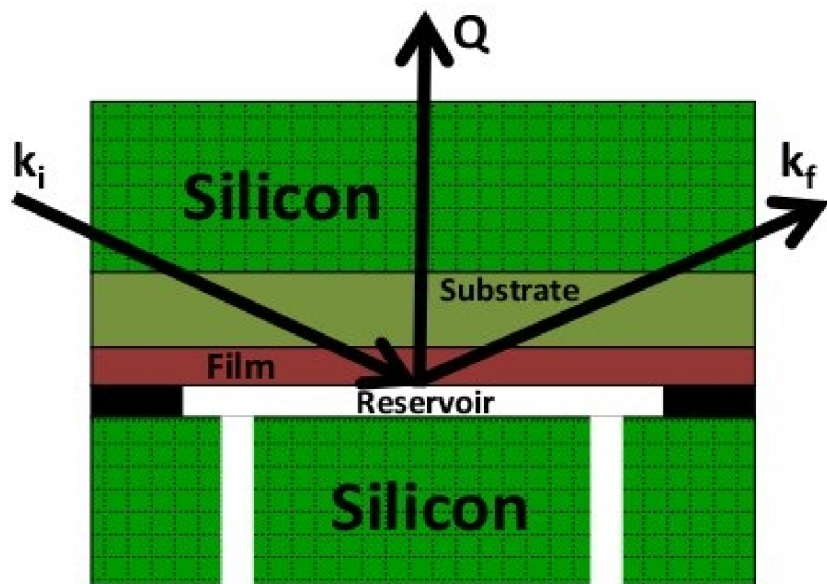
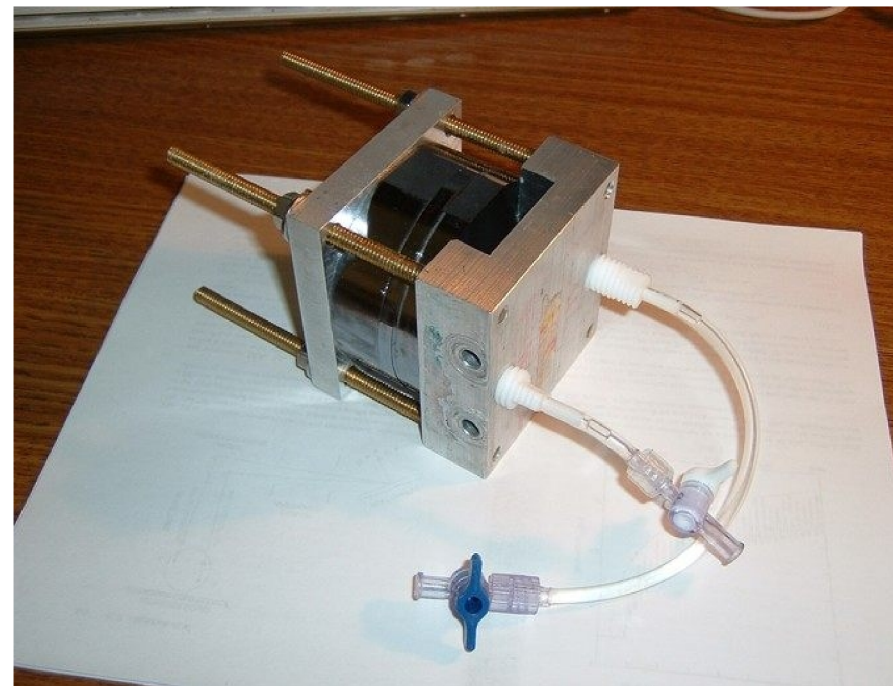


Fig. 3. Scattering length density profiles (top) and water fraction (bottom) for PE+TER+PC under indicated conditions.

After a number of different reflectivity measurements with various aqueous reservoir contrast values for  $\text{H}_2\text{O} / \text{D}_2\text{O}$  ratios, it was possible to deduce, from the analysis of that data, the water distribution across the thickness of the film structure. As shown in the figure above, the water is found to reside primarily within the poly-electrolyte layer.



Proper design of a fluids cell is essential for optimizing the signal-to-noise ratio in neutron reflectivity measurements.





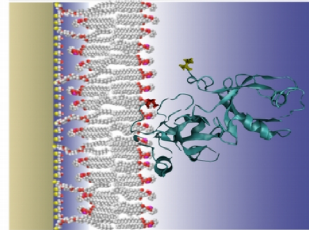
A sampling (on this and the next slide) of more recent specular NR studies of compositional depth profiles of biological macromolecules attached to or embedded in lipid bilayer membranes. These results are remarkable -- if not spectacular (at least in my opinion)!

## Water-soluble membrane-associated proteins

>50% of biological NR beam time for biomedical applications using tBLMs

### Active projects (last 2 cycles):

- Dengue
- Gaucher's disease
- GRASP
- HIV Gag & antibodies
- RSV & MLV
- Neurotransmitter
- OmpA/LA
- Parkinson's disease
- PTEN Tumor suppressor
- T-Cell receptor



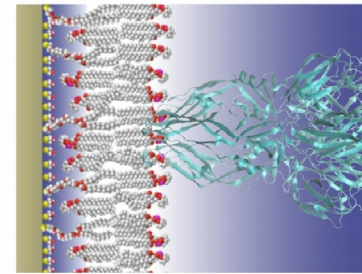
GRASP orientation at a tethered bilayer lipid membrane (tBLM) as determined by NR

### Collaborative staff involvement:

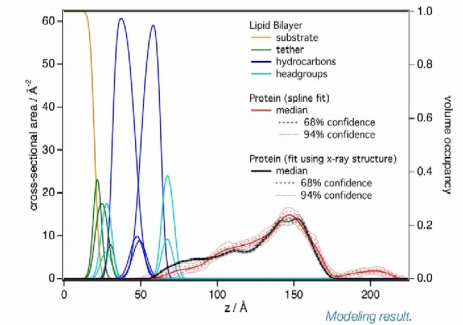
- experimental planning
- substrate preparation
- tether synthesis
- neutron measurement
- data analysis

Bulent Akgun, Frank Heinrich, Mathias Lösche, Duncan McGillivray, Hirsh Nanda, David Vanderah

## Example: Dengue Virus Envelope Protein



Visualization. Project with Mike Kent, Sandia National Labs.



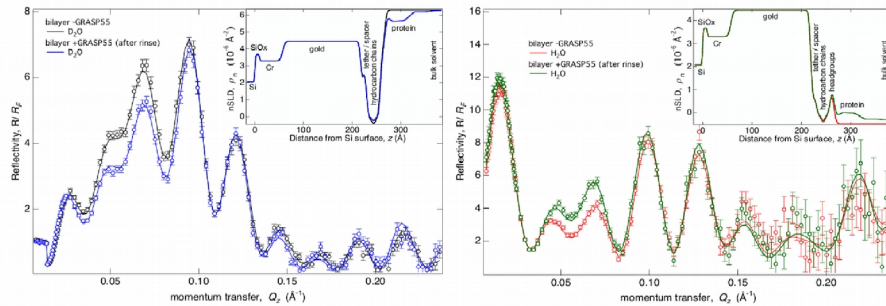
- Monte-Carlo Markov Chain uncertainty analysis
- Composition-space modeling of the bilayer
- Free-form fitting of structurally unknown components of the architecture
- Usage of PDB structure files for position and orientation of rigid proteins

Bulent Akgun, Frank Heinrich, Paul Kienzle, Sushil Satija



[www.nsl.nist.gov/programs/reflect/](http://www.nsl.nist.gov/programs/reflect/)

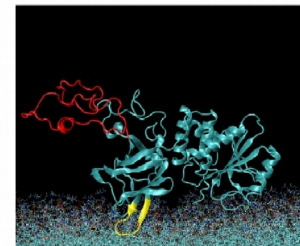
## Typical reflectometry data for tBLM experiments



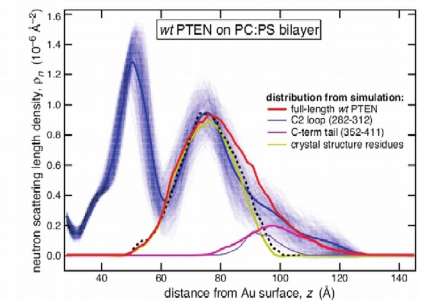
NR data measured on NG7, and best-fits for GRASP association with lipid membranes, project with A. Linstedt, University of Pittsburgh

Bulent Akgun, Frank Heinrich, Mathias Lösche, Duncan McGillivray, Hirsh Nanda

## Combining NR with Molecular Simulations



MD simulation snapshot of PTEN tumor suppressor association with a PS-containing lipid membrane



Comparison of MD and NR results, Shenoy, S. et al. J. Struct. Biol. 1-15 (2012).

Comparison of experimental data with results from:

- MD simulation
- Monte Carlo conformational search (SASSIE) results

Future Challenges:

- Ensemble averaging, integrating NR and simulation

Joseph Curtis, Mathias Lösche, Hirsh Nanda



# Neutron reflectometry studies of membrane-bound tubulin reveal an amphipathic helical binding motif

D. P. Hoogerheide,<sup>1</sup> S. Yu. Noskov,<sup>2</sup> D. Jacobs,<sup>3</sup> L. Bergdoll,<sup>4</sup> V. Silin,<sup>5</sup> D. Worcester,<sup>1</sup> J. Abramson,<sup>4,6</sup> H. Nanda,<sup>1,7</sup> T. K. Rostovtseva,<sup>3</sup> and S. M. Bezrukov<sup>3</sup>

Layer lipid membranes (BLMs) form barriers that separate the interior from the exterior of the cell and divide the cell into specialized compartments called organelles. Proteins that are embedded into BLMs, known as membrane proteins, play diverse roles, including the transportation of various ions, metabolites, proteins, DNA, etc., across the BLMs, thus providing communication pathways between cells and between organelles inside cells. This function is so crucial for health and disease that while membrane proteins account for about 20 % of known proteins [1], they comprise 70 % of known drug targets [2]. In humans, mitochondria are the organelles responsible for energy conversion, with two main purposes: to store energy, and to produce heat that maintains body temperature. However, mitochondria themselves are also the sources of the reactive oxygen species that damage mitochondria, mitochondrial DNA, and other cellular components. Therefore, maintaining the appropriate conditions that provide sufficient energy for cellular functions and limit the production of chemically damaging reactive oxygen species is crucial for cell life and death. Recent evidence indicates that the regulation of this equilibrium is accomplished at least in part by a complex of the mitochondrial voltage-dependent anion channel (VDAC), a passive transport channel of the mitochondrial outer membrane (MOM), and dimeric tubulin [3], which is best known as a structural protein in microtubules. The association of tubulin with the MOM is particularly suggestive given the role of microtubule-targeting drugs (MTDs) in chemotherapy [4]. In this work we shed light on the role of dimeric tubulin in regulating mitochondrial bioenergetics by investigating the binding of tubulin to biomimetic mitochondrial membranes using a combination of neutron reflectometry (NR) and molecular dynamics (MD) simulations [5].

Tubulin is a heterodimer comprising  $\alpha$  and  $\beta$  subunits, which have similar spatial arrangements but different amino acid sequences. In microtubules, the exposed end is always the  $\beta$  subunit; as a result, all MTDs bind to the  $\beta$  subunit [4]. Remarkably, in an *in vitro* system the rate of interaction between tubulin and a single VDAC channel was observed to depend strongly on the lipid composition of the BLM in which VDAC was embedded. In particular, the interaction rate increased by two orders of magnitude if a lamellar (i.e. preferring a flat membrane geometry) dioleoylphosphatidylcholine

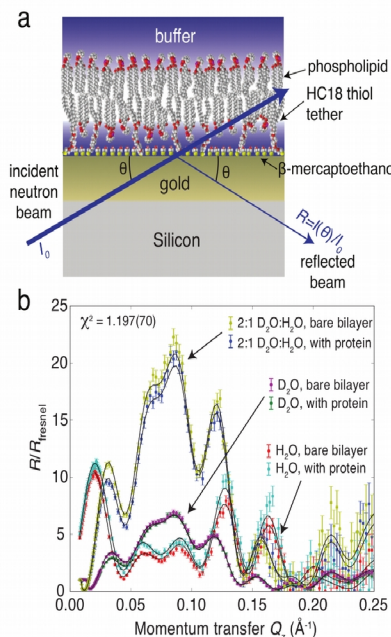


**FIGURE 1:** Neutron reflectometry (NR) experiment with a sparsely tethered lipid bilayer membrane (stBLM). (a) Schematic of the stBLM and scattering geometry. Sparse tethering is achieved by using  $\beta$ -mercaptoethanol as a spacer molecule. (b) NR data, showing the differences between the three deuteration levels of the buffer solutions. Data are normalized to the Fresnel reflectivity expected from a silicon/buffer interface. Solid lines show the fit to a theoretical model of the bilayer with bound tubulin.

(DOPC) membrane was replaced with the non-lamellar (preferring a curved membrane geometry) dioleoylphosphatidylethanolamine (DOPE) [6], suggesting that tubulin is able to distinguish between these two lipid species. Furthermore, these results indicate that the first step of the VDAC-tubulin interaction involves tubulin binding to the lipid membrane surface.

In this study, we determined the orientation of membrane-bound tubulin—and hence the face of the tubulin molecule that is in contact with the membrane surface—by NR on sparsely tethered BLMs (stBLMs). NR reports on the depth profile of the interfacial components, including the stBLM and any membrane-bound tubulin (Figure 1a). Thus, NR is well suited to determine the spatial extent of the protein in and away from the BLM and yields a potential family of binding surfaces to be investigated by computational methods and amino acid sequence analysis.

For these experiments, an stBLM was composed of a 1:1 molar ratio of DOPC:DOPE. This lipid composition closely mimics the mitochondrial outer membrane, in which the ratio of PC to PE headgroups is about 3:2. The stBLM was bathed in an aqueous 1 mol/L KCl solution buffered at pH 7.4 by 5 mM HEPES. The reflectivity of the stBLM was measured using 4.75 Å neutrons on the NCNR NG7 horizontal reflectometer. To provide contrast between the various components of the stBLM system, a sequence of reflectometry measurements was performed using buffers in 100 %  $D_2O$ , 100 %  $H_2O$ , and a 2:1  $D_2O:H_2O$  mixture. This procedure was then repeated in the presence of 600 nM tubulin dimers (a physiologically relevant concentration).

The reflectivity data (Figure 1b) were then fit to an stBLM model (Figure 2a). Because it accounts for known molecular volumes, molecular connectivity, and stoichiometric constraints, the model is highly constrained. To determine the orientation of the tubulin dimer on the lipid substrate, the expected scattering profile was calculated for various Euler rotations of the known X-ray crystal structure of tubulin. Due to the elongated geometry of the tubulin dimer, the NR profile is very sensitive to the tilt angle  $\beta$  (Figure 2b), allowing a precise determination of this tilt angle,  $\approx 60^\circ$ , from the optimization of the experimental NR data to the stBLM/tubulin model.

To complement the NR results, molecular dynamics simulations were performed to confirm the orientation of  $\alpha$ -tubulin on a DOPE membrane. A range of possible orientations were evaluated using a coarse-grained model of the protein; likely orientations were then optimized using atomistic simulations. The tilt angle of the tubulin on the membrane surface is consistent with that observed by NR, while the atomistic nature of the simulations allows us to identify the particular domain of the tubulin protein that is responsible for binding to the membrane surface. A comparison of the MD and NR results is shown in Figure 2b.

The binding sequence is shown in green in Figure 2b. Notably, it is on the  $\alpha$ -tubulin subunit, rather than on the  $\beta$ -tubulin subunit which is conventionally targeted by chemotherapeutics. When associated with the membrane, this amino acid sequence likely adopts an  $\alpha$ -helical structure which has opposing hydrophobic and hydrophilic faces, i.e. an amphipathic helix. Such helices are oriented at the interface between the polar lipid headgroups and the hydrophobic lipid tails. We have also shown [5] that the affinity of this helix to the mixed PC/PE membranes considered here depends strongly on the amount of PE lipid. This suggests that the lipid composition of the mitochondrial outer membrane could regulate tubulin binding, which in turn modulates VDAC permeability and consequently mitochondrial function. We hypothesize that this selectivity for the uncharged PE lipids may have developed to overcome electrostatic

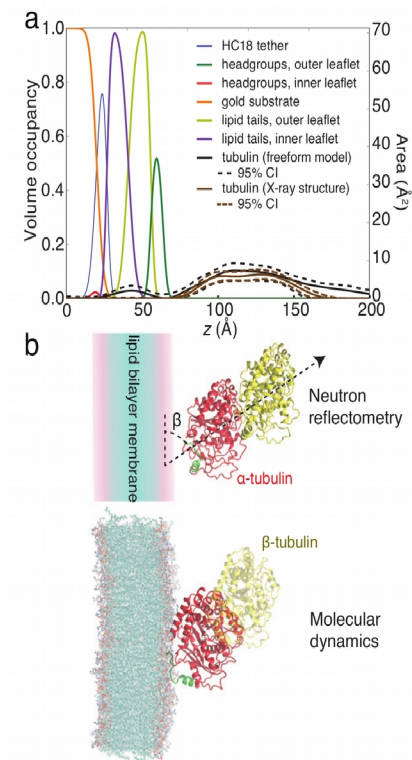


**FIGURE 2:** Results of modeling the tubulin-stBLM system. (a) Volume occupancy representation showing the position of various chemical species. (b) Visual representation of the structure of membrane-bound tubulin as determined by NR (top) and atomistic molecular dynamics simulations of the  $\alpha$ -tubulin subunit (bottom). The Euler angle  $\beta$  is  $\approx 60^\circ$ . The  $\alpha$ -tubulin subunit is shown in red; the  $\beta$ -tubulin subunit in yellow; and the binding site in green.

repulsion between the negatively charged components of the mitochondrial outer membrane and the tubulin molecule.

## References

1. M. S. Almen, K. J. Nordstrom, R. Fredriksson, and H. B. Schioth, *BMC Biology* **7**, 50 (2009).
2. M. A. Yildirim, K.-I. Goh, M. E. Cusick, A.-L. Barabasi, and M. Vidal, *Nat. Biotechnol.* **25**, 1119 (2007).
3. T. K. Rostovtseva, K. L. Sheldon, E. Hassanzadeh, C. Monge, V. Saks, S. M. Bezrukov, and D. L. Sackett, *Proc. Natl. Acad. Sci.* **105**, 18746 (2008).
4. J. J. Field, A. B. Waight, and P. D. Senter, *Proc. Natl. Acad. Sci.* **111**, 13684 (2014).
5. D. P. Hoogerheide, S. Yu. Noskov, D. Jacobs, L. Bergdoll, V. Silin, D. Worcester, J. Abramson, H. Nanda, T. K. Rostovtseva, and S. M. Bezrukov, *Nat. Struct. Mol. Biol.*, submitted (2016).
6. T. K. Rostovtseva, P. A. Gurney, M. Y. Chen, and S. M. Bezrukov, *J. Biol. Chem.* **287**, 29589 (2012).

<sup>1</sup> NIST Center for Neutron Research, National Institute of Standards and Technology, Gaithersburg, MD 20899

<sup>2</sup> University of Calgary, Calgary, AB, Canada, T2N 1N4

<sup>3</sup> Eunice Kennedy Shriver National Institute of Child Health and Human Development, National Institutes of Health, Bethesda, MD 20892

<sup>4</sup> University of California Los Angeles, Los Angeles, CA 90095

<sup>5</sup> University of Maryland, Rockville, MD 20850

<sup>6</sup> Institute for Stem Cell Biology and Regenerative Medicine, National Centre for Biological Sciences–Tata Institute of Fundamental Research, Bellary Road, Bangalore-560065, Karnataka, India

<sup>7</sup> Carnegie Mellon University, Pittsburgh, PA 15213



# How Do Lipid Membranes Accommodate Voltage-sensing Domains of Ion Channels?

M. Mihailescu<sup>1</sup>, D. Krepiak<sup>2</sup>, J.A. Freites<sup>1,4</sup>, E. Schow<sup>4</sup>, D.L. Worcester<sup>5,1,3</sup>, K. Gawrisch<sup>6</sup>, D. Tobias<sup>4</sup>, S.H. White<sup>1</sup> and K.J. Swartz<sup>2</sup>

Electrical signals in the nervous system propagate between neurons along axons via electric potentials that are generated by proteins that reside within the cell membranes. Known as voltage-gated ion channels, these proteins allow ions to pass through the cell membrane in a controlled manner. In the voltage-gated potassium, sodium, and calcium channels found in neurons and muscle cells, a special part of the protein, called the voltage-sensing domain (VSD), moves inside the membrane in response to changes in the membrane potential and drives the ion conduction pore open or closed (gating) [1] (Fig. 1). Until a few years ago, it was thought that VSDs were unique to voltage-gated ion channels. This view has changed radically with the discovery of new families of proteins that use VSD constructs for purposes other than ion channel gating [2]. There is tremendous interest in the structure and function of such proteins. Researchers want to elucidate the mechanism of ion gating in ion channels. Moreover, the portability of VSDs across the genomes of different organisms can provide important clues about evolutionary pathways.

Crystallographic studies using x-ray diffraction on voltage-gated potassium channels have revealed the atomic structure of the VSD in crystallized channels and identified regions that move in response to changes in the membrane electric field [3,4]. However, none of those studies were able to demonstrate the structure and conformation of the voltage-sensor domain in its native lipid environment. A picture of the topology of the VSD in a lipid membrane was needed in order to understand the role of the lipid in the protein stability and function, and ultimately, in the voltage-gating mechanism. We have developed an approach that employs neutron diffraction to obtain the image of functional voltage sensor domains in lipid membranes.

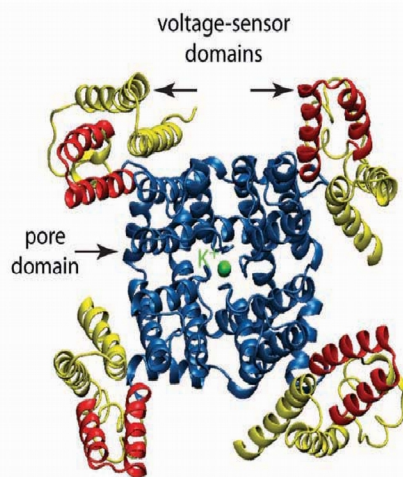


FIGURE 1: Top view (from above the surface of a lipid membrane) of a voltage-gated potassium channel.

We focused our efforts on the voltage-sensing domain of KvAP, an archaebacterial channel from *Aeropyrum pernix* [5], because this domain can be robustly expressed, stably purified, and reconstituted into lipid membranes. The voltage-sensing domains were expressed in *E. coli*, purified, and transferred to lipid vesicles (reconstitution of the VSDs into proteoliposomes). Lipid multilayer samples were prepared by deposition of aqueous dispersions of proteoliposomes on cover glass slides. They were allowed to dry and rehydrated from water phase at 93 % relative humidity throughout the diffraction experiments. Samples containing a few thousands lipid bilayers with incorporated VSDs were measured and strong lamellar diffraction patterns were observed (Fig. 2) and used to generate one dimensional, absolute-scale, scattering-length density profiles normal to the plane of the lipid bilayer. We have determined the protein distribution using contrast variation between protonated and deuterated VSDs. The voltage-sensing domain of KvAP was uniformly deuterated to 74 %

and multilayers were formed with either protonated or deuterated protein at the same protein:lipid ratio and lipid composition. Fourier transformation of the diffraction data to obtain scattering length density profiles and subtraction of the individual profiles for the labeled and unlabeled protein reveals the distribution of the protein across the bilayer (Fig. 3a; red).

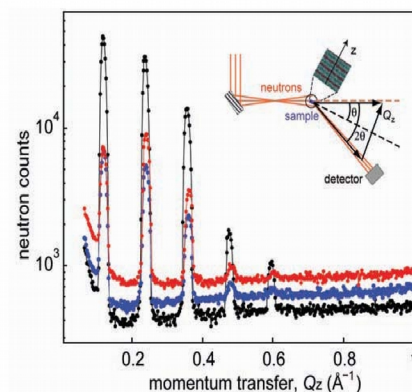


FIGURE 2: Neutron diffraction data collected at the AND/R (NCNR) for lipid multilayers samples with incorporated VSDs: Data displayed are for neat lipid (black), unlabeled VSD in lipid (blue) and deuterated VSD in lipid (red). The inset is a schematic illustration of the experimental setup.

The profile is presented with its uncertainty band derived from the standard deviation of the measured data. Maxima in the density distribution are observed in the headgroup region of the bilayer and minima in the inter-bilayer space. These findings firmly establish that voltage-sensing domains adopt a transmembrane topology, with the four helices oriented roughly normal to the membrane plane. Moreover, the protein distribution (Fig. 3a; red) exhibits extensive overlap with the water distribution (Fig. 3a; blue) within the confines of the lipid membrane, suggesting that the voltage-sensing domains are highly hydrated within the bilayer.

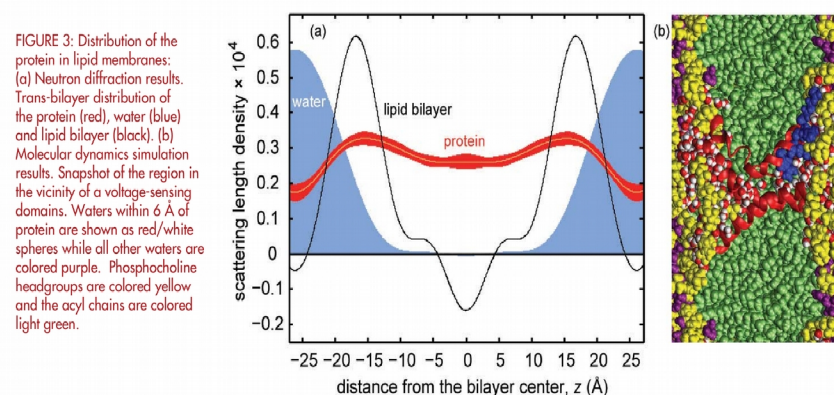


FIGURE 3: Distribution of the protein in lipid membranes: (a) Neutron diffraction results. Trans-bilayer distribution of the protein (red), water (blue) and lipid bilayer (black). (b) Molecular dynamics simulation results. Snapshot of the region in the vicinity of a voltage-sensing domains. Waters within 6 Å of protein are shown as red/white spheres while all other waters are colored purple. Phosphocholine headgroups are colored yellow and the acyl chains are colored light green.

Because neutron diffraction reflects an average distribution of atoms, atomic details in the bilayer structure close to the VSD are not easily revealed in the experiment. To explore details in the protein, lipid and water distribution we employed molecular dynamics simulation for VSDs embedded in lipid bilayers. The simulation results (Fig. 3b) are in qualitative agreement with the experiment regarding the trans-membrane disposition of the four helical segments of the VSD and the overlap with the water distribution. Additionally, the simulations predict that about 4 % all water in the system is intimately associated with the VSDs, and that the lipid layers in contact with the protein are perturbed to a much greater extent than lipids several layers away from the protein (Fig. 3b).

Our results provide direct evidence that voltage sensors domain topology in a membrane environment and will be relevant for other important classes of membrane proteins. They show that the voltage-sensing domains of voltage-gated ion channels interact profoundly with the surrounding membrane and water, in a manner that facilitates their movement and function within the lipid membrane.

## References

- [1] K. J. Swartz, *Nature* **456**, 891 (2008).
- [2] Murata Y. *et al.*, *Nature* **435**, 1239 (2005).
- [3] Y. Jiang, *et al.*, *Nature* **423**, 33 (2003).
- [4] S. B. Long, *et al.*, *Nature* **450**, 376 (2007).
- [5] V. Ruta, *et al.*, *Nature* **422**, 180 (2003).

<sup>1</sup>University of California, Irvine, Irvine, CA 92697

<sup>2</sup>National Institute of Neurological Disorders and Stroke, National Institutes of Health, Bethesda, MD 20892

<sup>3</sup>NIST Center for Neutron Research, National Institute of Standards and Technology, Gaithersburg, MD 20899

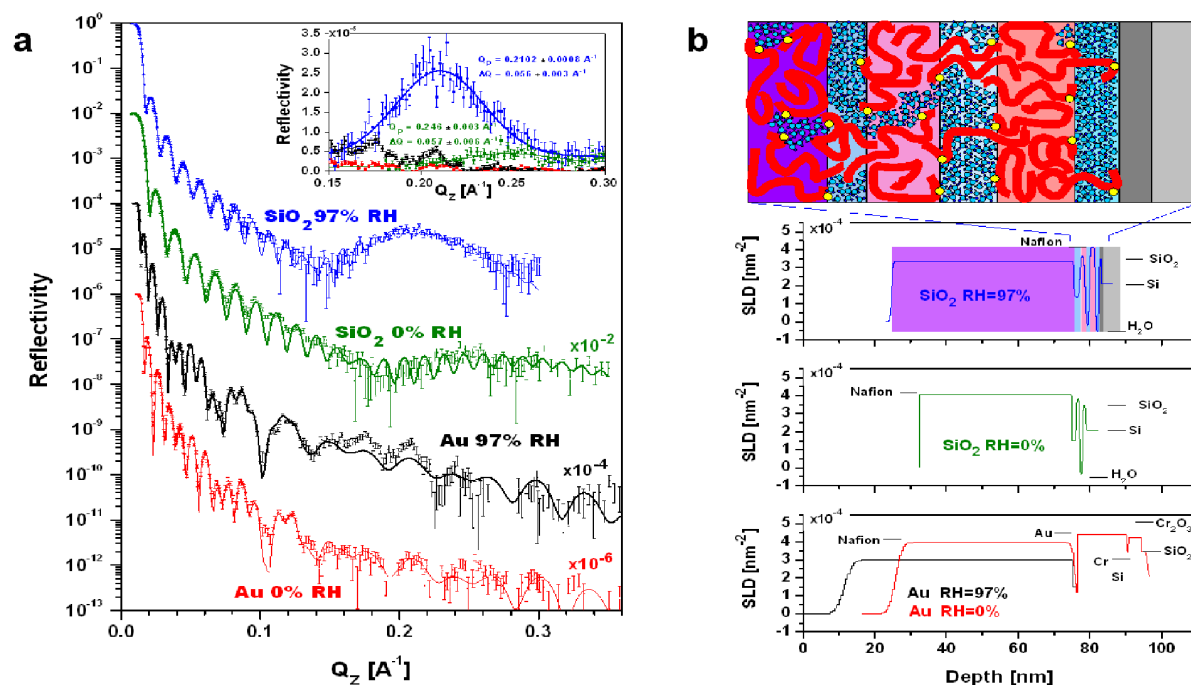
<sup>4</sup>University of California, Irvine, Irvine, CA 92697

<sup>5</sup>University of Missouri, Columbia MO 65211

<sup>6</sup>National Institute of Alcohol Abuse and Alcoholism, National Institutes of Health, Bethesda, MD 20892

# Electrochemistry and Photovoltaics

Although the application of neutron reflectometry to research in this area has not yet become as extensive as in others, it continues to grow steadily. Early work was performed by Dave Wiesler on electrochemical reduction/oxidation reactions while Joe Dura, Steve DeCaluwe and company have focused more recently on fuel cell membranes. Michael Mackay and students from UD have recently investigated the morphology of organic photovoltaic devices at the NCNR, collaborating with staff Brian Kirby, Brian Maranville, and others.



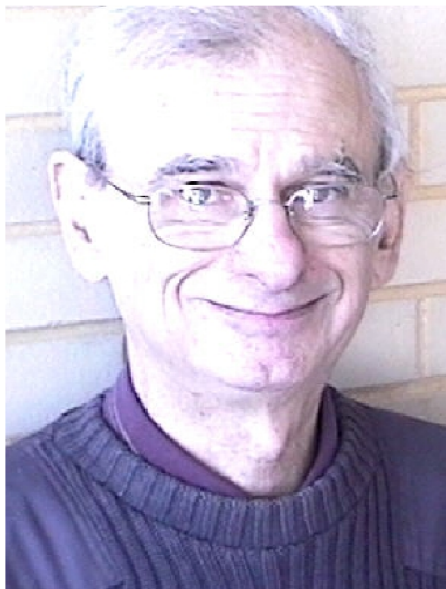
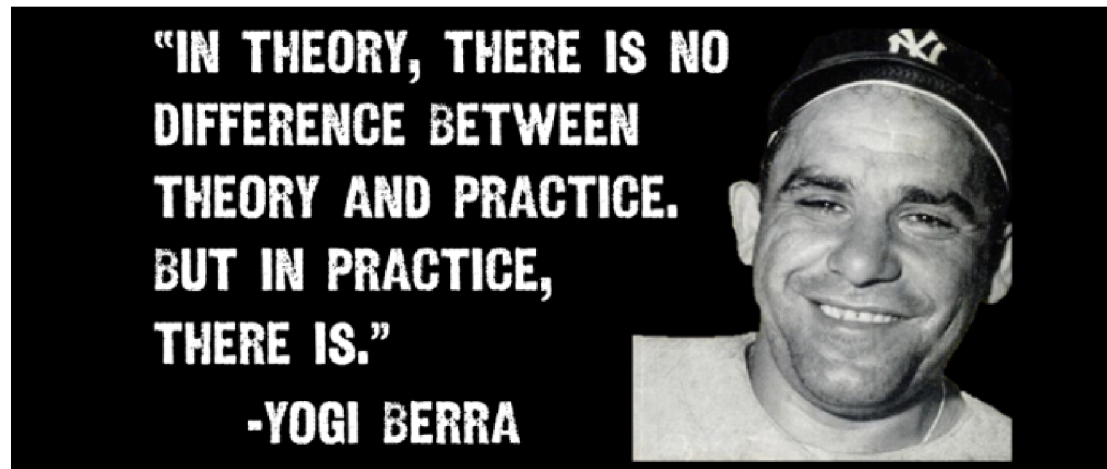
## Multilamellar Interface Structures in Nafion,

Joseph A. Dura, Vivek S. Murthi, Michael Hartman, Sushil K. Satija, Charles F. Majkrzak, *Macromolecules*, **42** (13), pp 4769–4774 (2009) [DOI: 10.1021/ma802823j].



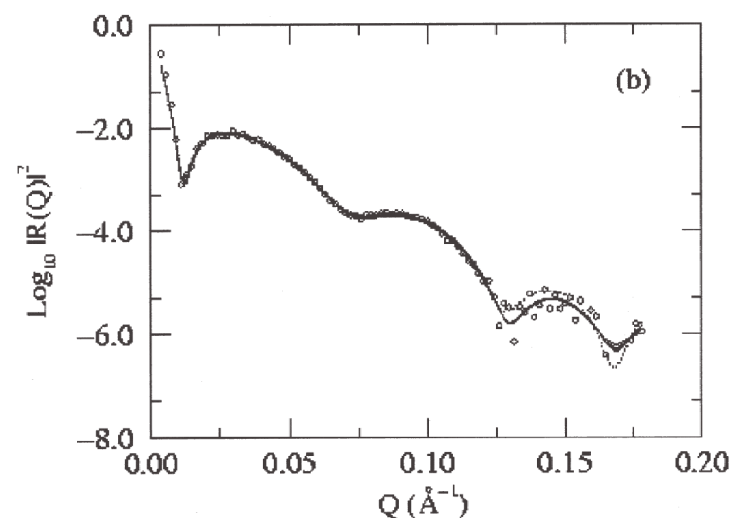
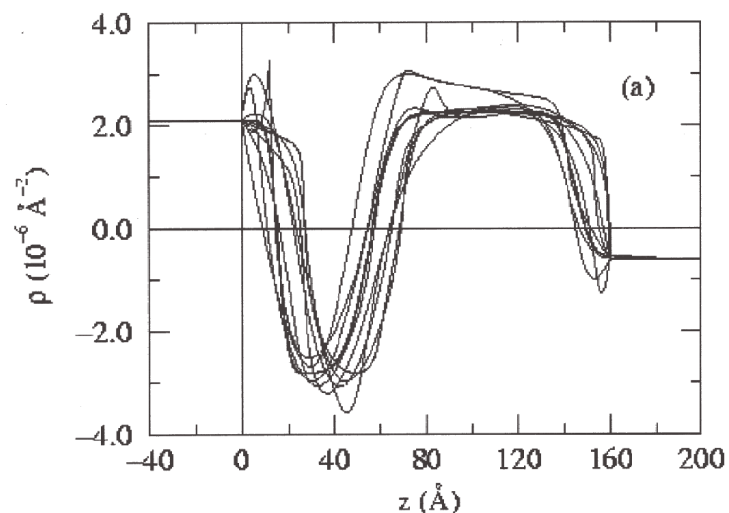


# Development of scattering theory for analysis of neutron reflectivity measurements



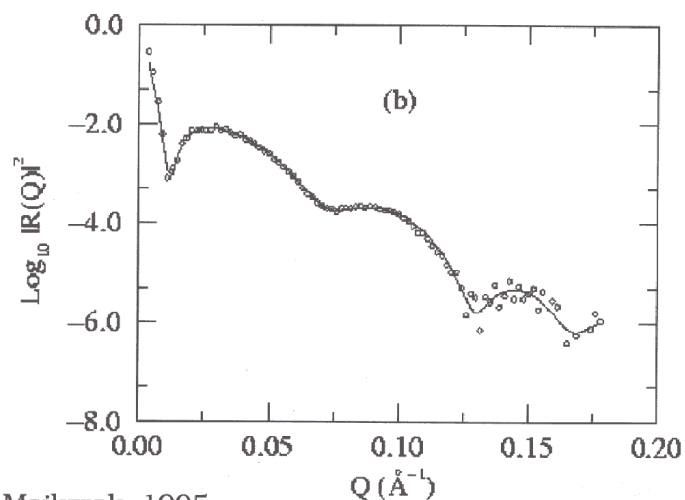
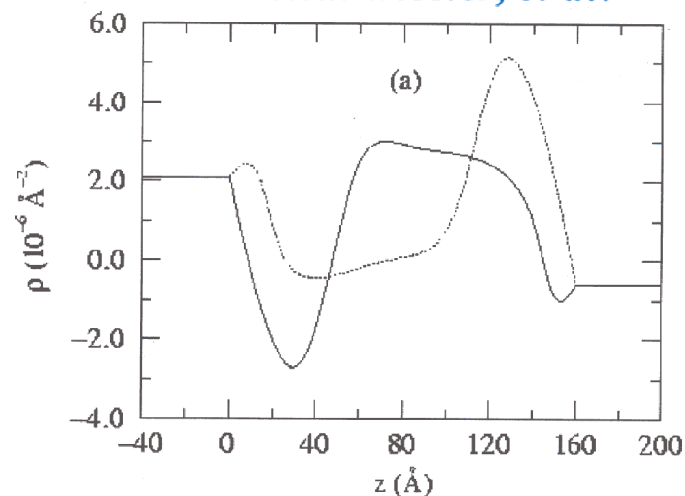
Norman Berk\*

Fortunately, the NCNR has a resident theoretical physicist who is a very well-respected expert in neutron scattering – and who has been “instrumental” in helping formulate our methodologies for interpreting reflectivity measurements. Significant contributions to our reflectometry analysis tools have also been made over the years by John Ankner, Paul Kienzle, and Brian Maranville. In-house experts in computer science, like Przemek Klosowski, have provided consistent support for numerical computations at the NCNR.



Repeated fits of reflectivity data from a Ti/TiO film system on a Si substrate in contact with an aqueous reservoir (Berk et al.). The variation among the individual fits is indicative of the accuracy attainable in the SLD profile given the truncation of the reflectivity data at a maximum value of  $Q$  and the statistical uncertainty in the data points.

### *TiO in situ: Wiesler, et al.*



Berk & Majkrzak, 1995

It was found that if enough individual fits were performed, another “family” of fits emerged (only one of which is shown above in comparison to a representative fit of the other family shown on the previous slide) with essentially the same chi-squared goodness of fit criteria -- this alternative SLD profile is a consequence of the loss of phase information inherent when the reflectivity  $|r|^2$  (proportional to the reflected *intensity*) is measured rather than the complex reflection *amplitude*  $r$  -- i.e., the non uniqueness arises from a loss of the phase information carried by the reflected wave function.



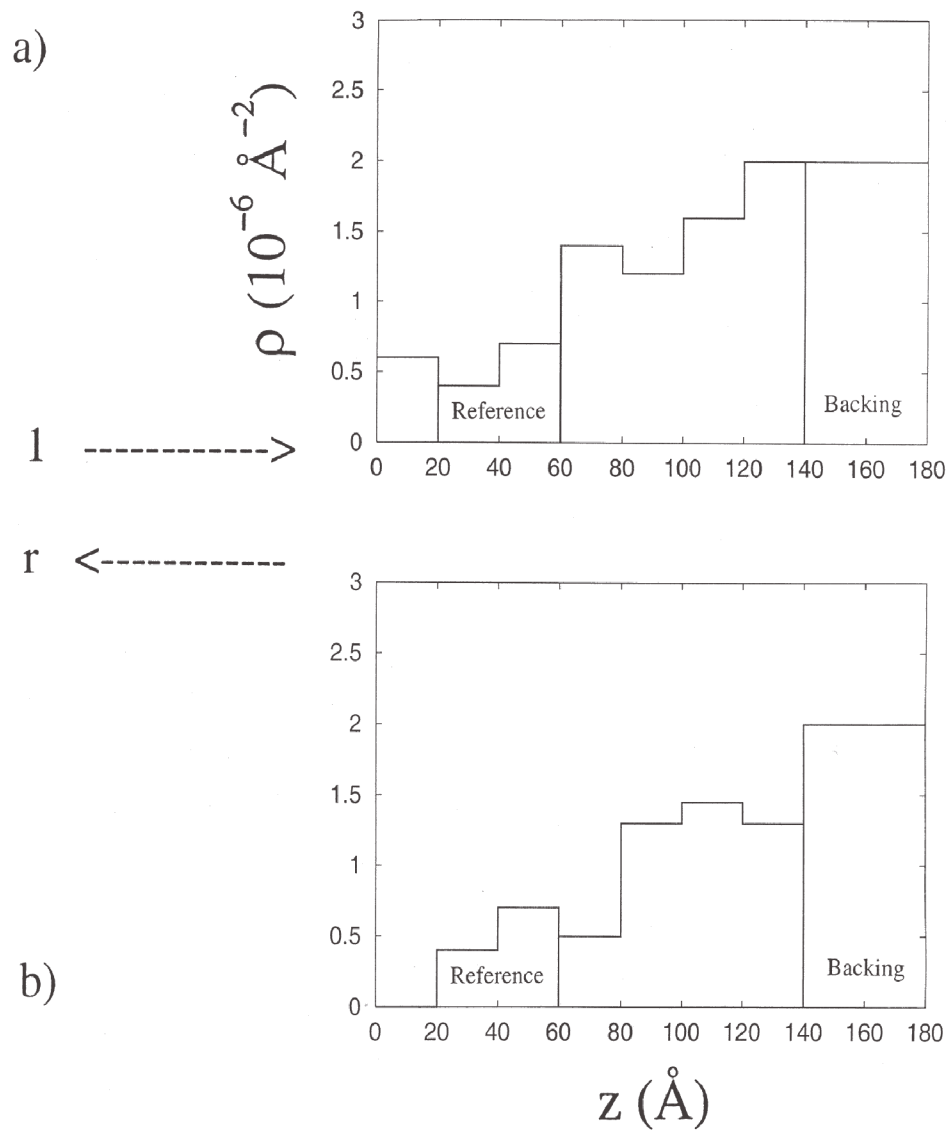
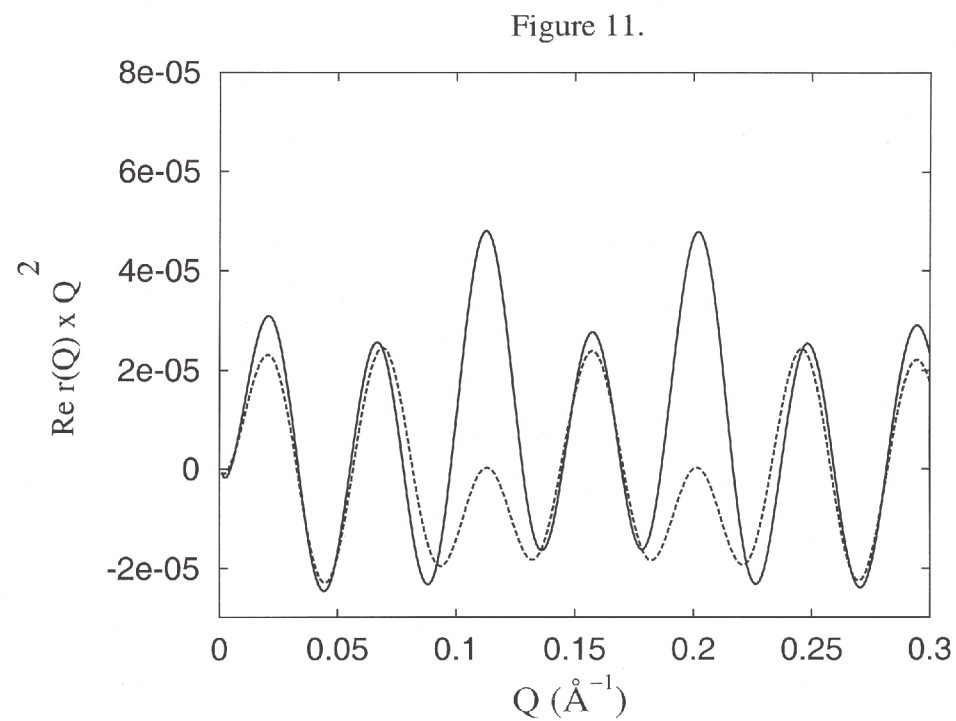
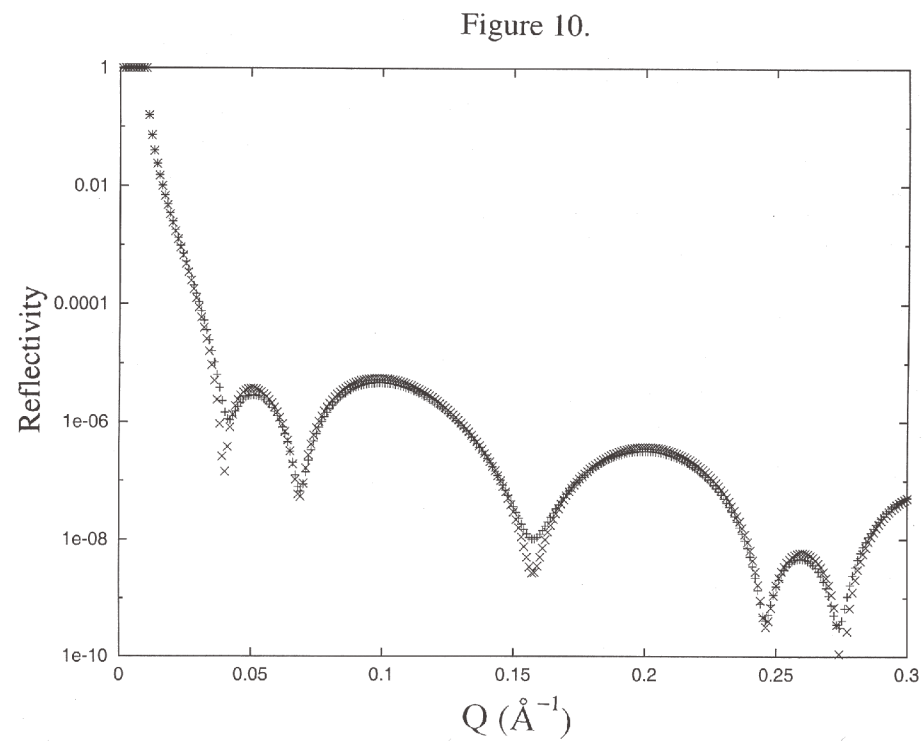
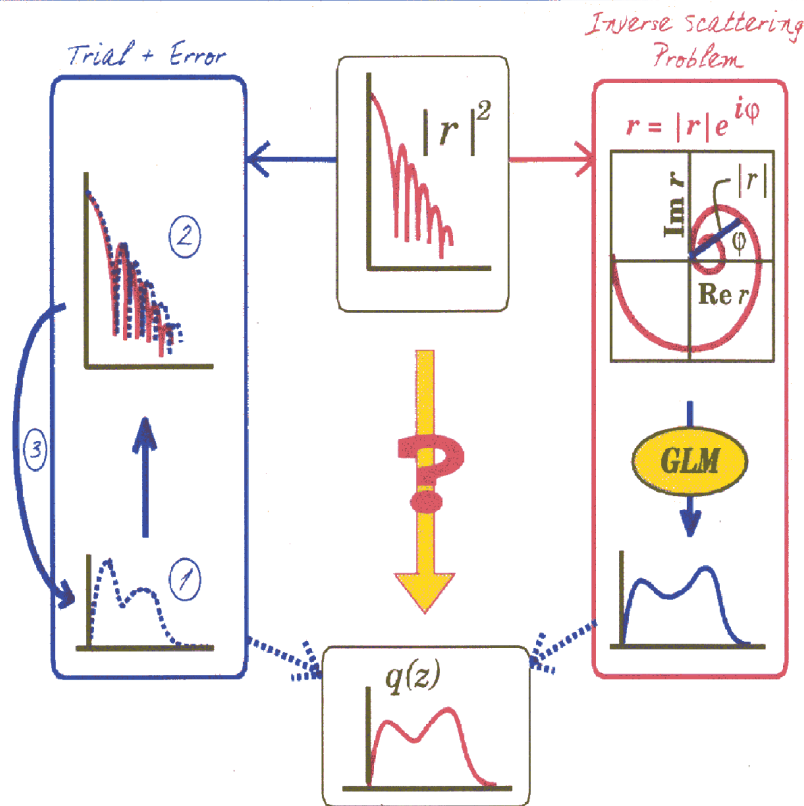


Figure 9.



# Inverting reflectivity



(after N.F. Berk)

Theoretically, Norm and several others, including Paul Sacks, Lipperheide, and Leeb, realized, that the one-dimensional specular reflectivity could be directly inverted **if** the reflected wave *amplitude* and not just the intensity as measured was known.

FOURIER TRANSFORM  
OF THE COMPLEX  
REFLECTION  
AMPLITUDE

$$R(z) = \frac{1}{\pi} \text{Re} \int_0^{\infty} r(k_z) e^{ik_z z} dk_z$$

GELFAND  
LEVITAN  
MARCHENKO  
INTEGRAL  
EQUATION

$$K(z, \gamma) + R(z + \gamma) + \int_{-z}^{+z} K(z, x) R(x + \gamma) dx = 0$$

SCATTERING  
LENGTH  
DENSITY

$$\rho(z) = 2 \frac{dK(z, z)}{dz}$$

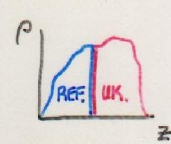
GIVEN THE COMPLEX REFLECTION AMPLITUDE, THE SCATTERING LENGTH DENSITY  $\rho$  CAN BE OBTAINED FROM AN EXACT, FIRST PRINCIPLE INVERSION FOR A REAL POTENTIAL OF FINITE EXTENT — AND THE SOLUTION IS UNIQUE!

NO FITTING, NO ADJUSTABLE PARAMETERS



But how do you determine the reflection amplitude as a function of  $Q$  from measured reflected intensity? Thinking about the piece-wise continuous solution method of the Shroedinger wave equation provided the answer . . .

FORMALISM ALLOWS A COMPOSITE POTENTIAL TO BE EXPRESSED AS A PRODUCT:

$$\underbrace{\begin{pmatrix} A & B \\ C & D \end{pmatrix}}_{\text{COMPOSITE (1,2,3)}} = \underbrace{\begin{pmatrix} a & b \\ c & d \end{pmatrix}}_{\text{UNKNOWN}} \underbrace{\begin{pmatrix} w & x \\ y & z \end{pmatrix}}_{\text{REFERENCE (1,2,3)}}$$


$$|R(Q)|^2 = |R_1(Q)|^2, |R_2(Q)|^2, \text{ and } |R_3(Q)|^2$$

$$\Sigma_i \equiv 2 \left[ \frac{1 + |R_i|^2}{1 - |R_i|^2} \right] = A_i^2 + B_i^2 + C_i^2 + D_i^2$$

$$A_i^2 = a^2 w_i^2 + b^2 y_i^2 + 2abw_i y_i$$

$$C_i^2 = c^2 w_i^2 + d^2 y_i^2 + 2cdw_i y_i$$

$$B_i^2 = a^2 x_i^2 + b^2 z_i^2 + 2abx_i z_i$$

$$D_i^2 = c^2 x_i^2 + d^2 z_i^2 + 2cdx_i z_i$$

(INDEPENDENTLY AT EACH  $Q$ )

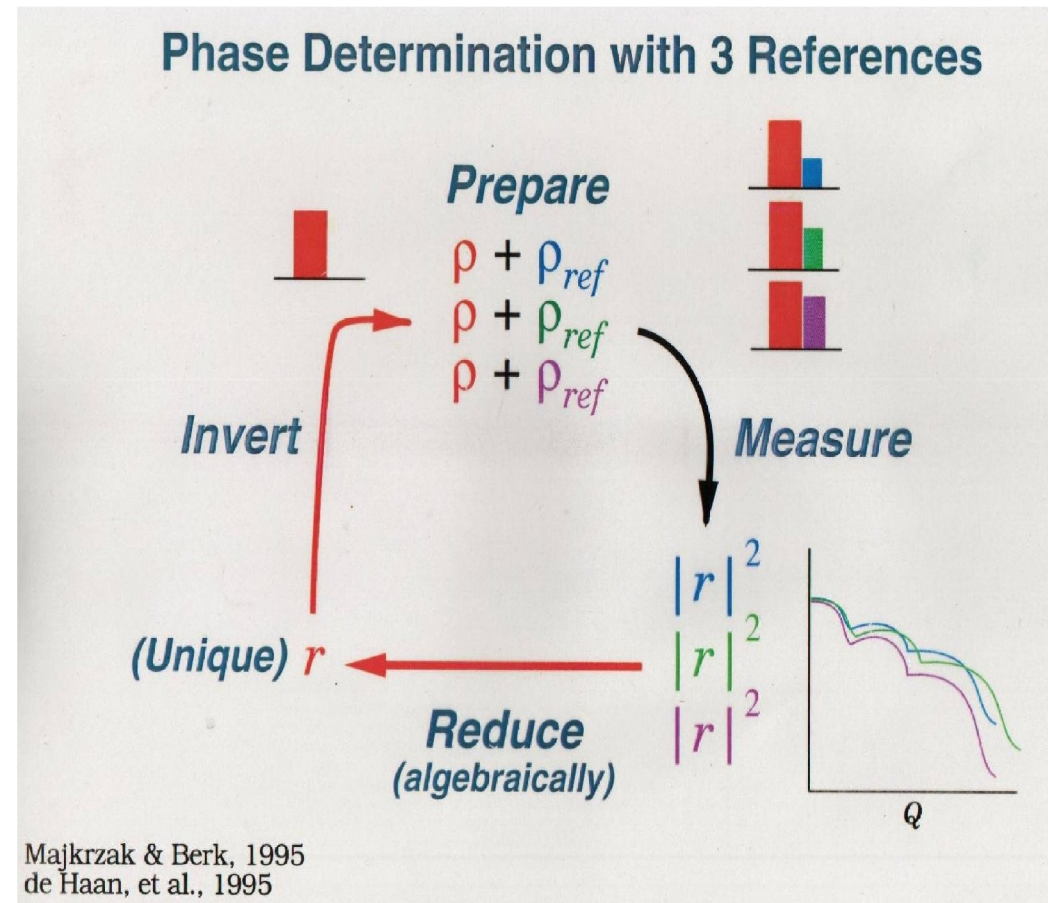
$$\Sigma_i = \underbrace{(w_i^2 + x_i^2)}_{\text{REF}} \alpha + \underbrace{(y_i^2 + z_i^2)}_{\text{REF}} \beta + 2(w_i y_i + x_i z_i) \gamma$$

$i = 1, 2, 3$

SOLVE FOR UNKNOWN  $\alpha, \beta$ , AND  $\gamma$  TO GET

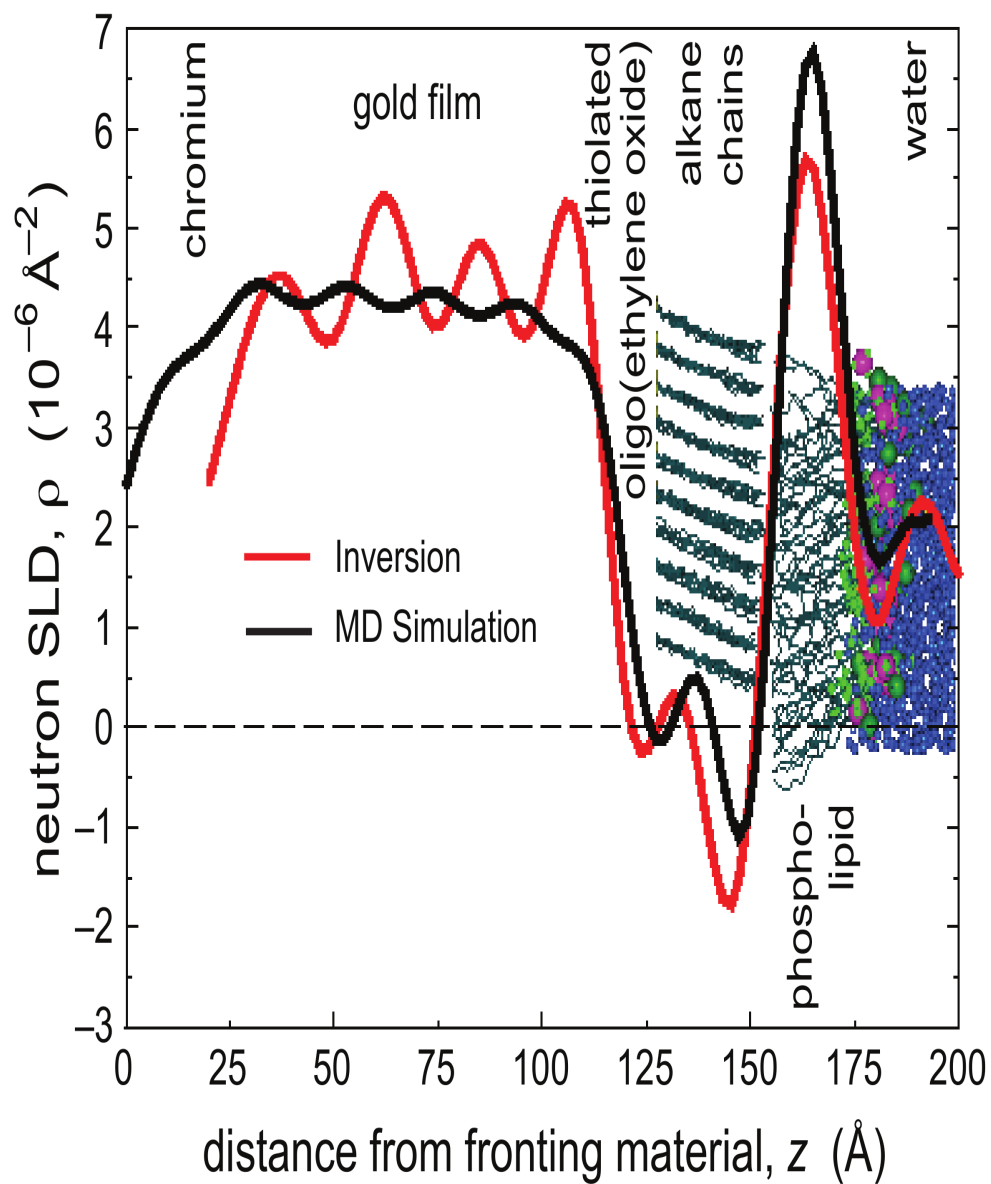
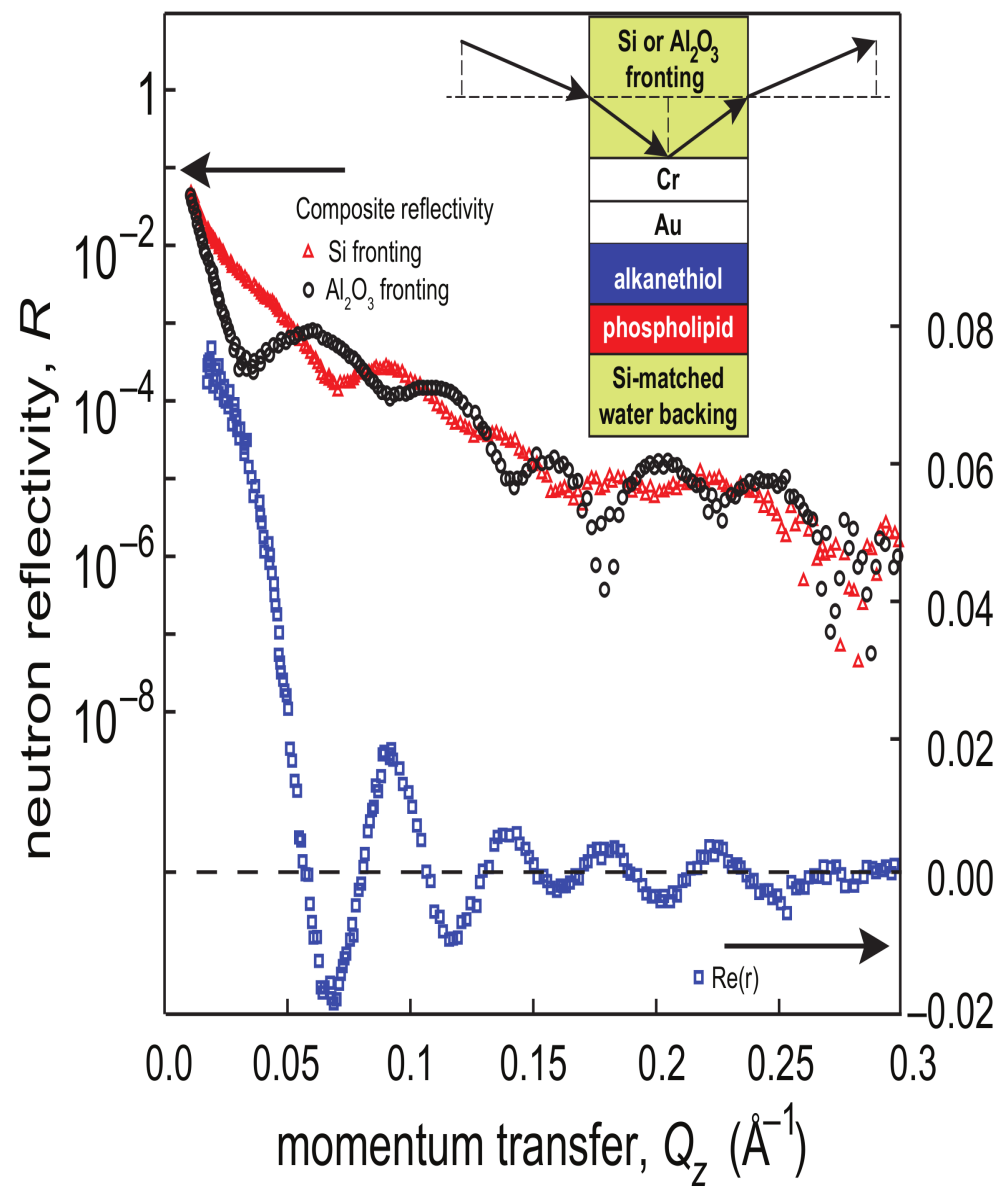
$$R_{\text{UNKNOWN}} = \frac{(\beta - \alpha) - 2i\gamma}{2 + \beta + \alpha}$$

$\alpha = a^2 + c^2$   
 $\beta = b^2 + d^2$   
 $\gamma = ab + cd$



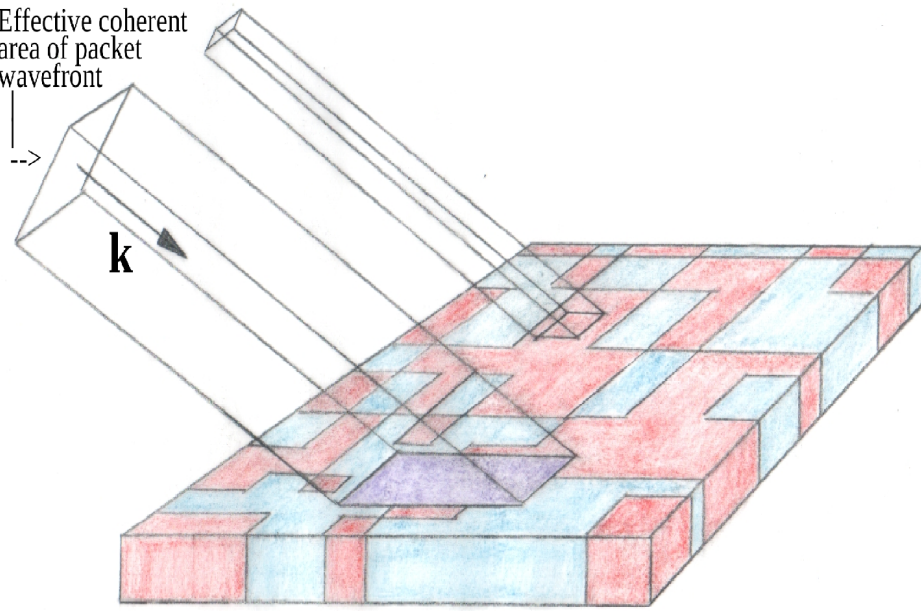
### Phase determination

C.F. Majkrzak and N.F. Berk, Phys. Rev. B **52**, 10827 (1995).  
 V.-O. de Haan, et al., Phys. Rev. B **52**, 10830 (1995).





Effective coherent  
area of packet  
wavefront



PHYSICAL REVIEW A **89**, 033851 (2014)

## Determination of the effective transverse coherence of the neutron wave packet as employed in reflectivity investigations of condensed-matter structures. I. Measurements

Charles F. Majkrzak,<sup>\*</sup> Christopher Metting, Brian B. Maranville, Joseph A. Dura, Sushil Satija, Terrence Udovic, and Norman F. Berk

*Center for Neutron Research, National Institute of Standards and Technology Gaithersburg, Maryland 20899, USA*

(Received 6 September 2013; revised manuscript received 22 November 2013; published 27 March 2014)

The primary purpose of this investigation is to determine the effective coherent extent of the neutron wave packet transverse to its mean propagation vector  $\mathbf{k}$  when it is prepared in a typical instrument used to study the structure of materials in thin film form via specular reflection. There are two principal reasons for doing so. One has to do with the fundamental physical interest in the characteristics of a free neutron as a quantum object, while the other is of a more practical nature, relating to the understanding of how to interpret elastic scattering data when the neutron is employed as a probe of condensed-matter structure on an atomic or nanometer scale. Knowing such a basic physical characteristic as the neutron's effective transverse coherence can dictate how to properly analyze specular reflectivity data obtained for material film structures possessing some amount of in-plane inhomogeneity. In this study we describe a means of measuring the effective transverse coherence length of the neutron wave packet by specular reflection from a series of diffraction gratings of different spacings. Complementary nonspecular measurements of the widths of grating reflections were also performed, which corroborate the specular results. (This paper principally describes measurements interpreted according to the theoretical picture presented in a companion paper.) Each grating was fabricated by lift-off photolithography patterning of a nickel film (approximately 1000 Å thick) formed by physical vapor deposition on a flat silicon crystal surface. The grating periods ranged from 10 μm (5 μm Ni stripe, 5 μm intervening space) to several hundred microns. The transverse coherence length, modeled as the width of the wave packet, was determined from an analysis of the specular reflectivity curves of the set of gratings.

DOI: [10.1103/PhysRevA.89.033851](https://doi.org/10.1103/PhysRevA.89.033851)

PACS number(s): 42.25.Kb, 37.20.+j, 03.75.Dg, 61.05.fj

The effective transverse coherence area perpendicular to the propagation direction of the neutron wave packet is projected onto the film surface defining an area over which in-plane variations in SLD are averaged over in the specular process (note that the glancing angle of incidence enhances the projection along one in-plane direction):

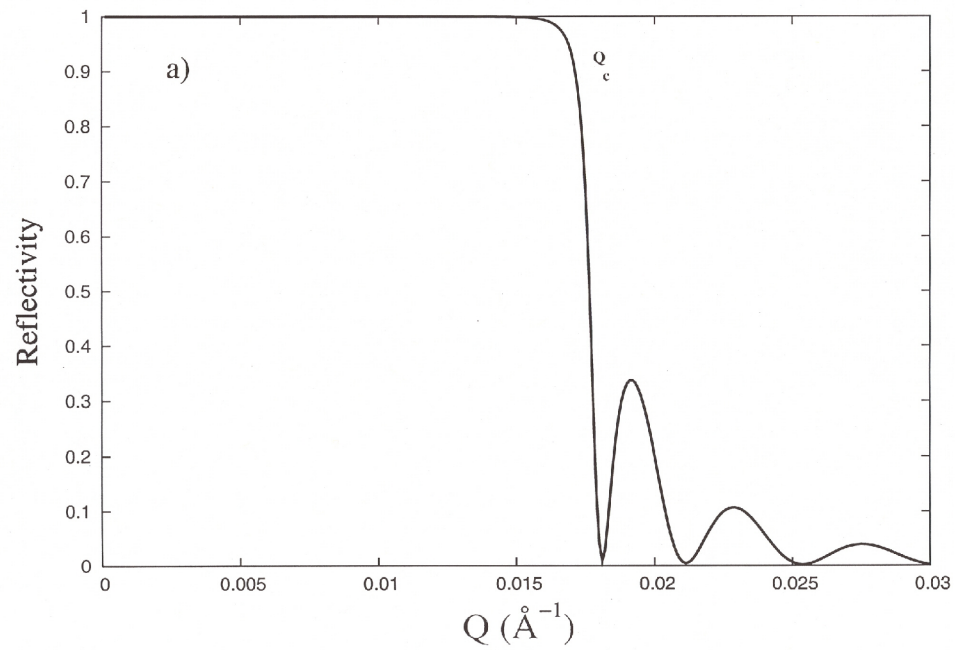
$$r = (4\pi / (iQ)) \int_{-\infty}^{+\infty} \psi_{kz}(z) \langle \rho(x,y,z) \rangle_{x,y} e^{ikz} dz$$

$$\langle \rho(x,y,z) \rangle_{x,y} = (1/A) \int_{-\infty}^{+\infty} \rho(x,y,z) dx dy$$

The length scale of the SLD variations must be small enough for effective averaging to occur within the projected area. (The purple shaded area is meant to represent the coherent average of separate areas of “red” and “blue” SLD.) If not, then the net measured reflected intensity  $|r|^2$  is an area-weighted sum of reflectivities, each corresponding to an in-plane averaged SLD within a particular respective area, as depicted schematically in the figure above for the case of two distinct areas of different SLD (red and blue areas):

$$|r_{\text{NET MEASURED}}|^2 = (A_{\text{RED}} / A_{\text{TOTAL}}) |r_{\text{RED}}|^2 + (A_{\text{BLUE}} / A_{\text{TOTAL}}) |r_{\text{BLUE}}|^2$$

Figure 13



## Coherent Average

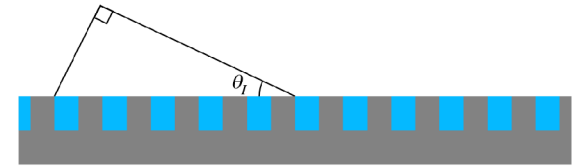
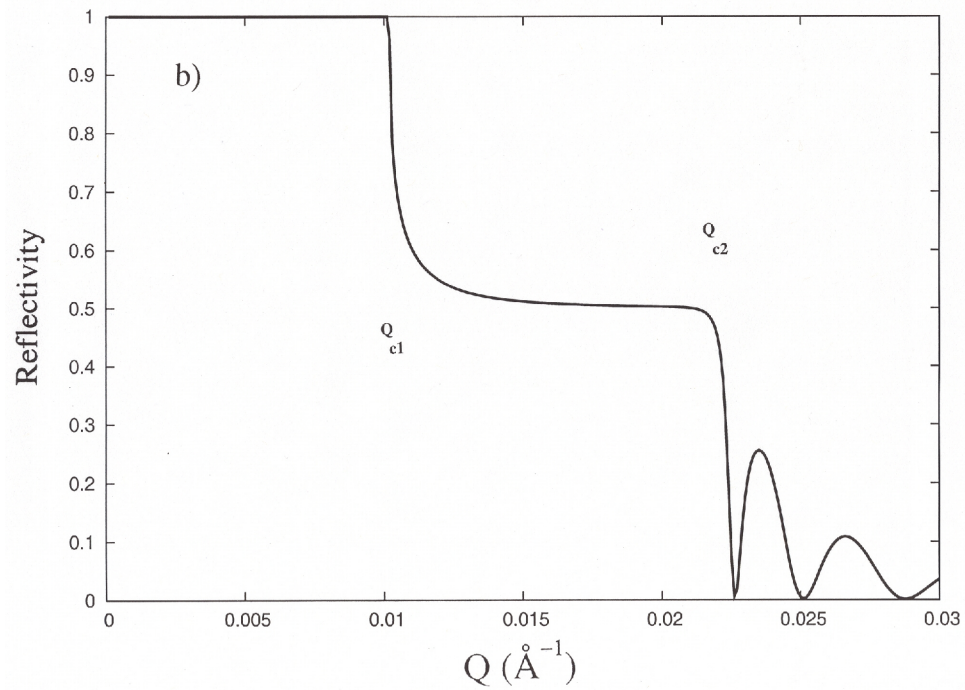
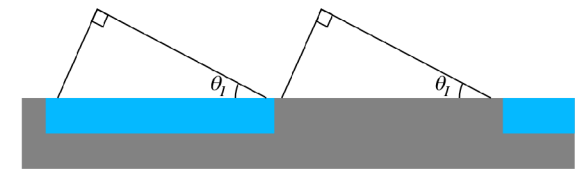


Figure 13

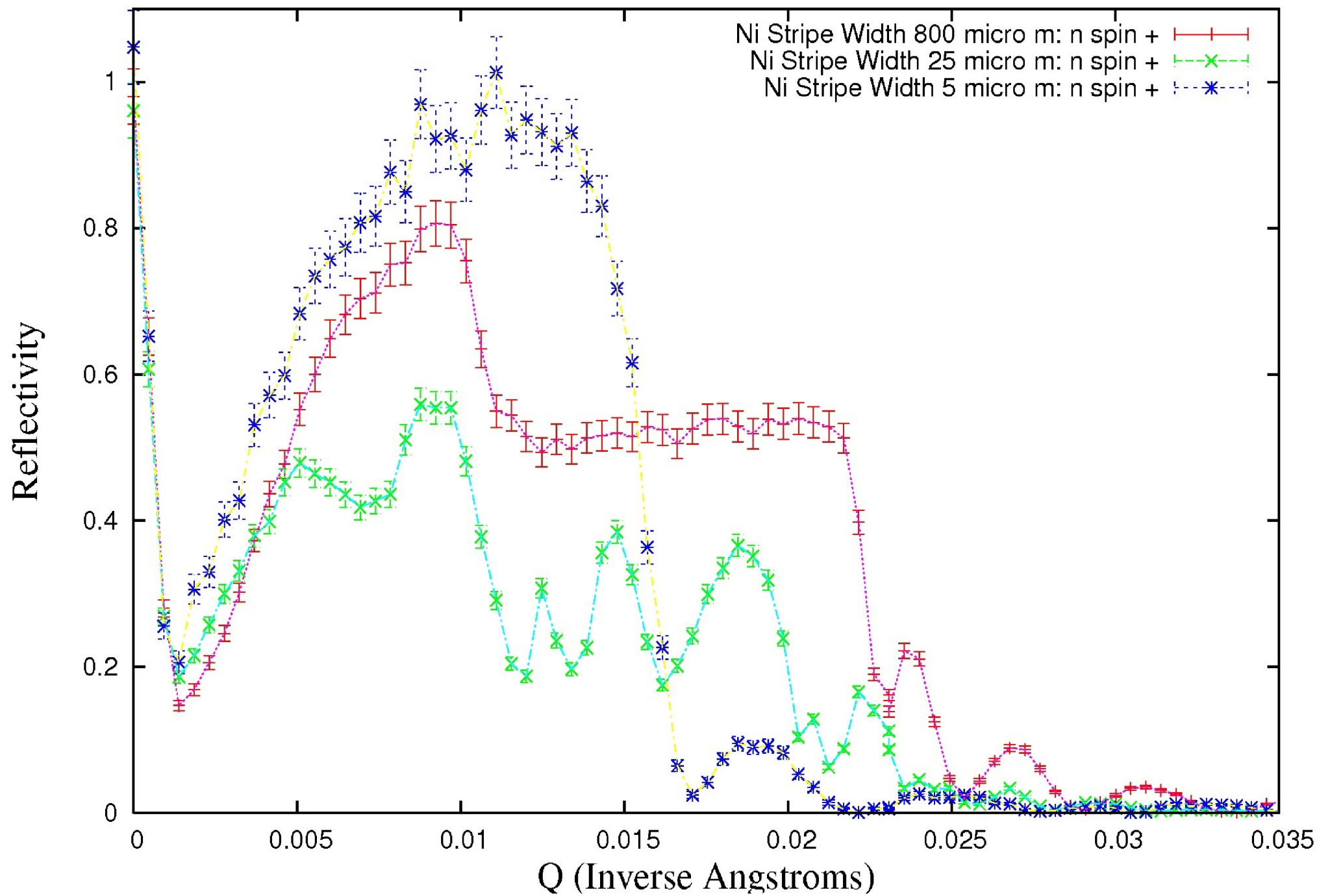


## Incoherent Sum





Grating Stripes Perpendicular to Scattering Plane



Coming to the NCNR?  
Click Here.  
Visa question?  
Logon to your  
NCNR-IMS account

#### NCNR SiteMap

#### About the NCNR

What We Do  
Informal History  
Staff  
Annual Report  
2017 Summer School  
June 19-June 23, 2017  
Working at the NCNR  
See differently with neutrons  
at NIST (video)

#### Facility Information

Live Data  
Instrumentation  
Instrument Contacts  
Schedules  
Center for High Resolution  
Neutron Scattering (CHRS)  
>Education and Outreach  
Sample Environment  
NCNR Staff Forms  
Sample Prep Labs

#### User Information

Planning Your Experiment  
Obtaining BeamTime  
Data Reduction/Analysis  
Shipping Samples  
Publishing Your Results  
Financial Assistance  
Travel & Lodging  
NCNR User Group

#### Other Sites

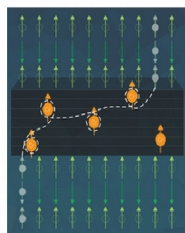
Neutron Sources  
Photon Sources  
Postdoctoral Opportunities  
Societies & Organizations



Maximizing access for the scientific  
community to transformative  
neutron scattering instrumentation

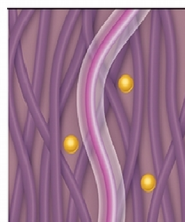
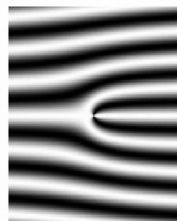
A consortium for the advancement  
of neutron-based measurements for  
manufacturing of soft materials

### RECENT RESEARCH HIGHLIGHTS



NIST collaboration heats up exotic  
topological insulators  
details  
paper in Nature Materials  
press release (UCLA)  
news item in IEEE Spectrum

Move over, lasers: scientists can now  
create holograms from neutrons, too  
details  
paper in Optics Express  
news item in Physics Today



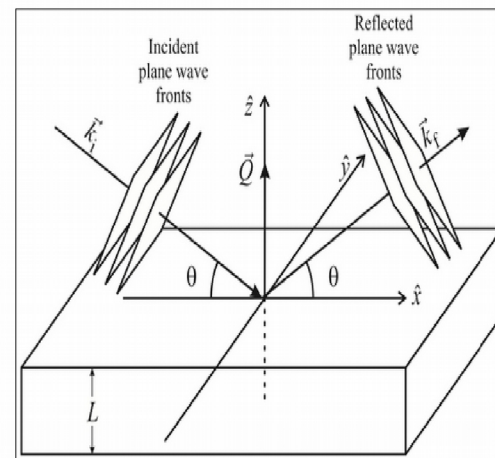
Nanoparticles can make polymers  
flow more easily  
details  
paper in Physical Review Letters

## NIST CENTER FOR NEUTRON RESEARCH

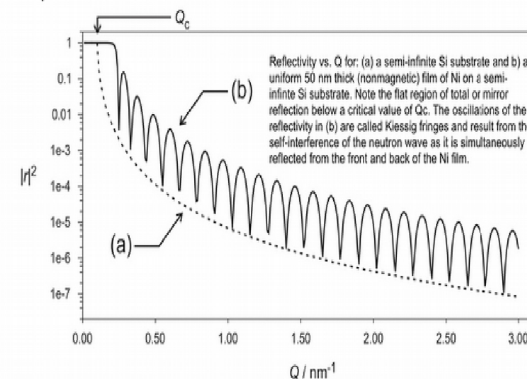
NCNR-IMS Login Facility Information User Information CHRS News About NCNR

### Surfaces and Interfaces Team

### Neutron Reflectometry



Reflectometry uses neutrons scattered at grazing angles to probe the nuclear and magnetic composition of flat samples. Common types of materials studied include biological membranes, magnetic multilayers, and polymer films. The NCNR currently operates three reflectometers - PBR, MAGIK, and NG-7 - each specially configured for different types of research. Additionally, construction is underway on CANDOR, a revolutionary new white beam reflectometer. Please visit the instrument pages (linked at right) for specific information.



#### Reflectometers

- PBR - Magnetism
- MAGIK - Offspecular Capability
- NG7 - Horizontal Geometry
- CANDOR - White Beam

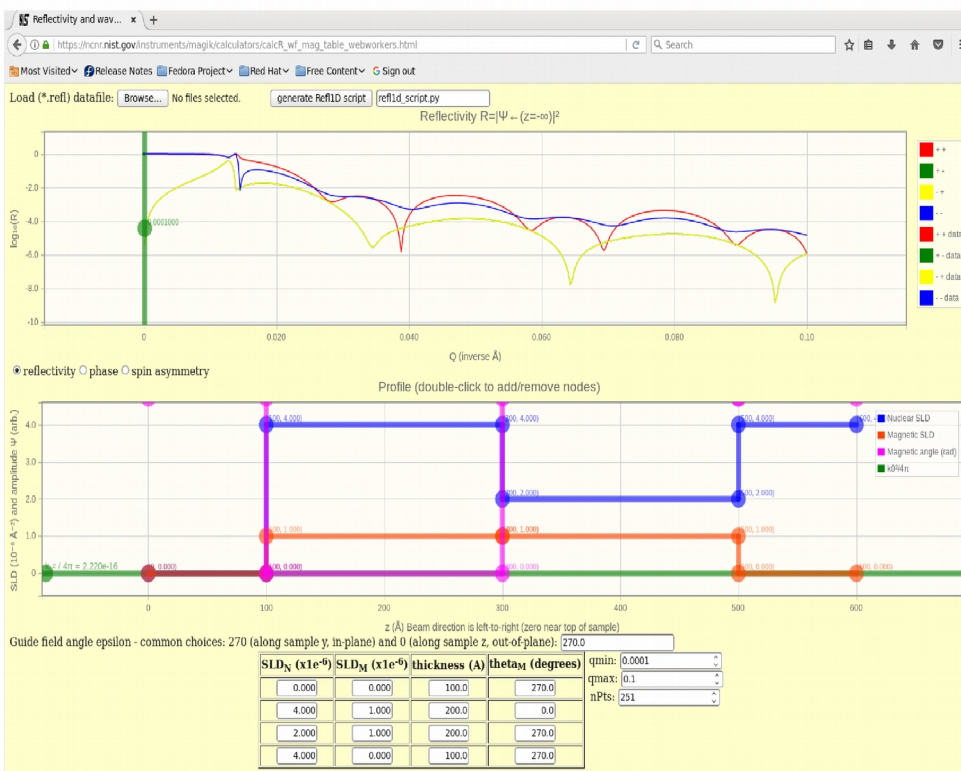
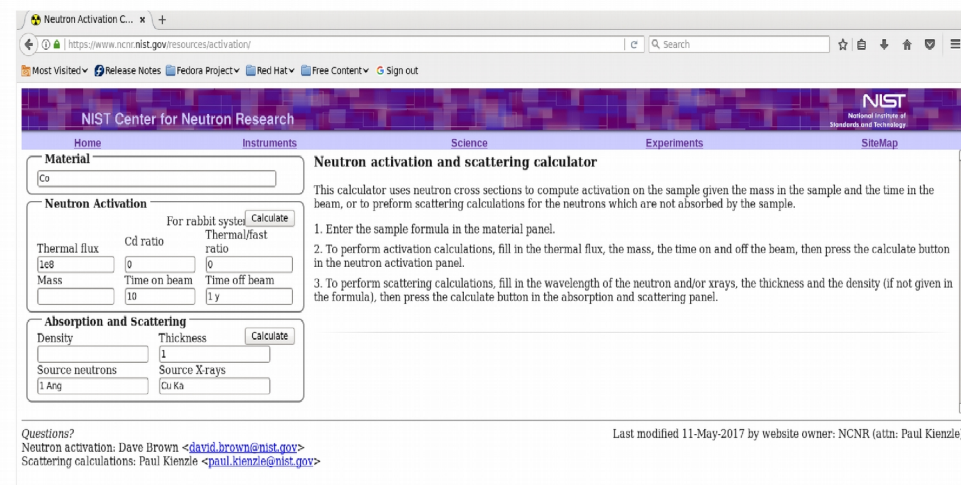
#### Data Analysis

- Online data reduction
- Raw data file explorer
- SLD Calculator
- Scatterer's Periodic Table
- Ref1D Model Fitting (Windows)
- Ref1D Model Fitting (Mac)

#### Reference Material

- Theory of PNR
- NR Summer School Lecture
- PNR Summer School Lecture
- PNR and Magnetic Materials
- Pynn Neutron Primer





On-line programs for calculating scattering length densities and specular neutron reflectivity – fitting programs are also available. (Developed and maintained by NCNR staff, particularly Brian Maranville and Paul Kienzie.)

# Interactive, Web-Based Calculator of Neutron and X-ray Reflectivity

Brian B. Maranville

National Institute of Standards and Technology,  
Gaithersburg, MD 20899, USA

[brian.maranville@nist.gov](mailto:brian.maranville@nist.gov)

Software DOI: <https://doi.org/10.18434/M3QG67>

Software Version: 1.0

Key words: calculator; neutron; reflectivity; scattering.

Accepted: June 30, 2017

Published: July 12, 2017

<https://doi.org/10.6028/jres.122.034>

## 1. Summary

For many users of the neutron and X-ray reflectometry instruments at NIST, these measurements represent a relatively small and specialized part of their research portfolio. As such, providing calculation and modeling tools that are as accessible and easy-to-use as possible is a high priority of the facility. In order to meet this need, a purely web-browser-based calculator for reflectivity modeling and rudimentary fitting has been developed and provided on a publicly accessible web server.

Going to <https://www.ncnr.nist.gov/instruments/magik/calculators/reflectivity-calculator.html>, will load a one-page web application into the browser. Any relatively modern browser with support for ECMAScript 5 will be able to load and run the application. A calculator for magnetic samples can be found at <https://www.ncnr.nist.gov/instruments/magik/calculators/magnetic-reflectivity-calculator.html>.



Fig. 1. Screenshot of non-magnetic reflectivity calculator.

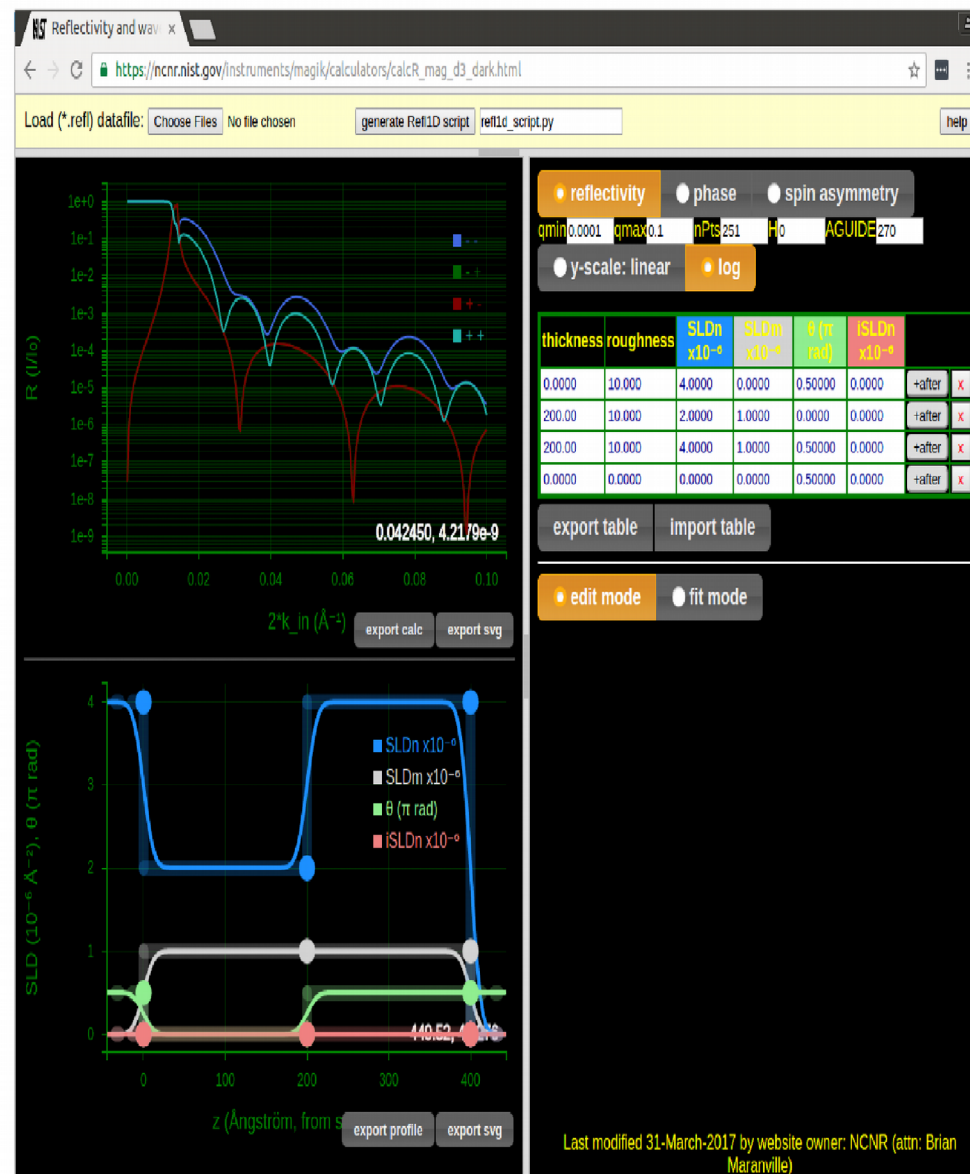


Fig. 2. Screenshot of magnetic reflectivity calculator.



## Bibliography / References

Optics, 3rd Ed., by E. Hecht, Addison-Wesley, 1998.

Neutron Optics, by V.F. Sears, Oxford University Press, 1989.

Principles of Optics, 6th Ed., by M. Born and E. Wolf, Pergamon Press, 1987.

Quantum Mechanics, 2nd Ed., by E. Merzbacher, Wiley, 1970.

“Structural Investigations of Membranes in Biology by Neutron Reflectometry”, C.F.Majkrzak, N.F.Berk, S.Krueger, and U.A.Perez-Salas, Chapter 12 in *Neutron Scattering in Biology*, Edited by J.Fitter, T.Gutberlet, and J.Katsaras, (Springer, Berlin, 2006) p.225-263.

“Polarized Neutron Reflectometry”, C.F.Majkrzak, K.V.O'Donovan, and N.F.Berk, Chapter 9 in *Neutron Scattering from Magnetic Materials*, Edited by T.Chatterji, (Elsevier, Amsterdam, 2006) p.397-471.

“Phase-Sensitive Neutron Reflectometry”, C.F.Majkrzak, N.F.Berk, and U.A.Perez-Salas, *Langmuir* **19**, 7796 – 7810 (2003).

B.J.Kirby et al., Phase-sensitive specular neutron reflectometry . . . , *Current Opinion in Colloid & Interface Science* **17** (2012) 44-53.

C.F.Majkrzak et al., *J. Appl. Phys.* **110** (2011).

www.ncnr.nist.gov -- look here for information about neutron reflectometry in general as well as in specific studies highlighted in past and current annual reports for the facility.